

N8470505

AERODYNAMIC CHARACTERISTICS OF A JET VTOL WING-BODY
CONFIGURATION IN TRANSITION FLIGHT

by

Raymond Edward Mineck

B.S. in Aeronautical Engineering

Rensselaer Polytechnic Institute

1970

A Thesis submitted to

the Faculty of

The School of Engineering and Applied Sciences

of the George Washington University in partial satisfaction

of the requirements for the degree of Master of Science

May 1975

Thesis directed by

Dr. Alvin M. Bloom

Assistant Research Professor of Engineering

AERODYNAMIC CHARACTERISTICS OF A JET VTOL WING-BODY
CONFIGURATION IN TRANSITION FLIGHT

by

Raymond Edward Mineck

B.S. in Aeronautical Engineering
Rensselaer Polytechnic Institute

1970

A Thesis submitted to

the Faculty of

The School of Engineering and Applied Sciences
of the George Washington University in partial satisfaction
of the requirements for the degree of Master of Science

May 1975

Thesis directed by

Dr. Alvin M. Bloom

Assistant Research Professor of Engineering

ABSTRACT

Jet VTOL aircraft can experience some severe interference effects when transitioning from hover to wingborne flight. A wind-tunnel investigation was conducted to obtain force measurements and extensive pressure measurements on a vectored-thrust wing-body combination to understand the causes of the interference problems and to provide basic data for comparisons with existing analytical methods. The jet's interference effects are strongest at the lowest effective velocity ratios and at locations nearest the jet. The effects are strongly dependent on effective velocity ratio and weakly dependent on angle of attack. The vectored-thrust jets with the exits near the wing trailing edge showed the most beneficial (least detrimental) interference effects of the configurations tested. The analytical method generally predicted the correct trends although the levels were not always correct.

ACKNOWLEDGEMENTS

The author wishes to extend his gratitude to the Langley Research Center for supporting this thesis. Appreciation is also expressed to Dr. Alvin M. Bloom of George Washington University for his valuable guidance and helpful criticism.

TABLE OF CONTENTS

	Page
ABSTRACT.	ii
ACKNOWLEDGEMENTS.	iii
TABLE OF CONTENTS	iv
LIST OF TABLES.	vi
LIST OF FIGURES	vii
LIST OF SYMBOLS	x

Chapter

I. INTRODUCTION.	1
II. BACKGROUND.	3
III. BRIEF DESCRIPTION OF WOOLER'S METHOD.	6
Jet-Flow-Field Program.	7
Lifting-Surface Program	8
IV. DESCRIPTION OF THE WIND-TUNNEL MODEL.	9
V. TESTS AND PROCEDURES.	11
VI. DISCUSSION OF EXPERIMENTAL RESULTS.	14
Lift-Jet Configuration	15
Front Vectored-Thrust Configuration	19
Rear Vectored-Thrust Configuration.	22
Rear Vectored-Thrust Configuration with Flaps	23
Interference on the Fuselage.	24
Comparison of Theory and Experiment	25

	Page
VII. CONCLUSIONS	29
APPENDIX.	31
REFERENCES.	42
TABLE	45
FIGURES	46

LIST OF TABLES

TABLE - Load Range and Accuracy of the Balance

LIST OF FIGURES

Figure

1. Sketch of the model.
2. Photographs of the model.
3. High-pressure air system.
4. Variation of C_T with V_e .
5. System of axes.
6. Basic aerodynamic characteristics of the lift-jet configuration.
7. Wing-pressure distribution for the lift-jet configuration.
8. Variation of C_L/C_T and C_m/C_T with V_e for the lift-jet configuration.
9. Variation of the thrust-removed characteristics with angle for attack of the lift-jet configuration.
10. Variation of the interference effects with angle of attack for the lift-jet configuration.
11. Variation of the interference effects with effective velocity ratio for the lift-jet configuration.
12. Basic aerodynamic characteristics of the front vectored-thrust configuration.
13. Wing-pressure distribution for the front vectored-thrust configuration.
14. Variation of C_L/C_T and C_m/C_T with V_e for the front vectored-thrust configuration.

Figure

15. Variation of the thrust-removed characteristics with angle of attack for the front vectored-thrust configuration.
16. Variation of the interference effects with angle of attack for the front vectored-thrust configuration.
17. Variation of the interference effects with effective velocity ratio for the front vectored-thrust configuration.
18. Basic aerodynamic characteristics of the rear vectored-thrust configuration.
19. Wing-pressure distribution for the rear vectored-thrust configuration.
20. Variation of C_L/C_T and C_m/C_T with V_e for the rear vectored-thrust configuration.
21. Variation of the thrust-removed characteristics with angle of attack for the rear vectored-thrust configuration.
22. Variation of the interference effects with angle of attack for the rear vectored-thrust configuration.
23. Variation of the interference effects with effective velocity ratio for the rear vectored-thrust configuration.
24. Basic aerodynamic characteristics of the rear vectored-thrust configuration with flaps.
25. Variation of the jet-induced interference with effective velocity ratio for the rear vectored-thrust jets with flaps.
26. Basic aerodynamic characteristics of the fuselage alone with the lift jet.
27. Variation of the jet-induced interference effects with effective velocity ratio for the fuselage alone with the lift jet.

Figure

28. Basic aerodynamic characteristics of the fuselage alone with the front vectored-thrust jet.
29. Variation of the jet-induced interference effects with effective velocity ratio for the fuselage alone with the front vectored-thrust jet.
30. Variation of the interference effects on the wing with effective velocity ratio for the lift jet.
31. Variation of the interference on the wing with effective velocity ratio for the front vectored-thrust jets.
32. Variation of the interference on the wing with effective velocity ratio for the rear vectored-thrust jets.
33. Variation of the interference on the wing with flaps with effective velocity ratio for the rear vectored-thrust jets.

LIST OF SYMBOLS

A_j	effective jet-exit area, m^2 (ft^2)
b	wing span, 1.02 m^2 (3.35 ft^2)
c	local wing chord, cm (in.)
\bar{c}	wing mean aerodynamic chord, 21.21 cm (8.35 in.)
C	circumference of jet, cm (in.)
C_d	section-drag coefficient
C_L	lift coefficient, $L/q_\infty S$
C_{L_T}	thrust-removed lift coefficient, $L_T/q_\infty S$
C_m	pitching-moment coefficient, $M_Y/q_\infty S \bar{c}$
C_{m_T}	thrust-removed pitching-moment coefficient, $M_{Y_T}/q_\infty S \bar{c}$
C_p	pressure coefficient, $(p_\ell - p_\infty)/q_\infty$
C_T	thrust coefficient, $T/q_\infty S$
d	jet diameter, cm (in.)
d_o	jet-exit diameter, cm (in.)
D	ratio of major to minor axis of an ellipse or drag

E	entrainment per unit length of jet
E_1, E_2, E_3	entrainment empirical constants
F_B	body force on jet boundary
k	kernel function
L	lift, N (lbf)
L_T	thrust-removed lift, N (lbf)
m	sink strength
M_Y	pitching moment, N-m (lbf-in.)
M_{YT}	thrust-removed pitching moment, N-m (lbf-in.)
p_ℓ	local pressure, N/m ² (lbf/ft ²)
p_∞	free-stream static pressure, N/m ² (lbf/ft ²)
P_R	pressure loading function
q_∞	free-stream dynamic pressure, N/m ² (lbf/ft ²)
q_j	jet-exit dynamic pressure, N/m ² (lbf/ft ²)
r	radial distance from singularity
R	radius of curvature
s	distance along the jet path

S	wing reference area, $0.209 \text{ m}^2 (2.25 \text{ ft}^2)$
T	total thrust, N (lbf)
u_d	disturbance velocity from the doublet in the x direction.
u_s	disturbance velocity from the sink in the x direction
v_d	disturbance velocity from the doublet in the y direction
v_s	disturbance velocity from the sink in the y direction
V_e	effective velocity ratio
V_j	jet velocity
V_{j0}	jet velocity at the exit
V_∞	free-stream velocity
w_d	disturbance velocity from the doublet in the z direction
w_s	disturbance velocity from the sink in the z direction
y	distance from fuselage centerline, positive out the right wing
z	distance from jet exit
α	angle of attack
β	$1 - (\text{Mach No.})^2$

ΔC_m	interference increment in pitching moment
ΔC_L	interference increment in lift
δ_j	jet-nozzle deflection angle, deg
μ	doublet strength
ρ_∞	free-stream density, kg/m^3 (lbm/ft^3)
ρ_j	jet density, kg/m^3 (lbm/ft^3)
η	fraction of semispan, $y/(b/2)$
ϕ	velocity potential
θ	angle of jet from vertical, deg
ξ, η, ζ	coordinate system centered at doublet

CHAPTER I

INTRODUCTION

The analysis of the aerodynamic characteristics of jet-powered vertical takeoff and landing (VTOL) aircraft is a more complex problem than that of conventional takeoff and landing aircraft. Two of the reasons for the additional complexity are the need to account for the induced effects of the jet exhaust and the need for nonlinear aerodynamic theory in the transition-speed range. The transition-speed range covers the forward speeds between hover and the minimum required for wingborne flight. During transition, the jet-exhaust flow is directed at large angles relative to the free stream. The jet exhaust interferes with the flow field around the aircraft inducing a change in the forces on the aircraft. The aircraft may also fly at large angles relative to the free stream so that linear aerodynamic theory can no longer be applied.

A great deal of force data has been obtained on jet VTOL configurations. The effect of the jet-exhaust location on a simple wing-body configuration was investigated in Reference [1]. The results showed that the jet induces a lift loss at some jet locations. The most favorable induced effects were obtained when the jet exhaust was below and behind the wing.

Complete configurations have also been tested by other investigators. These include the Kestrel which is a predecessor of the Harrier, the world's only production jet VTOL aircraft. The Kestrel uses vectored

thrust to obtain its VTOL capability. The results of wind-tunnel tests of the Kestrel, presented in Reference [2], showed the lift loss and a pitch-up problem in transition which poses a trim problem for the pilot. Another complete configuration that has been tested uses a "lift-plus-lift-cruise" engine arrangement to obtain a VTOL capability. This concept uses a lift jet in hover and uses the vectored-thrust engines for lift in hover and transition and for overcoming the drag in cruise. This investigation, presented in Reference [3], also shows the lift loss and the pitch-up problem. None of these investigations dealt deeply with the forces on each component of the aircraft such as the fuselage, nacelles, and wing. Also, only a limited amount of pressure data were obtained on the wing of the simple wing body of Reference [1]. No pressure data were obtained in the investigations of References [2] and [3].

In the present investigation, a wind-tunnel model was built and tested to obtain force measurements and extensive pressure measurements on the fuselage, nacelles, and wing. These data are needed to understand the causes of the interference problem as well as provide basic data for comparison with existing analytical methods.

CHAPTER II

BACKGROUND

The experimental characteristics of the jet must be determined before the interference effects can be understood and eventually analyzed. The problem has been simplified by several investigators to a jet exhausting from a flat plate into a crossflow. Several investigations of the jet in a crossflow have been conducted to determine the jet's path, momentum, and mass flow as well as the pressures induced on the flat plate by the jet. Some of these investigations are reported in References [4] and [5]. The more complex problem of multiple jets is reported in Reference [6]. The research showed four important characteristics of the jet. They are: (1) two counter-rotating vortices; (2) the separated wake behind the jet, (3) the entrainment of flow into the jet; and (4) the solid blockage of the jet.

Early attempts (see Ref. [7]) to analyze the characteristics of the jet used an empirical curve fit for the jet path. However, the induced effects could not be readily handled with this approach. The empirical approach has been replaced with a semi-empirical approach which uses potential flow to model the jet. A NASA symposium entitled "The Analysis of a Jet in a Subsonic Crossflow (Ref. [8])" presents an overview of both the experimental and theoretical work on the problem. Two approaches of modeling the jet and its interference effects are the sink-doublet approach and the vortex-lattice approach.

The sink-doublet approach for modeling the jet in the cross wind was developed by Wooler (Ref. [9]). Expressions for the jet entrainment were derived and a simplifying assumption of the jet shape was made. The equations for the jet momentum and continuity and force the force normal to the jet were solved for the location of the jet centerline. The jet was then replaced by doublets and sinks along the jet path representing the blockage and the entrainment. The induced velocities are calculated from the strengths and locations of the sinks and doublets. The method, which is limited to handling circular jets, has been expanded to treat various jet configurations. It is capable of handling jets with stratified velocity profiles. Three types of velocity stratification can be treated - vaned jet nozzle, lift fan, and high-bypass ratio turbofan. The wake effects or separation behind the jet cannot be analyzed with this potential-flow model; however, it is believed that a source distribution may help improve the results. This method, which is often referred to as Wooler's method, has been used as the basis of several other VTOL prediction methods such as the one presented in Reference [10].

Several vortex-lattice approaches have been developed. One approach (developed by Monical (Ref. [11])) can analyze fan-in-wing VTOL aircraft. In this method, the wing is represented by a network of horseshoe vortices. The fan exhaust is represented by horseshoe vortex network distributed around the circumference of the jet exhaust with the unbound legs extending downstream. The strengths of the vortices are determined by requiring no flow pass through the surface at specified control points, thereby neglecting entrainment. The forces and moments are obtained from

the strengths and locations of the vortices. Because Wooler's method was the most advanced procedure, it was chosen to help analyze the results from the present investigation.

CHAPTER III

BRIEF DESCRIPTION OF WOOLER'S METHOD

Wooler's method is designed to analyze the jet-induced interference effects on a wing or a body or the unpowered aerodynamic characteristics of wing or body in the nonlinear angle-of-attack range. The analysis of each of these four cases is implemented using FORTRAN computer programs. To analyze the jet-induced effects on a wing, the jet flow-field program is used to determine the downwash field induced on the wing by the jet exhaust. This downwash distribution is treated as a modified tangency condition which is then input to the lifting-surface program. The effects due to the induced flow field from the jet are then computed. To analyze the jet-induced effects on a body, cross-sections of the body are mapped into a circle using a mapping program. The jet flow-field program is again used to compute the induced flow on the circular cross-section obtained from the mapping program. The induced flow field is used in the transformation program which computes the induced aerodynamics and maps the results back into the original coordinate system. A nonlinear body aerodynamics program is used to analyze the unpowered aerodynamics of the body outside of the linear angle-of-attack range. Similarly, a nonlinear wing aerodynamics program is used to analyze the wing. Because only the induced effects on the wing will be analyzed, only the jet flow-field program and the lifting-surface program will be discussed. A brief description of these two programs follows; a more

detailed description can be found in the Appendix. The complete derivation of the lifting-surface program can be found in Reference [12] and the other programs in Reference [13].

Jet Flow-Field Program

The fundamental problem in developing an analysis method was to formulate a mathematical model of the jet exhausting into a crossflow. When the jet exhausts into the crossflow, the higher pressures on the upstream side of the jet and the flow into the jet deflect the jet. An expression for the entrainment of flow into the jet was developed using dimensional analysis by accounting for the flow perpendicular to the jet and flow parallel to the jet.

The force on the jet boundary was modeled by a crossflow-drag coefficient. The expression for entrainment is used in the continuity and momentum equations for the jet. The force on the jet is used in the equation for the jet's curvature. Experimental data were used to determine the empirical constants in the entrainment model. To simplify the representation of the jet, the jet shape was assumed to be an ellipse. These three equations for the jet's curvature, mass flow, and momentum were solved for the derivatives of the jet position, velocity, and diameter. Because the equations could not be solved in closed form, they were numerically integrated. To evaluate the flow field induced by the jet, the jet is replaced by a sink distribution to account for the entrainment and a doublet distribution to account for the blockage.

The velocity induced by the sinks and doublets were summed at specified control points.

This induced flow field, evaluated at control points on the wing, is used in the lifting-surface program to evaluate the effects of the modified flow field on the wing.

Lifting-Surface Program

The lifting-surface program is an implementation of the theory developed in Reference [14]. The lifting-surface program is based on the solution of the integral equation relating the downwash at a point on the wing to the product of a pressure loading function and a kernel function. The pressure loading function was assumed to be a finite series with the constant undetermined coefficients. The resulting matrix equation related a downwash matrix to the product of a downwash control point matrix and the unknown constant matrix of the pressure loading series. The equation is solved for the pressure series which is integrated for the lift, induced drag, and pitching-moment coefficients on the wing. The method can handle a wing with flaps, but it cannot handle a wing in sideslip or a fuselage.

CHAPTER IV

DESCRIPTION OF THE WIND-TUNNEL MODEL

The model used in this investigation was a vectored-thrust V/STOL configuration designed specifically to obtain extensive pressure data to identify the interference on the various aircraft components. The wing, fuselage, and vectored-thrust engine nacelles were equipped with pressure orifices. A sketch of the model is shown in Figure 1.

The model was equipped with removable flaps, wings, empennage, vectored-thrust engine nacelles, and a lift jet to determine the contribution of each component to the total aerodynamics. The vectored-thrust engine simulators, which were mounted in fuselage-supported nacelles, were of the ejector type which induced inlet flow. The vectored-thrust jet exits could be mounted 13.1 cm (5.17 in.) below the wing plane at the $0.11\bar{c}$ or $1.11\bar{c}$. The exit diameter was 9.2 cm (3.67 in.). The vectored-thrust jet exits could be deflected downwash at angles of 0° , 45° , and 90° from the horizontal plane.

The model was also equipped with a lift-jet simulator located 16.8 cm (6.63 in.) below the wing plane at the $-0.11\bar{c}$. The simulator was a simple convergent nozzle without an external air intake. The lift jet was limited to exhausting at 90° from the horizontal plane. The lift-jet exit was 5.7 cm (2.25 in.) in diameter. A total pressure probe and a static pressure orifice were installed in the lift-jet exit.

The difference between the two pressures was a reference exit dynamic pressure that was used for the thrust calibrations of the lift jet.

A 45° partial-span flap could be installed on the wing to determine the effect of flaps. The flap chord was 20 percent of the local wing chord. Chordwise rows of pressure orifices were located on the left wing at the 25-, 39-, 52-, and 80-percent semispan locations. The inboard row coincided with the centerline of the vectored-thrust jet exit. The vectored-thrust nacelles covered up some of the orifices so complete measurements of the pressures there were not always available. Also, pressure orifices were located on the bottom of the fuselage in three longitudinal rows and on top and bottom of the vectored-thrust nacelles. Three basic thrust configurations were investigated: the lift-jet configuration; the front vectored-thrust configuration; and the rear vectored-thrust configuration. Photographs of these three configurations are presented in Figure 2.

CHAPTER V

TESTS AND PROCEDURES

Before the model was tested at forward speeds, the thrust of each engine simulator was calibrated statically. Details of the calibration procedure can be found in Reference [15].

Experiment has shown that a jet exhausting into quiescent surroundings will induce flow towards the jet. This induced flow induces a pressure change on nearby surfaces. To minimize the induced effects when calibrating each engine simulator, the engine simulator was mounted on the bare backbone of the model. The forces and moments from the engine simulator were measured with a six-component strain-gage balance (see Fig. 3). The load range and the accuracy of the balance is shown in Table I. High-pressure air was fed to a plenum chamber mounted on the balance. The plenum chamber supplied air to the vectored-thrust engine simulators and the lift-jet simulator. At static conditions, the resultant force or thrust of the jet was calibrated as a function of a reference pressure. For the vectored-thrust engines, the engine plenum pressure was used as the reference pressure; for the lift jet, the lift-jet exit dynamic pressure was used as the reference pressure. The static calibration was used to obtain the experimental nozzle-deflection angle δ_j (or the angle of the thrust vector), and the location of the thrust vector. From the reference pressure and the static calibration, the

forces and moments due to the static thrust can be computed at forward speeds and can, therefore, be removed from the powered data.

The model was then tested in the Langley Research Center's V/STOL tunnel. Data were obtained with the power on at several heights above the tunnel floor. The minimum height for the model to be out of ground effect was defined as the minimum height where there were no changes in the data with increasing distance from the ground. (See Ref. [16].) All subsequent testing was done with the model at a height which was greater than or equal to this minimum height.

Data were obtained both power on and power off through angle-of-attack ranges and power on through effective velocity ratio ranges. The effective velocity ratio was determined using an effective jet-exit area. The effective area A_j was the sum of the exit areas of the thrust devices in use - the right and left vectored-thrust jets and/or the lift jet. The effective velocity ratio was determined from the following expression:

$$v_e = \sqrt{\frac{q_\infty}{q_j}} = \sqrt{\frac{q_\infty}{\frac{T}{2A_j}}} \quad (1)$$

From the definition of the thrust coefficient, the relationship between thrust coefficient and effective velocity ratio can be determined

$$C_T = \frac{2A_j}{S} \frac{1}{v_e^2} \quad (2)$$

The variation of thrust coefficient with velocity ratio is presented in Figure 4 for the vectored-thrust jets and the lift jet. To determine the interference effects of power, the unpowered aerodynamics and the direct-thrust contributions were removed from the power-on data. These direct-thrust contributions were obtained from the engine static calibrations. The thrust-removed data (distinguished with the subscript T) were obtained by subtracting the direct-thrust effects from the basic data. For example,

$$C_{L_T} = C_L \Big|_{\alpha} - C_T \sin (\alpha + \delta_j) \quad (3)$$

The interference increments were represented by a Δ . It should be noted that positive value of interference would imply beneficial interference. The interference was obtained by removing the unpowered component from the thrust-removed data. For example,

$$\Delta C_L = C_{L_T} \Big|_{\alpha} - C_L \Big|_{\alpha, \text{power off}} \quad (4)$$

Three basic thrust configurations were tested: the lift jet, the front vectored-thrust jets deflected 90° , and the rear vectored-thrust jets deflected 90° . Data were measured on the fuselage alone, on the fuselage with the nacelles, and on the fuselage and nacelles with the wing and flaps. Only the results from these three thrust configurations will be discussed herein. The results for the other thrust configurations and the horizontal tail effects can be found in References [16] and [17].

CHAPTER VI

DISCUSSION OF EXPERIMENTAL RESULTS

The data presented in this report have been resolved into the stability-axes system with the moment reference center at the quarter chord of the mean aerodynamic chord. (See Fig. 5.) The thrust was the resultant force from the jets and is not related to a particular axis system. Physical quantities are presented in the SI units and parenthetically in the U.S. Customary Units.

The results of the wind-tunnel investigation are presented in two basic ways: (1) in terms of conventional aerodynamic coefficients and (2) in terms of force-thrust ratios. Force-thrust ratios serve two purposes. They can be used to determine the load sharing between the wing and the jet, and they can represent data continuously from hover to large forward speeds with reasonably sized numbers. Because the effective velocity ratio is the parameter used in describing the jet and its effects, it was chosen instead of thrust coefficient for presentation of results. The variation of the aerodynamic parameters with effective velocity ratio has been used in many experimental reports. For these reasons, the interference data are presented against effective velocity ratio. The results are presented as follows:

	<u>Figures</u>
Experimental results for the lift-jet configuration	6 - 11
Experimental results for the front vectored-thrust configuration	12 - 17
Experimental results for the rear vectored-thrust configuration	18 - 23
Experimental results for the rear vectored-thrust configuration with flaps.	24 - 25
Experimental results for the fuselage with the lift jet.	26 - 27
Experimental results for the fuselage with the front vectored-thrust jets.	28 - 29
Comparison of experimental and theoretical results of the interference on the wing.	30 - 33

In the transition-speed regime of VTOL aircraft, the location of the jet exhaust has a large effect on the pressures and, consequently, the forces on the aircraft. The three jet-exhaust locations used in this investigation were the lift jet, front vectored-thrust jets, and rear vectored-thrust jets. (See Fig. 2.) These locations show many of the problems of VTOL aircraft.

Lift-Jet Configuration

The basic wing-body configuration was tested with the lift jet. The basic aerodynamic data are presented in Figure 6 with the power off ($C_T = 0$) and with the power on at three different C_T settings.

As would be expected, increasing the thrust coefficient increases the lift and the pitching-moment coefficients since the thrust vector is in front of the model moment reference center. The observed changes in pitching moment are small and do not present a trim problem.

Increasing the thrust also decreases the lift-curve slope. A small part of this change arises from a direct thrust effect. The component of thrust in the lift direction is

$$C_{L(\text{Thrust})} = C_T \sin (\alpha + \delta_j) \quad (5)$$

and its derivative with respect to angle of attack is

$$\frac{dC_{L(\text{Thrust})}}{d\alpha} = C_T \cos (\alpha + \delta_j) \quad (6)$$

Increasing the thrust increases the pitching-moment slope. This is not a direct thrust effect because the thrust acts over a constant arm l .

The pitching moment due to thrust is

$$C_{m(\text{Thrust})} = C_T \frac{l}{c} \quad (7)$$

which is independent of angle of attack.

The jet induces a local downwash which allows the wing to operate at a higher geometric angle of attack before stalling. This stall angle increases with decreasing effective velocity ratio. This is more readily apparent from the wing pressure data shown in Figure 7. The pressure profile across the wing chord is presented at four spanwise stations.

For clarity, only part of the angle-of-attack data is presented. Without power at 0° geometric angle of attack, the model sees a slightly positive local angle of attack inboard which decreases outboard. (See Fig. 7(a).) This is indicated by the positive pressure coefficients on the lower surface and negative pressure coefficients on the upper surface of the leading edge of the symmetrical airfoil. This flow-direction change is caused by the interference of the fuselage. As expected, the leading-edge negative pressures increase with angle of attack. The loss of the large negative pressure peak at 12° angle of attack indicates that the wing has stalled.

With power on (Figs. 7(b) and 7(c)), the pressure profiles are changed significantly. At 0° angle of attack, the pressures near the leading edge on the lower surface are less than on the upper surface. This means that the wing is in a downwash field due to the jet. Note that the effects are greatest at the smallest effective velocity ratio (largest thrust coefficient) and at the locations nearest the jet exit ($\eta = 0.25$). The large negative pressure peak on the upper surface at 12° angle of attack indicates the wing has not yet stalled which agrees with the results from force data in Figure 6.

The basic aerodynamic data from Figure 6 had very large lift coefficients at low effective velocity ratios. At low velocity ratios, the jet effects tend to dominate the aerodynamic effects. This implies that most of the lift comes from the jet. When this is the case, conventional aerodynamic coefficients can be misleading. An alternative method for presenting the data is a force-thrust ratio which puts emphasis on

the wing-jet lift sharing. The ratios are obtained by dividing the conventional aerodynamic coefficients by the thrust coefficient. These force-thrust ratios have the added advantage that they are defined at hover or zero forward speed. The basic data are presented in terms of force-thrust ratios through the effective velocity ratio range in Figure 8. The lift-thrust ratio is a type of "lift efficiency." For example, a configuration with 90° jets at zero lift coefficient and angle of attack should have the lift equal to the thrust; the lift-thrust ratio should be 1.0. This would be true if there were no interference effects. Note that the lift-jet configuration has a poor "lift efficiency" at 0° angle of attack. The jet is lifting, but the wing and fuselage are pushing down. At 10° angle of attack, the wing and fuselage are lifting as is indicated from the lift-thrust ratios greater than 1.0.

The pitching-moment thrust ratio indicates that the lift jet has a pitch-up problem which is similar to the results found in References [2] and [3]. As forward speed V_e increases, the nose-up pitching moment increases. This creates a trim problem for the pilot.

Because the direct-thrust effects can disguise the wing aerodynamics, these effects have been removed from the data. The results are presented in Figure 9. If there were no interference effects, the thrust-removed power-on data should collapse on top of the power-off data; however, this is not generally the case. The most striking result is that all the thrust-removed lift coefficients are less than the power-off lift coefficients. As the velocity ratio decreases, the difference between

power off and power on increases. The thrust-removed lift-curve slopes decrease with decreasing effective velocity ratio (increasing thrust coefficient). The thrust-removed pitching moments do not show the same trend that the lift coefficient showed. The difference between the power off and power on increases with decreasing velocity ratio for velocity ratios of 0.3 and 0.2; however, the opposite is true for the effective velocity of 0.1.

The differences between the thrust-removed power-on data and the power-off data are defined as the interference effects. These interference effects arise from both the fuselage and the wing. The interference effects are presented through the angle-of-attack range in Figure 10 and through the effective velocity ratio range in Figure 11.

Because the aerodynamic coefficients lose their significance at low speeds, the interference has been divided by thrust coefficient. The lift interference is detrimental at all angles of attack and effective velocity ratios tested. The interference is strongly dependent on effective velocity ratio and weakly dependent on angle of attack. The detrimental interference becomes larger as the velocity ratio increases (thrust coefficient decreases). As the velocity ratio increases, the jet is turned downstream closer to the fuselage interfering with the flow there.

Front Vectored-Thrust Configuration

The wing-body configuration was tested with the vectored-thrust nacelles with the jet exits in the front position and the nozzles

deflected 90° . The basic aerodynamic results are presented in Figure 12. The trends are very similar to those found with the lift-jet configuration but the effects are larger. Because the exit areas are different for the lift-jet and vectored-thrust configurations, care should be used when comparing the different configurations. Although the data were obtained at the same velocity ratios, the thrust coefficients are different. (See Fig. 4.) The lift and the pitching moment for the front vectored-thrust jets increase with decreasing velocity ratio. The stall angle also increases with decreasing effective velocity ratio. In the linear angle-of-attack range, the lift-curve slope decreases, and the pitching-moment slopes increase with increasing velocity ratio. An explanation for these results can be deduced from the pressure data.

The pressure data for the front vectored-thrust configuration are shown in Figure 13. The pressure distribution at $\eta = 0.39$ was integrated power off (Fig. 13(a)) through the angle-of-attack range to obtain the section-lift coefficient. The same procedure was followed for the power-on data (Fig. 13(b)). Comparison of the section-lift coefficients showed the wing to be operating at a local angle of attack of about 1.5° less than the geometric angle of attack. This downwash from the jet allows the geometric angle of attack to be larger before stall with the power on than the power off. A comparison of Figure 13(a) with 13(b) or 13(c) shows large effects of power. The most noticeable effect is the large region of negative pressures on the lower surface which are not very sensitive to changes in angle of attack. Apparently, the large velocity at the exit tends to dominate the local flow field near the exit

regardless of the angle of attack. These induced pressures are caused by the jet's exhaust entraining flow away from the wing.

The effect of effective velocity ratio on the force-thrust ratios for the front vectored-thrust jets is shown in Figure 14. At hover, there is a lift loss from the entrainment of flow into the jet. The basic data show trends different from the lift jet. At low effective velocity ratios for both 0° and 10° angle of attack, the lift efficiency C_L/C_T is less than 1.0. This effect is attributed to the jets drawing flow from the wing's lower surface. At the higher velocity ratios, the aerodynamic effects increase and the lift efficiency is greater than 1.0. The effects on the pitching moment are similar to those of the lift jet. There is the same pitch-up problem with increasing forward speed.

The thrust-removed data are presented in Figure 15. The most striking result is the large negative lift coefficients at an effective velocity ratio of 0.1. Most of the negative lift is produced by the large region of negative pressure coefficients on the lower surface of the wing near the jet. There is a large difference (about 0.3 or 0.4) between the aerodynamic pitching-moments power on and power off. This large difference was not present for the lift-jet configuration where the largest difference was about 0.1.

The interference effects are presented through an angle-of-attack range in Figure 16 and through an effective velocity ratio range in Figure 17. At small effective velocity ratios, the trends are the same as those found for the lift-jet configuration. The induced effects are not strongly dependent of angle of attack in the linear range. At higher

velocity ratios, the lift interference is beneficial for the front vectored-thrust jets.

Rear Vectored-Thrust Configuration

The wing-body was tested with the vectored-thrust nacelles in the rear position with the nozzles deflected 90° . The basic results, presented in Figure 18, are similar to those from the front vectored-thrust configuration; however, there were two differences. At a given velocity ratio (thrust coefficient), the lift coefficients are greater and the pitching moments had large negative values. The negative pitching moments are caused by the large distance between the thrust line and the moment reference center. The increase in lift can be explained using the pressure data.

The pressure data are presented in Figure 19. The major difference between the front location (Figs. 13(b) or 13(c)) and the rear location (Figs. 19(b) or 19(c)) is the reduction of the region of negative pressures near the jet. This reduced download allowed the lift to increase.

The force-thrust data are presented in Figure 20. The lift efficiency shows a small lift loss at small velocity ratios at 0° angle of attack. At a given ratio, the efficiency is greater than it was for the front vectored-thrust jets. The large, nose-down pitching moment poses a severe trim problem. If this configuration could be trimmed, it would still have a pitch-up problem because C_m/C_T increases with effective velocity ratio. This pitch up is smaller than the pitch up for the front vectored-thrust jets.

The thrust-removed data are presented in Figure 21. The power-on, thrust-removed lift is greater than the power-off lift at velocity ratios of 0.2 and 0.3. This is in sharp contrast to the results from the front vectored-thrust configuration (see Fig. 15). The aerodynamic pitching moments are greater power on than power off, and the difference increases with decreasing effective velocity ratio.

The interference data for the rear vectored-thrust jets are presented in Figure 22 for an angle-of-attack range and in Figure 23 for an effective velocity ratio range. The vectored-thrust jets do cause a detrimental lift interference at very low effective velocity ratios, but the magnitude is much smaller than for the front vectored-thrust jets. At velocity ratios of 0.2 and above, the interference is beneficial. Shifting the vectored-thrust jet exits rearward significantly affected the interference. This beneficial interference could be caused by a supercirculation or jet-flap effect by the jet at the trailing edge. As was previously mentioned, this benefit comes with a severe penalty - the large nose-down pitching moment from the jet's thrust. One method of solving the problem would be to combine the favorable rear vectored-thrust jet configuration with the lift-jet-configuration. This would be similar to the lift-plus-lift-cruise concept mentioned previously.

Rear Vectored-Thrust Configuration with Flaps

A rather simple method to increase the lift is to add flaps to the wing. The basic aerodynamic characteristics of the rear vectored-thrust configuration with flaps deflected is presented in Figure 24.

As expected, installing the flaps increased the lift and made the pitching moment more negative. Although the changes in lift and pitching moment are small compared to the total values, they are nonetheless important. The increase in lift due to flap deflection does not carry this severe pitching-moment penalty that the rear vectored-thrust jet had. This can be more easily seen by examining the interference data which are presented in Figure 25. Adding the flaps brought about a small beneficial change in the interference for the rear vectored-thrust configuration. For the rear jets, the jet exhaust entrains flow over the flap which delays separation. Without this entrained flow, the free-stream flow would separate from the upper surface, and the lift would be less than it would be without separation.

Interference on the Fuselage

The fuselage without the wings was tested with the lift jet and with the front vectored-thrust jets. By testing the fuselage alone and with the vectored-thrust jets, the aerodynamics and the interference of each component can be calculated. To simplify comparisons, the wing area was used to obtain lift and pitching-moment coefficients. The basic data of the fuselage with the lift jet are presented in Figure 26. At 0° angle of attack, the lift and pitching moment were 0 with power off. This is to be expected for the nearly symmetrical fuselage. The lift coefficient and pitching-moment coefficient increase with angle of attack with the power off. With power-on, the lift level increases relative to power off; however, the lift decreases with angle of attack for $V_e < 0.3$.

Because the model moment reference center is behind the jet, the pitching moment increases with thrust.

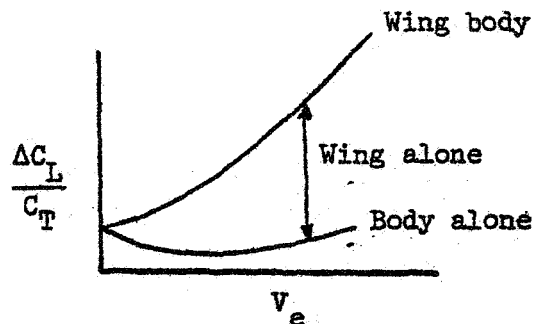
The jet-induced interference on the fuselage through an effective velocity ratio range is presented in Figure 27. There is a detrimental lift interference which increases with increasing effective velocity ratio. This is expected because of the separated flow region behind the jet and the proximity of the jet's path to the fuselage.

The basic data for the fuselage with the front vectored-thrust nacelles are presented in Figure 28. The trends are similar to those obtained for the lift jet except the effects are larger because of the different exit areas and thrust coefficients. Without power, the lift and pitching moment increase with angle of attack. The nacelles are producing lift ahead of the moment reference center. The interference on the fuselage with the front vectored-thrust jets is presented in Figure 29. The interference in lift decreases slightly and then increases with increasing velocity ratio. There is a relatively small difference for 0° and 10° angle of attack in the lift interference. The interference in pitching moment increases with increasing effective velocity ratio.

Comparison of Theory and Experiment

The jet flow-field program and the lifting-surface program (Wooler's method) predict the interference effects on the wing alone. The wind-tunnel model that was used in this investigation could not be tested with the wing alone. The results presented in Figures 11, 17, 23,

and 25 are for the wing-body configuration. An examination of the high-pressure air system needed for the jet makes it extremely difficult to build a model for obtaining wing-alone data. The theoretical data from Wooler's method are for the wing alone and should not be compared directly with the wing-body data. Since there are no theoretical methods to evaluate the interference on a wing-body configuration, the experimental data must be manipulated to obtain wing-alone data. It is assumed that the total interference can be divided up into a wing part, a fuselage part, and a mutual wing-body interference part. The fuselage part was measured experimentally and was presented in Figures 27 and 29. The mutual interference between the wing and the fuselage was calculated to be about 6 percent using the methods described in Reference 18. If this mutual interference is neglected, the interference on the wing can be obtained by subtracting the fuselage (and nacelles when installed) data from the fuselage wing data as shown in the following sketch:



Interference effects on the wing. - The experimental and theoretical interference effects induced by the lift jet on the wing alone are

presented in Figure 30. The experimental results show a detrimental lift interference which worsens with increasing effective velocity ratio. The interference in pitching moment is very small. The theoretical results are in reasonable agreement with the experimental results in both the magnitude and the trends. The theoretical interference in pitching moment at 0° angle of attack was so close to 0 that it did not show up on the scales used. A possible explanation is that the lift-jet wake affected the fuselage but not the wing. The potential-flow model appears to be representative for this case.

The interference effects induced on the wing by the front vectored-thrust jets are presented in Figure 31. The experimental results show a lift loss at small effective velocity ratios which becomes a lift augmentation as the effective velocity ratio increases. The theoretical results show the correct trends although the magnitudes differ.

The fuselage alone was not tested with the rear vectored-thrust jets because the region of the fuselage affected by the jet in the front or the rear position was relatively small compared to the total length of the fuselage. The interference in lift should not drastically change with a small change in jet location. Therefore, to obtain the interference effects on the wing from the rear vectored-thrust jets, the interference data on the fuselage alone for the front vectored-thrust jets was subtracted from the interference data for the wing body with the rear vectored-thrust jets. These results are presented in Figure 32. The experimental lift interference is beneficial through most of the

effective velocity ratio range. The theoretical results show the correct trends for lift but not for the pitching moment. A possible reason for the difference in pitching moment is the use of data for the front vectored-thrust jets with the fuselage alone to obtain the wing-alone data for the rear vectored-thrust jets. The surface area primarily affected by the jet interference was about the same for the front and the rear vectored-thrust jets. The location of this surface area is different. Therefore, the interference in lift is similar for the two jet locations, but the interference in pitching moment is not similar because of the difference in location.

Interference effects on the wing with flaps. - The interference effects on the wing with flaps are presented in Figure 33. The experimental interference in lift is beneficial through the angle-of-attack range. The theoretical results were obtained from the lifting-surface program which was modified to handle the partial-span flaps. The theoretical lift interference shows the right trends, but the magnitude differs. The pitching-moment interference does not show the correct trends for the same reasons previously discussed.

CHAPTER VII

CONCLUSIONS

The results from this investigation show some basic characteristics of the jet and its interference. The jet effects are strongest at the lowest effective velocity ratios (highest thrust coefficients) and at the location nearest the jet. The jet-induced effects are strongly dependent on effective velocity ratio and weakly dependent on angle of attack. For the lift jet, the lift interference was detrimental on both the wing and the fuselage. For the vectored-thrust configurations, the lift interference was detrimental at low effective velocity ratios and beneficial at high effective velocity ratios. The interference on the rear vectored-thrust configurations was more beneficial (or less detrimental) than the front vectored-thrust configuration. This came at the expense of a severe nose-down pitching moment. The flaps provided an increase in lift with an increase in beneficial lift interference and without any severe penalty in pitching moment.

The assumption of neglecting mutual wing-body fuselage interference appears to have been warranted. The theoretical results generally predict the correct trends and the levels are the right order of magnitude. However, in view of the comparisons between the theory and experimental data taken in the present investigation, the Wooler method is only a first step in developing a complete prediction method.

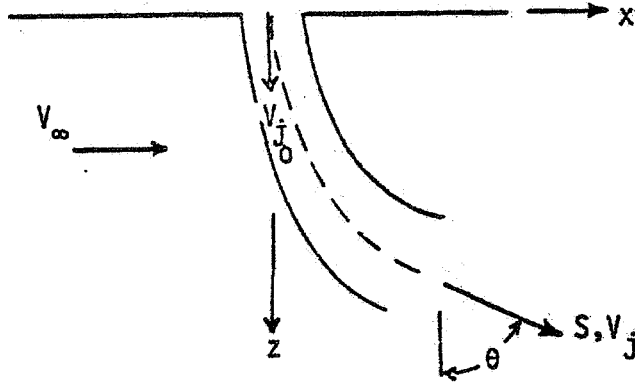
The deficiencies in the method are believed to be in the jet flow-field program and not in the lifting-surface program. The deficiencies are related to how well the four characteristics of the jet are modeled. The method does not account for the separated region behind the jet. It does account for the blockage and entrainment with the empirical constants in the entrainment equations. The method might be improved by better modeling of these nonpotential flow effects.

APPENDIX

DERIVATIONS OF THE JET FLOW-FIELD AND LIFTING-SURFACE THEORIES

Jet Flow-Field Theory

The development of the jet flow-field theory uses three basic equations of motion. They are the continuity equation, momentum equation, and Newton's law. To simplify the computations, the jet density is assumed to be equal to the free-stream density. The following sketch describes the symbols used in the derivation:



The continuity equation for a differential length of the jet is

$$E = \rho \frac{d}{ds} (A_j V_j) \quad (1A)$$

where E is the entrainment of flow per unit length of the jet.

The momentum equation for a differential length of the jet in the direction tangent to the jet may be written

$$E V_{\infty} \sin\theta = \rho \frac{d}{ds} (A_j V_j^2) \quad (2A)$$

The sum of the forces perpendicular to the jet should equal the product of the mass of the jet and its acceleration towards the center of a circle. The two forces perpendicular to the jet arise from the change in velocity from the viscous entrainment and the force on the jet boundary from the free stream. Newton's law may be written

$$E V_{\infty} \cos\theta + F_B = \rho \frac{A_j V_j^2}{R} \quad (3A)$$

where R is jet curvature. The body force on the boundary can be represented by the two-dimensional drag coefficient of an ellipse

$$F_B = C_d \frac{1}{2} \rho (V_{\infty} \cos\theta)^2 d \quad (4A)$$

An expression for the entrainment was developed from dimensional considerations. The entrainment per unit length of the jet was assumed to have the following form

$$E = \rho E_1 V_{\infty} d \cos\theta + \frac{\rho E_2 (V_j - V_{\infty} \sin\theta) C}{1 + E_3 \frac{V_{\infty}}{V_j} \cos\theta} \quad (5A)$$

The first term accounts for the flow which is moving perpendicular to the jet and the second term accounts for flow parallel to the jet.

Experimental observations have shown that a circular jet develops into a kidney shape and maintains a geometrically similar shape as it moves downstream. Because it would be difficult to treat a kidney shape

exactly, the shape was simplified into an ellipse. Therefore, the jet is treated in two regions: a developing region in which the jet deforms from a circle to a 4:1 ellipse and a developed region with a 4:1 ellipse. The developing region extends until the jet has penetrated $0.3 \frac{V_{j0}}{V_{\infty}} \frac{z}{d_0}$ into the free stream. The ratio of the depth to the width of the jet decreases linearly from 1 at the exit to 0.25 at the end of the developing region. From geometry, the circumference and the area of the ellipse can be expressed in terms of the ellipse's major axis. In the developing region where $\frac{z}{d_0} < 0.3 \frac{V_{j0}}{V_{\infty}}$

$$C = d\pi \left[\frac{1 + \left(1 - \frac{5}{2} \left(\frac{z}{d_0} \right) \left(\frac{V_{\infty}}{V_{j0}} \right) \right)^2}{2} \right]^{1/2} \quad (6A)$$

$$A_j = \frac{\pi d^2}{4} \left[1 - \frac{5}{2} \left(\frac{z}{d_0} \right) \left(\frac{V_{\infty}}{V_{j0}} \right) \right] \quad (7A)$$

and in the developed region where $\frac{z}{d_0} > 0.3 \frac{V_{j0}}{V_{\infty}}$

$$C = 2.24d \quad (8A)$$

$$A_j = \pi \frac{d^2}{16} \quad (9A)$$

Using these basic equations, the equations for the jet's size, position, and speed may be obtained. Starting with the momentum equation (see eq. (2A)) and by expanding the derivative

$$E V_{\infty} \sin\theta = \rho A_j V_j \frac{d}{ds} (V_j) + \rho V_j \frac{d}{ds} (A_j V_j) \quad (10A)$$

and then by dividing through by V_j

$$E \frac{V_{\infty}}{V_j} \sin\theta = \rho A_j \frac{d}{ds} (V_j) + \rho \frac{d}{ds} (A_j V_j) \quad (11A)$$

The second term on the right-hand side of equation (11A) is identical to the right-hand side of equation (1A). Substituting and collecting terms

$$E \left(\frac{V_{\infty}}{V_j} \sin\theta - 1 \right) = \rho A_j \frac{d}{ds} (V_j) \quad (12A)$$

Replacing $\frac{d}{ds}$ by $\cos\theta \frac{d}{dz}$ and solving for the derivatives

$$\frac{d}{dz} (V_j) = \frac{E \left(\frac{V_{\infty}}{V_j} \sin\theta - 1 \right)}{\rho A_j \cos\theta} \quad (13A)$$

Substituting for the entrainment

$$\frac{d}{dz} (V_j) = \left[\rho E_1 V_{\infty} d \cos\theta + \frac{\rho E_2 (V_j - V_{\infty} \sin\theta) C}{1 + E_3 \frac{V_{\infty}}{V_j} \cos\theta} \right] \frac{\left(\frac{V_{\infty}}{V_j} \sin\theta - 1 \right)}{\rho A_j \cos\theta} \quad (14A)$$

Starting with the continuity equation (see eq. (1A)) and by expanding the derivatives and replacing $\frac{d}{ds}$ by $\cos\theta \frac{d}{dz}$

$$E = \rho \cos\theta \left[A_j \frac{d}{dz} (V_j) + V_j \frac{d}{dz} (A_j) \right] \quad (15A)$$

and solving for the derivative

$$\frac{d}{dz} (A_j) = \frac{E}{\rho V_j \cos\theta} - \frac{A_j}{V_j} \frac{d}{dz} (V_j) \quad (16A)$$

Substituting for the entrainment

$$\frac{d}{dz} (A_j) = \left[\rho E_1 V_\infty d \cos\theta + \frac{\rho E_2 (V_j - V_\infty \sin\theta) C}{1 + E_3 \frac{V_\infty}{V_j} \cos\theta} \right] \frac{1}{\rho V_\infty \cos\theta} - \frac{A_j}{V_j} \frac{d}{dz} (V_j) \quad (17A)$$

Starting with Newton's law (see eq. (3A)), the radius of curvature may be expressed in terms of its first and second derivative

$$R = \frac{\left[1 + \left(\frac{dx}{dz} \right)^2 \right]^{3/2}}{\left(\frac{d^2x}{dz^2} \right)} \quad (18A)$$

Substituting for the entrainment and the body force

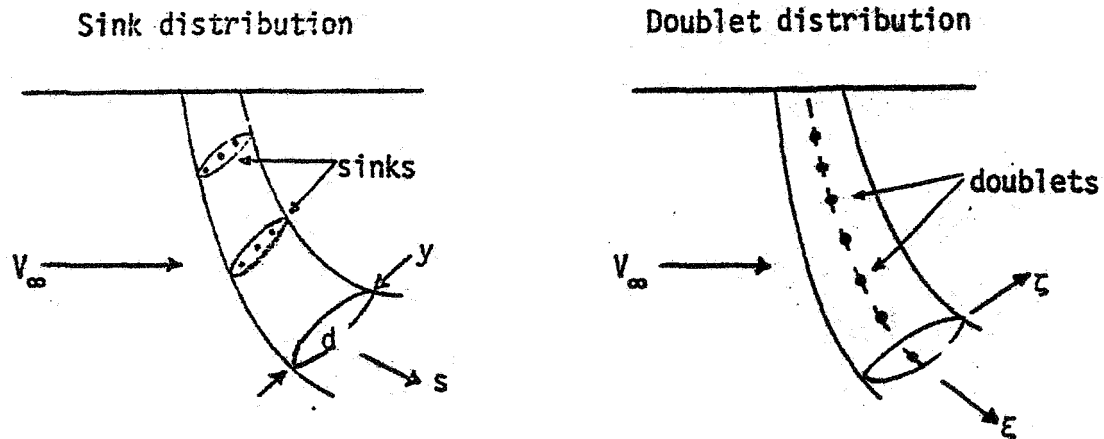
$$\frac{\frac{d^2x}{dz^2}}{\left[1 + \left(\frac{dx}{dz} \right)^2 \right]^{3/2}} = \left[E_1 V_\infty d \cos\theta + \frac{E_2 (V_j - V_\infty \sin\theta) C}{1 + E_3 \frac{V_\infty}{V_j} \cos\theta} \right] \frac{V_\infty \cos\theta}{A_j V_j^2} + \frac{C_d \frac{1}{2} V_\infty^2 \cos^2\theta d}{A_j V_j^2} \quad (19A)$$

The problem reduces to solving three differential equations (eqs. (14A), (17A), and (19A)) for the jet's downstream position, velocity, and diameter in terms of its penetration. However, the entrainment parameters (E_1 , E_2 , and E_3) and the cross-flow drag coefficient are still unknown. The values for the entrainment parameters were chosen for good correlation of experimental data. The drag coefficient of an ellipse was obtained from Reference [19].

$$C_d = \frac{1}{6} \left[-\frac{1}{D^2} + \frac{6.6}{D} + .4 \right] \quad (20A)$$

where D is the ratio of the ellipse major axis to minor axis.

The three differential equations (eqs. (14A), (17A), and (19A)) were numerically integrated using the Runge-Kutta method. Once the jet path was known, the jet was replaced by a doublet distribution to represent the blockage and a sink distribution to represent the entrainment as shown in the following sketch.



The sink strength per unit distance is the entrainment divided by the jet diameter

$$m = \frac{E}{d} ds \quad (21A)$$

The velocity potential for a sink dy long is

$$\phi = -\frac{m}{4\pi r} dy \quad (22A)$$

The velocity components induced by the sink at a point $p (x_p, y_p, z_p)$ are

$$du_s = -\frac{\partial \phi}{\partial x} = \frac{m dy (x - x_p)}{4\pi [(z - z_p)^2 + (x - x_p)^2 + (y_p + y)^2]^{3/2}} \quad (23A)$$

$$dv_s = -\frac{\partial \phi}{\partial y} = \frac{m dy (y + y_p)}{4\pi [(z - z_p)^2 + (x - x_p)^2 + (y_p + y)^2]^{3/2}} \quad (24A)$$

$$dw_s = -\frac{\partial \phi}{\partial z} = \frac{m dy (z - z_p)}{4\pi [(z - z_p)^2 + (x - x_p)^2 + (y_p + y)^2]^{3/2}} \quad (25A)$$

Integrating the induced velocity across the length of the jet yields

$$u_s = -\frac{m}{4\pi} \frac{x - x_p}{(z - z_p)^2 + (x - x_p)^2} \left[\frac{y_p - \frac{d}{2}}{[(z - z_p)^2 + (x - x_p)^2 + (y_p - \frac{d}{2})^2]^{1/2}} - \frac{y_p + \frac{d}{2}}{[(z - z_p)^2 + (x - x_p)^2 + (y_p + \frac{d}{2})^2]^{1/2}} \right] \quad (26A)$$

$$v_s = -\frac{m}{4\pi} \left[\frac{1}{\left[(z-z_p)^2 + (x-x_p)^2 + \left(y - \frac{d}{2}\right)^2 \right]^{1/2}} - \frac{1}{\left[(z-z_p)^2 + (x-x_p)^2 + \left(y_p + \frac{d}{2}\right)^2 \right]^{1/2}} \right] \quad (27A)$$

$$w_s = -\frac{m}{4\pi} \frac{z - z_p}{(z-z_p)^2 + (x-x_p)^2} \left[\frac{y_p - \frac{d}{2}}{\left[(z-z_p)^2 + (x-x_p)^2 + \left(y_p - \frac{d}{2}\right)^2 \right]^{1/2}} - \frac{y_p + \frac{d}{2}}{\left[(z-z_p)^2 + (x-x_p)^2 + \left(y_p + \frac{d}{2}\right)^2 \right]^{1/2}} \right] \quad (28A)$$

The strength of the doublet distribution is obtained from the complex velocity potential for the two-dimensional flow past an ellipse

$$\mu = \frac{1}{2} V_\infty \cos\theta (a+b) b \quad (29A)$$

The velocity potential of a doublet is

$$\phi = \frac{2\mu x}{4\pi r^3} \quad (30A)$$

The components of velocity induced by the doublet are

$$u_i = -\frac{\partial\phi}{\partial\xi} = \frac{-6\xi\zeta\mu}{4\pi (\xi^2 + \zeta^2 + \eta^2)^{5/2}} \quad (31A)$$

$$v_i = -\frac{\partial \phi}{\partial \eta} = \frac{-6\eta\xi\mu}{4\pi(\xi^2 + \eta^2 + \zeta^2)^{5/2}} \quad (32A)$$

$$w_i = -\frac{\partial \phi}{\partial \zeta} = \frac{2\mu}{4\pi(\xi^2 + \eta^2 + \zeta^2)^{3/2}} \left[1 - \frac{3\zeta}{(\xi^2 + \eta^2 + \zeta^2)} \right] \quad (33A)$$

These components can be resolved into the X, Y, and Z axis system

$$u_d = u_i \sin\theta + w_i \cos\theta \quad (34A)$$

$$v_d = -v_i \quad (35A)$$

$$w_d = u_i \cos\theta - w_i \sin\theta \quad (36A)$$

The induced velocity components from the sinks and the doublets are summed at each control point and nondimensionalized by the free-stream velocity.

Lifting-Surface Theory

The lifting-surface theory which is discussed in Reference 7 is based on a kernel function procedure. The basic equation is

$$\frac{w(x,y)}{V} = \frac{c_0 b}{\pi 16\rho V^2} \int_{\eta=-1}^{\eta=1} \int_{\xi_{L.E.}}^{\xi_{T.E.}} P_R(\xi,\eta) K[x,y,\xi,\eta] d\xi d\eta \quad (37A)$$

This equation related the downwash w on the wing to a pressure loading P_R . The kernel function K is a weighting function which gives the

downwash (x,y) due to a unit load at (ξ,η) . A finite series was used to represent the pressure function

$$P_R(\theta,\eta) = \frac{8\pi b}{c} \sqrt{1-\eta^2} \sum_{n=0}^{N-1} \sum_{m=1}^M a_{np} \eta^p \ell_n(\theta) \quad (38A)$$

where $p = 2(m-1)$

$$\ell_n(\theta) = \cos \frac{\theta}{2} \text{ for } n=0 \quad (39A)$$

$$\ell_n(\theta) = \frac{4}{2^{2n}} \sin(n\theta) \text{ for } n>1 \quad (40A)$$

$$\xi = \xi_m - \frac{c}{c_0} \cos\theta \quad (41A)$$

The kernel function was simplified to steady flow

$$K = 1 + \frac{x_0}{\sqrt{x_0^2 + \beta^2 s^2 (y-\eta)^2}} \quad (42A)$$

Substituting equations (38A) and (42A) into equation (37A)

$$\frac{w(x,y)}{v} = \sum_{n=0}^{N-1} \sum_{m=1}^M \int_{\eta=-1}^{\eta=1} \frac{a_{np} \eta^p \sqrt{1-\eta^2}}{(y-\eta)^2} d\eta \int_0^\pi \ell_n(\theta) \quad (43A)$$

$$\left[1 + \frac{x_0}{\sqrt{x_0^2 + \beta^2 s^2 (y-\eta)^2}} \right] \sin\theta d\theta \quad (44A)$$

Equation (44A) was integrated using Gauss' method of numerical integration. The integration yielded an equation of the form

$$\frac{w(x,y)}{v} = \sum_{n=0}^{N-1} \sum_{m=1}^M d_{np} a_{np} \quad (45A)$$

or in matrix form

$$[w] = [D] [A] \quad (46A)$$

The matrix equation is solved for the coefficients of the pressure matrix. The coefficients are used in equation (38A) to obtain the pressure loading which is integrated to yield the forces and moments on the wing.

Equation (44A) was integrated using Gauss' method of numerical integration. The integration yielded an equation of the form

$$\frac{w(x,y)}{v} = \sum_{n=0}^{N-1} \sum_{m=1}^M d_{np} a_{np} \quad (45A)$$

or in matrix form

$$[w] = [D][A] \quad (46A)$$

The matrix equation is solved for the coefficients of the pressure matrix. The coefficients are used in equation (38A) to obtain the pressure loading which is integrated to yield the forces and moments on the wing.

REFERENCES

- [1] Carter, A. W. Effects of Jet Exhaust Location on the Longitudinal Aerodynamic Characteristics of a Jet V/STOL Model. NASA TN D-5333, July 1969.
- [2] Margason, R. J., Vogler, R. D., and Winston, M. M. Wind-Tunnel Investigation at Low Speeds of a Model of the Kestrel (XV-6A) Vectored-Thrust V/STOL Airplane. NASA TN D-6826, July 1972.
- [3] Margason, R. J. and Gentry, G. L. Aerodynamic Characteristics of a Five Jet VTOL Configuration in the Transition Speed Range. NASA TN D-4812, Oct. 1968.
- [4] Shaw, C. S. and Margason, R. J. An Experimental Investigation of a Highly Underexpanded Sonic Jet Ejecting From a Flat Plate Into a Subsonic Crossflow. NASA TN D-7314, Dec. 1973.
- [5] Wu, J. C., McMahon, H. M., Mosher, D. K., and Wright, M. A. "Experimental and Analytical Investigations of Jets Exhausting Into a Deflecting Stream." AIAA Paper 69-223, Feb. 1969
- [6] Fricke, L. B., Wooler, P. T., and Ziegler, H. Wind-Tunnel Investigation of Jets Exhausting Into a Crossflow. AFFDL TR-70-154, Dec. 1970.
- [7] Margason, R. J. The Path of a Jet Directed at Large Angles to a Subsonic Free Stream. NASA TN D-4919, Nov. 1968.
- [8] Anon. Analysis of a Jet in a Subsonic Crosswind. NASA SP-218, Sep. 1969

- [9] Wooler, P. T., Burghart, G. H., and Gallagher, J. T. "Pressure Distribution on a Rectangular Wing With a Jet Exhausting Normally Into an Airstream." Journal of Aircraft, vol. 4, no. 6, Nov.-Dec. 1967.
- [10] Goldhammer, M. L., Lopez, M. L., and Shen, C. C. Methods for Predicting the Aerodynamic and Stability and Control Characteristics for STOL Aircraft. AFFDL TR-73-146, Dec. 1973.
- [11] Monical, R. E. "A Method of Representing Fan-Wing Combinations for Three Dimensional Potential Flow Solutions." Journal of Aircraft, vol. 2, no. 6, Nov.-Dec. 1965.
- [12] Stevens, J. R., and McDonald, J. W. Subsonic Lifting Surface Design and Analysis Procedure. Bureau of Naval Weapons Rep. NOR-64-195, April 1965.
- [13] Wooler, P. T., Kao, H. C., Schwendemann, M. F., Wasson, H. R., and Ziegler, H. V/STOL Aircraft Aerodynamic Prediction Methods. AFFDL-TR-72-26, vols. I-IV, Jan. 1972
 Vol. I - Theoretical Developments of Prediction Methods
 Vol. II - Application of Prediction Methods.
 Vol. III - Manual for Computer Programs.
 Vol. IV - Literature Survey.
- [14] Ashley, H., and Landahl, M. Aerodynamics of Wings and Bodies. Addison-Wesley Publishing Co., Inc., Reading, Mass., 1965
- [15] Margason, R. J. and Gentry, G. L. Static Calibration of an Ejector Unit for Simulation of Jet Engines in Small Wind Tunnel Models. NASA TN D-3867, March 1967

- [16] Mineck, R. E., and Schwendemann, M. F. Aerodynamic Characteristics of a Vectored-Thrust V/STOL Fighter in the Transition-Speed Range. NASA TN D-7191, May 1973.

- [17] Mineck, R. E., and Margason, R. J. Pressure Distribution on a Vectored-Thrust V/STOL Fighter in the Transition-Speed Range. NASA TM X-2867, March 1974

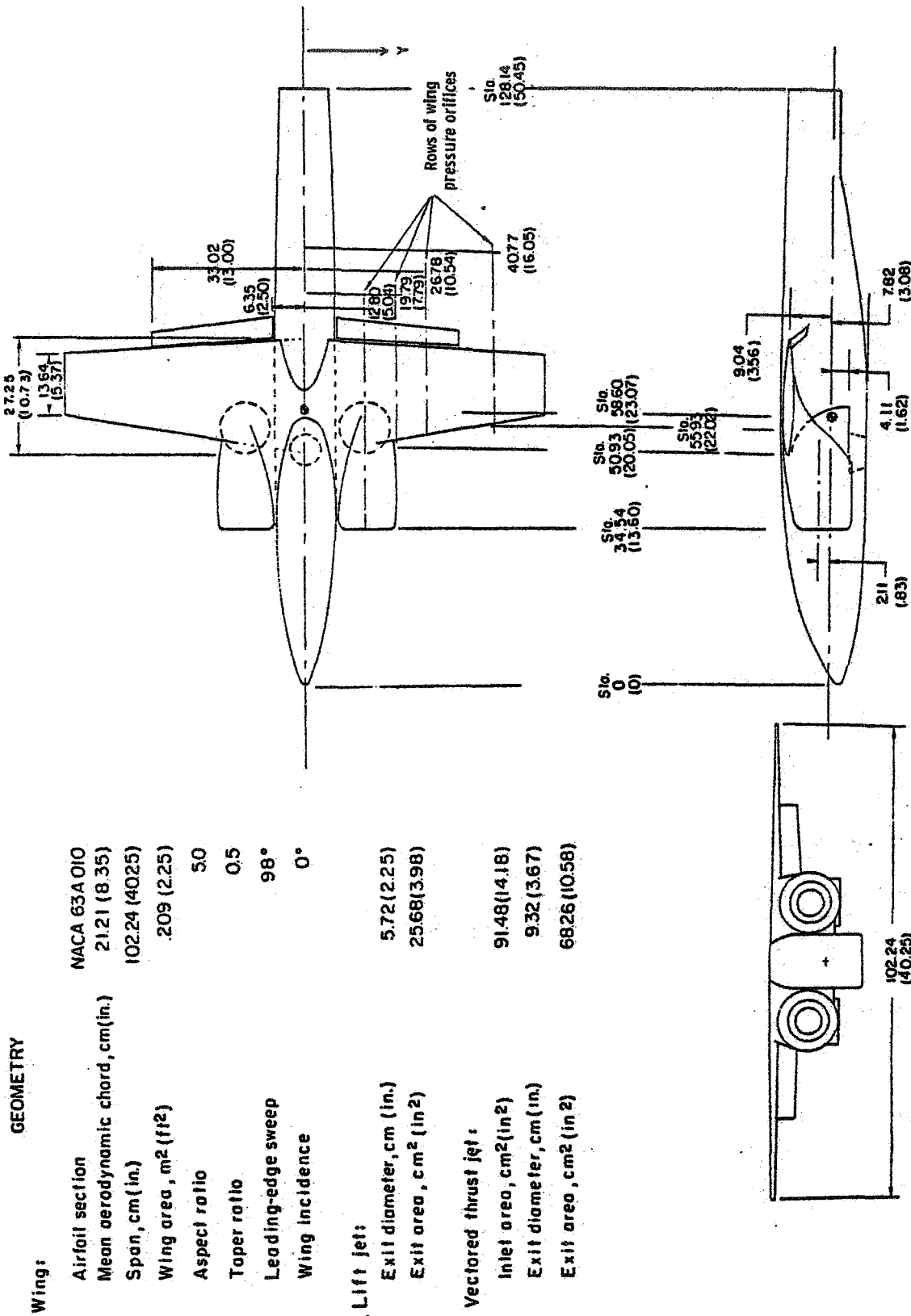
- [18] Pitts, W. C., Nielsen, J. N., and Kaatari, G. E. Lift and Center of Pressure of Wing-Body-Tail Combinations at Subsonic, Transonic, and Supersonic Speed. NACA Rep. 1307, 1957

- [19] Hoerner, S. F. Fluid-Dynamic Drag. S. F. Hoerner (Publisher), Midland, New Jersey, 1965

TABLE

Load Range and Accuracy of the Balance

Balance component	Load range	Accuracy
Normal force	2224 nt (500 lbf)	11.1 nt (2.5 lbf)
Axial force	890 nt (200 lbf)	4.4 nt (1.0 lbf)
Pitching moment	33894 nt cm (3000 in lbf)	169.5 nt cm (15.0 in lbf)
Rolling moment	11298 nt cm (1000 in lbf)	56.5 nt cm (5.0 in lbf)
Yawing moment	22596 nt cm (2000 in lbf)	113.0 nt cm (10.0 in lbf)
Side force	1334 nt (300 lbf)	6.7 nt (1.5 lbf)

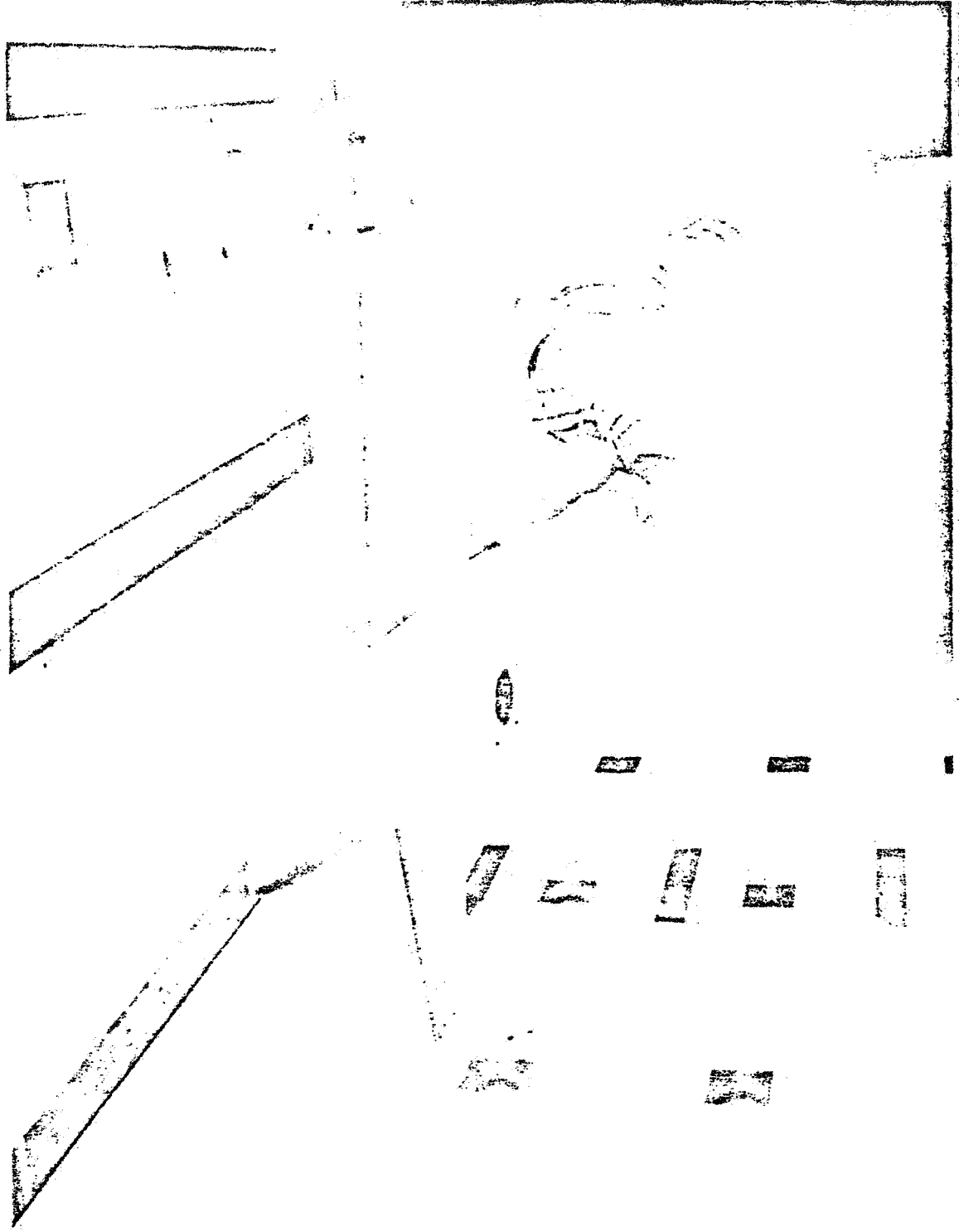


(a) Front vectored-thrust configuration with lift jet and flaps.

Figure 1 - Details of model. All dimensions are in centimeters (inches) unless otherwise noted.



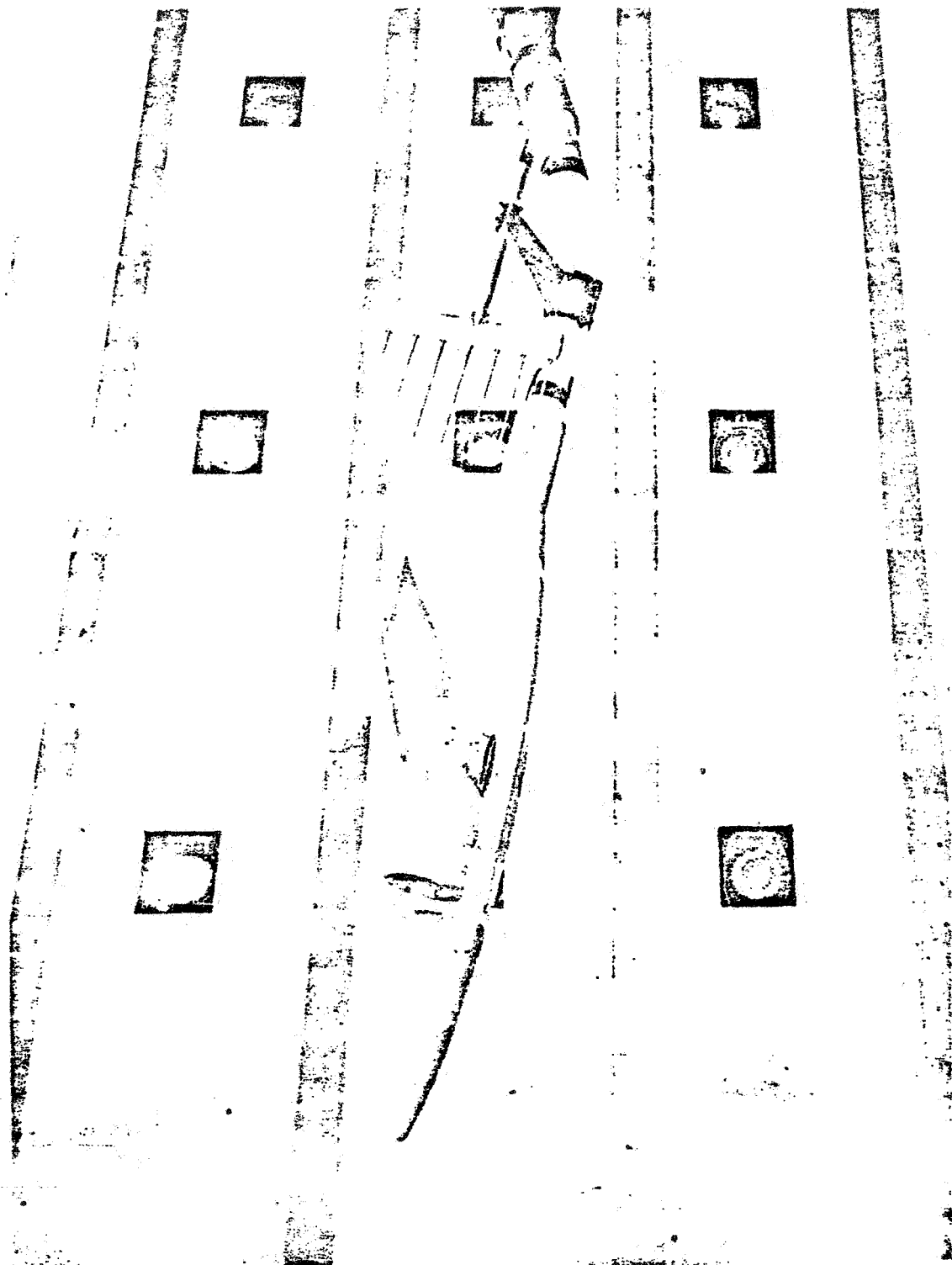
Figure 1.- Concluded.



L-71-3220

(a) Lift-jet configuration.

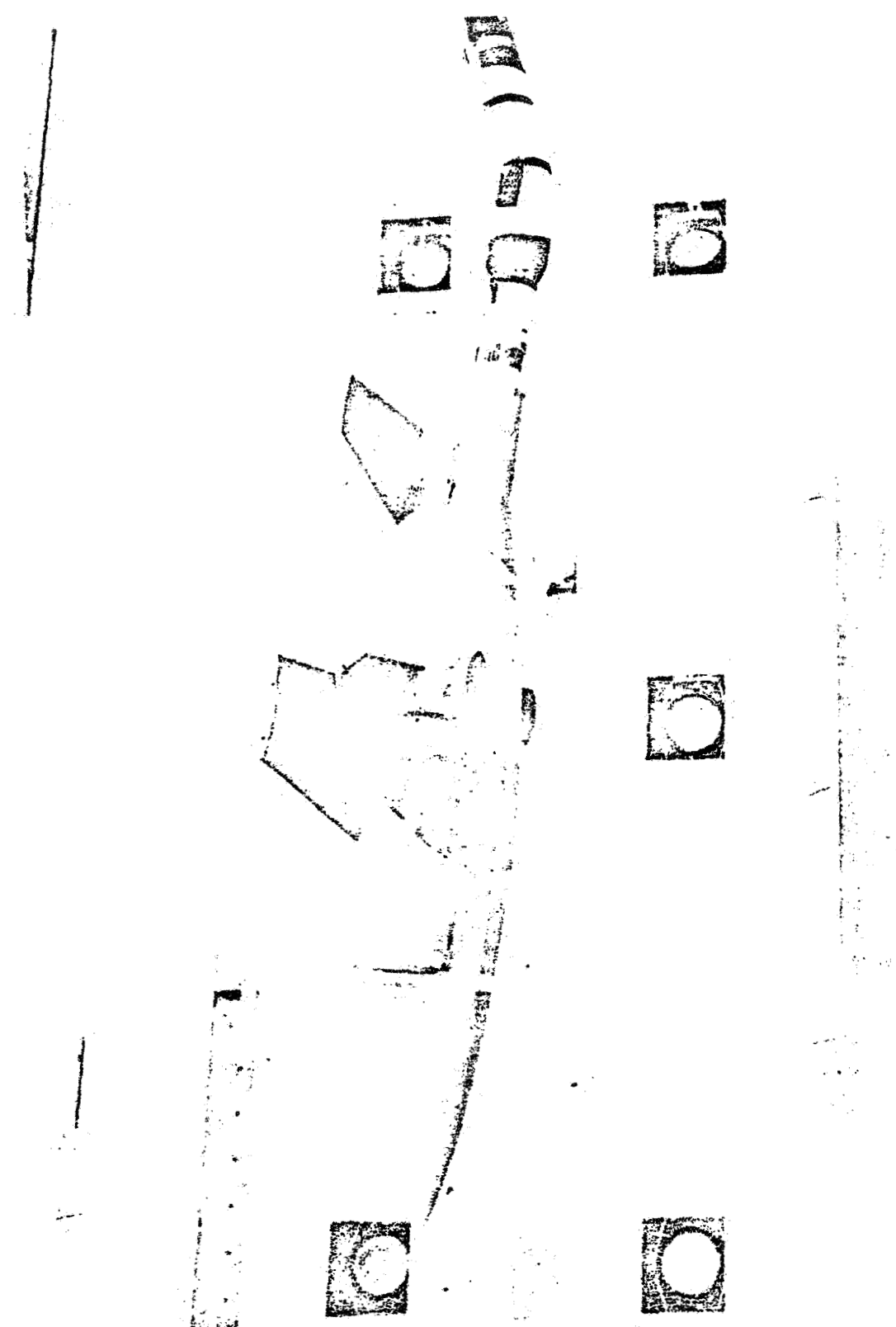
Figure 2.- Model in the V/STOL tunnel.



(b) Front vectored-thrust configuration.

Figure 2. - Continued.

L-71-3072.1



(c) Rear vectored-thrust configuration with flaps.

Figure 2.- Concluded.

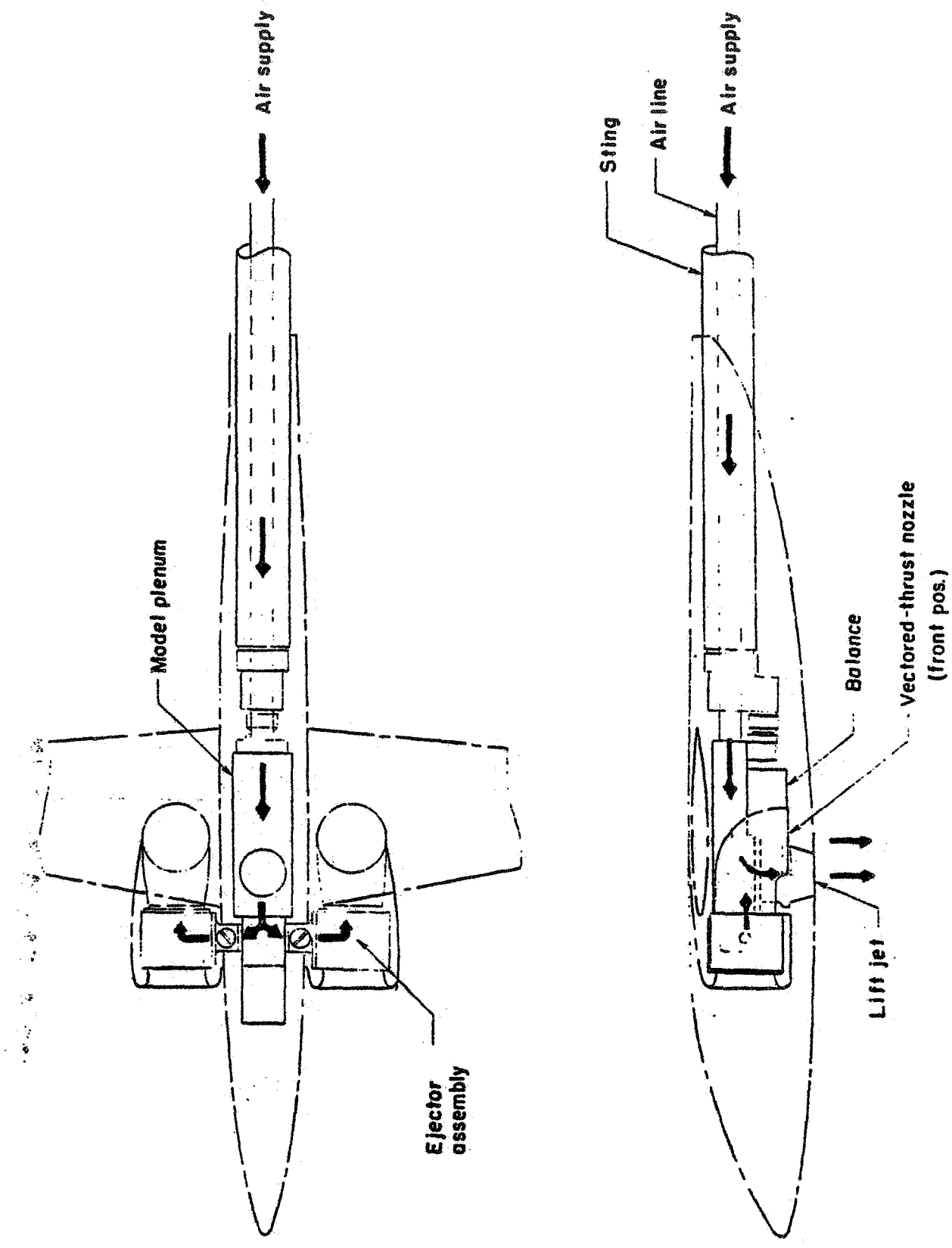


Figure 3 . - SKETCH OF THE HIGH PRESSURE AIR SYSTEM USED TO SIMULATE JET THRUST

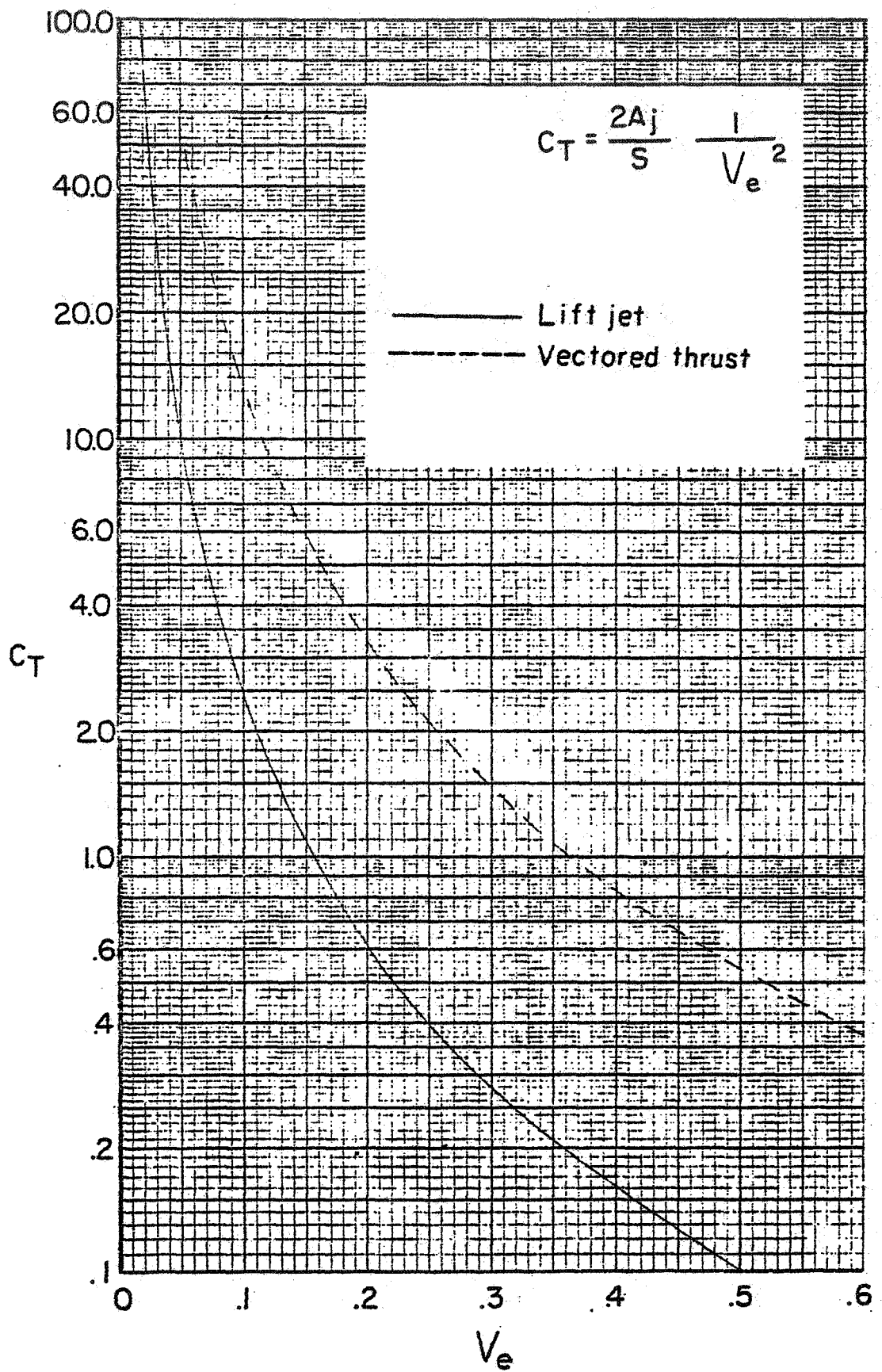


Figure 4 - Variation of thrust coefficient with effective velocity ratio

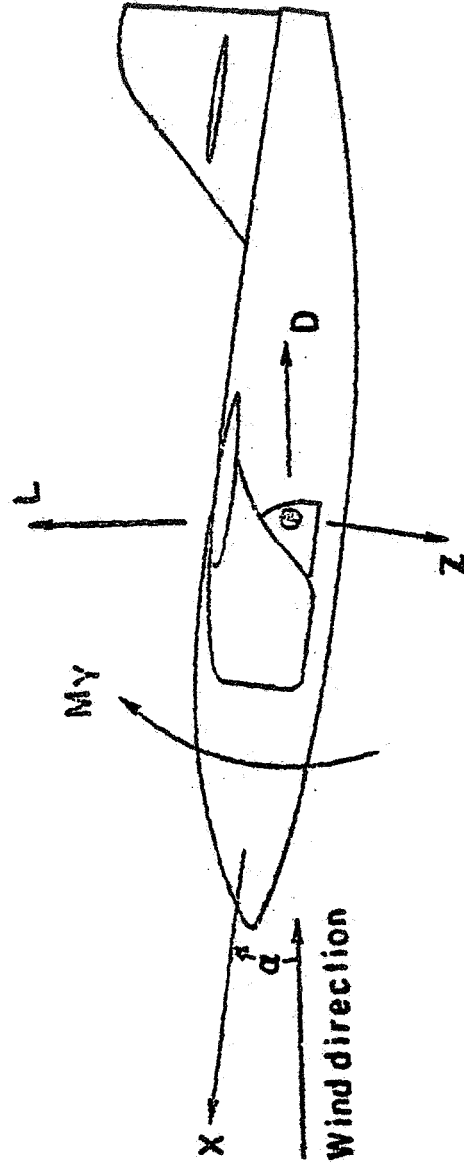


Figure 5 - Axes system.

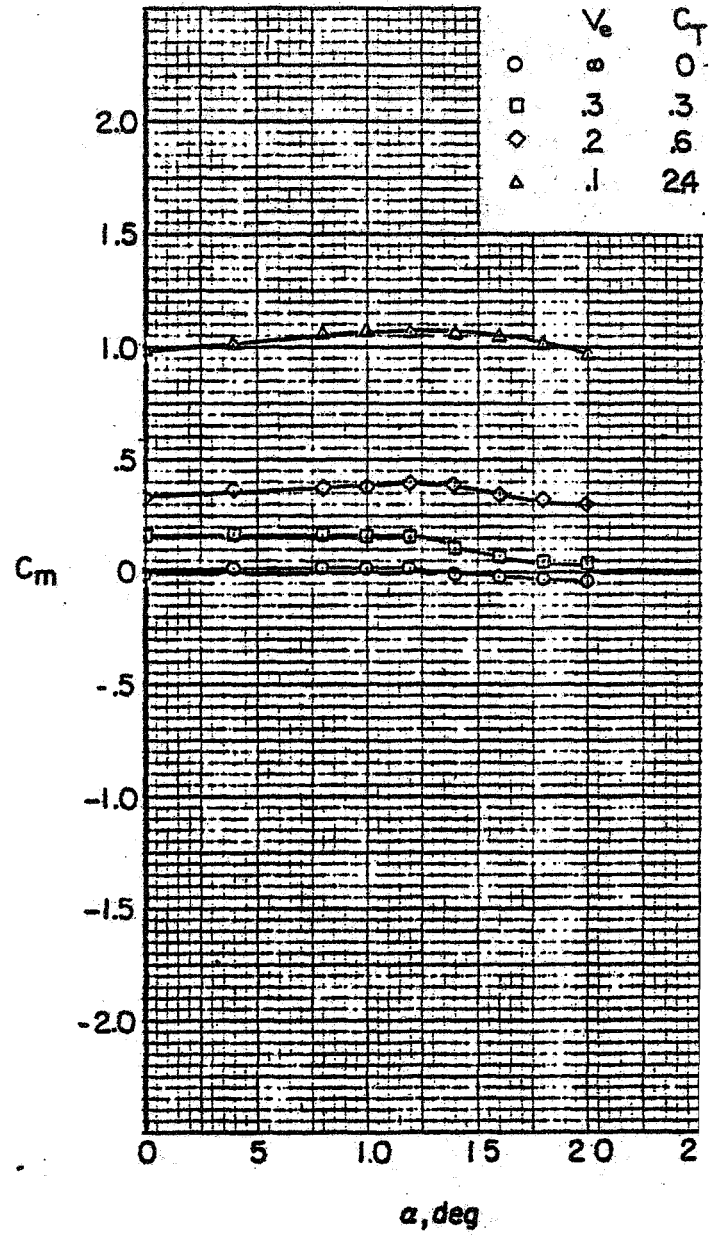
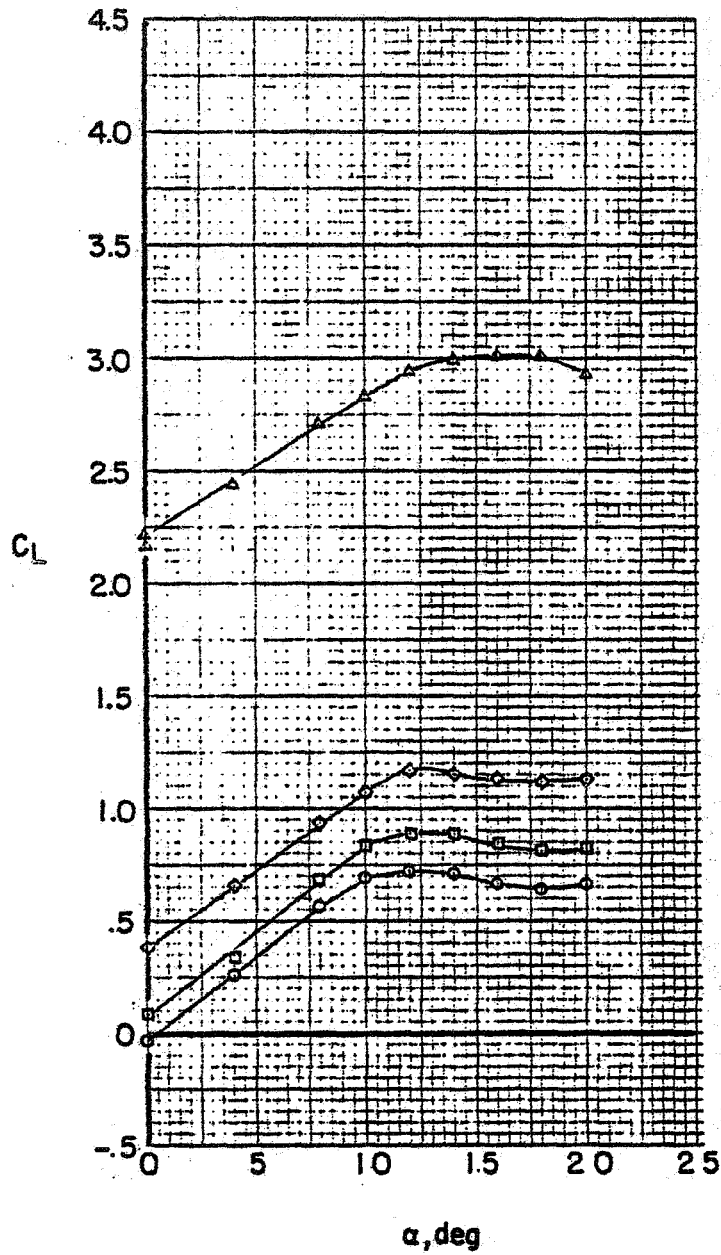


Figure 6 - Basic aerodynamic characteristics of the lift jet configuration.

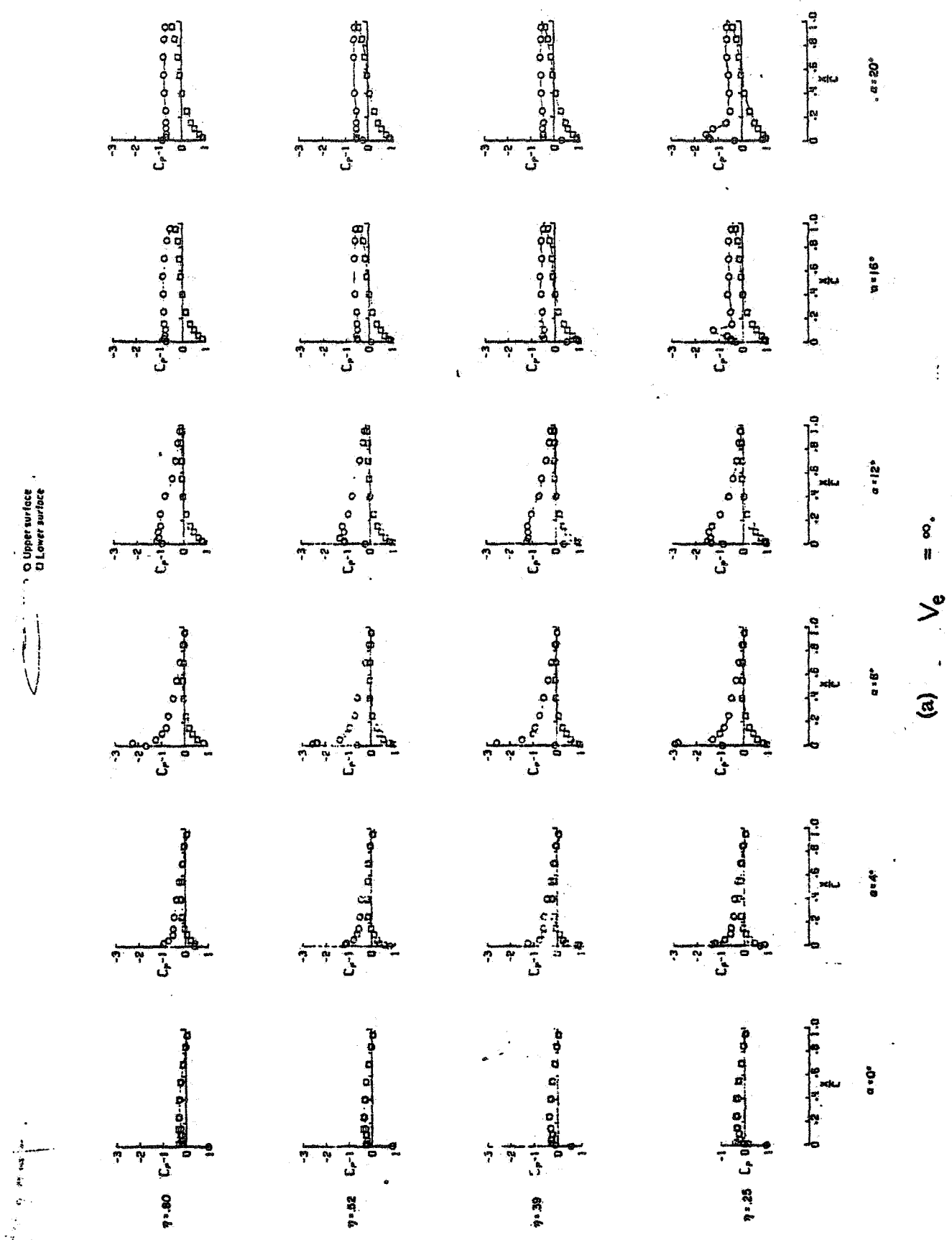
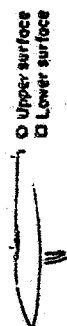
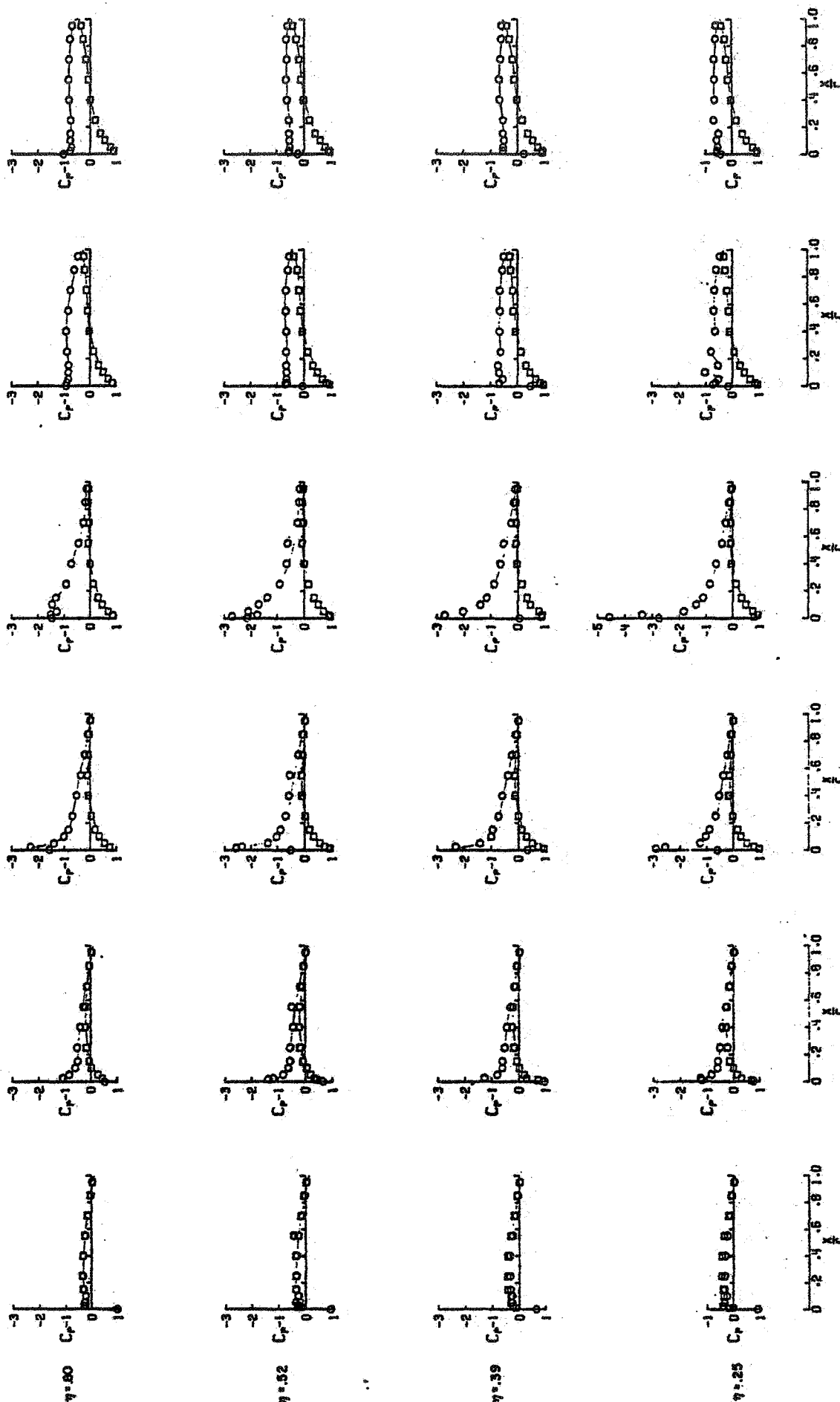


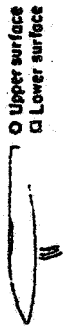
Figure 7 - Pressure distribution on the wing for the lift jet configuration.



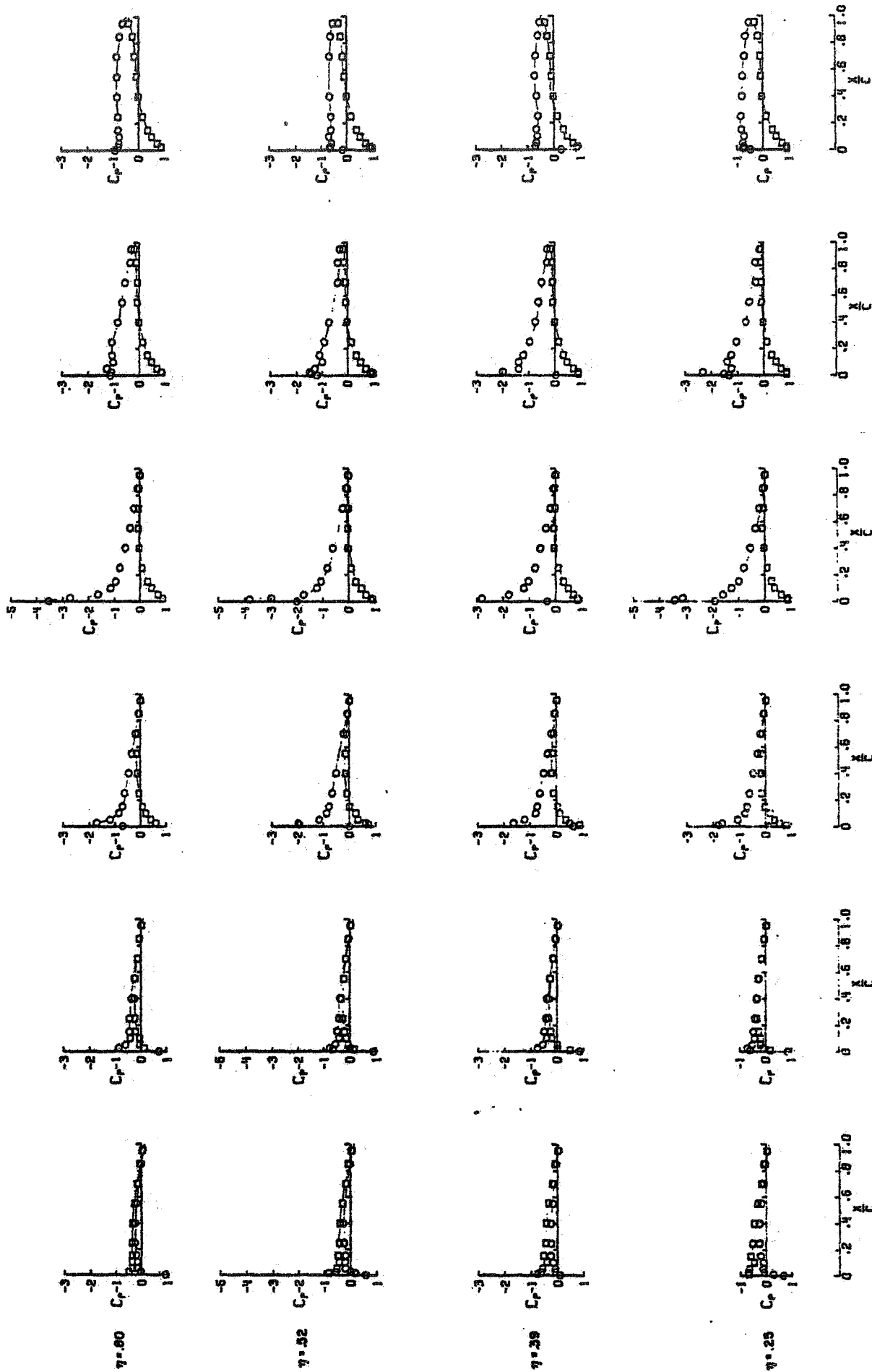
○ Upper surface
□ Lower surface



(b) $V_e \approx 0.3$.



○ Upper surface
□ Lower surface



(c) $V_e \approx 0.1$.

Figure 7.- Concluded.

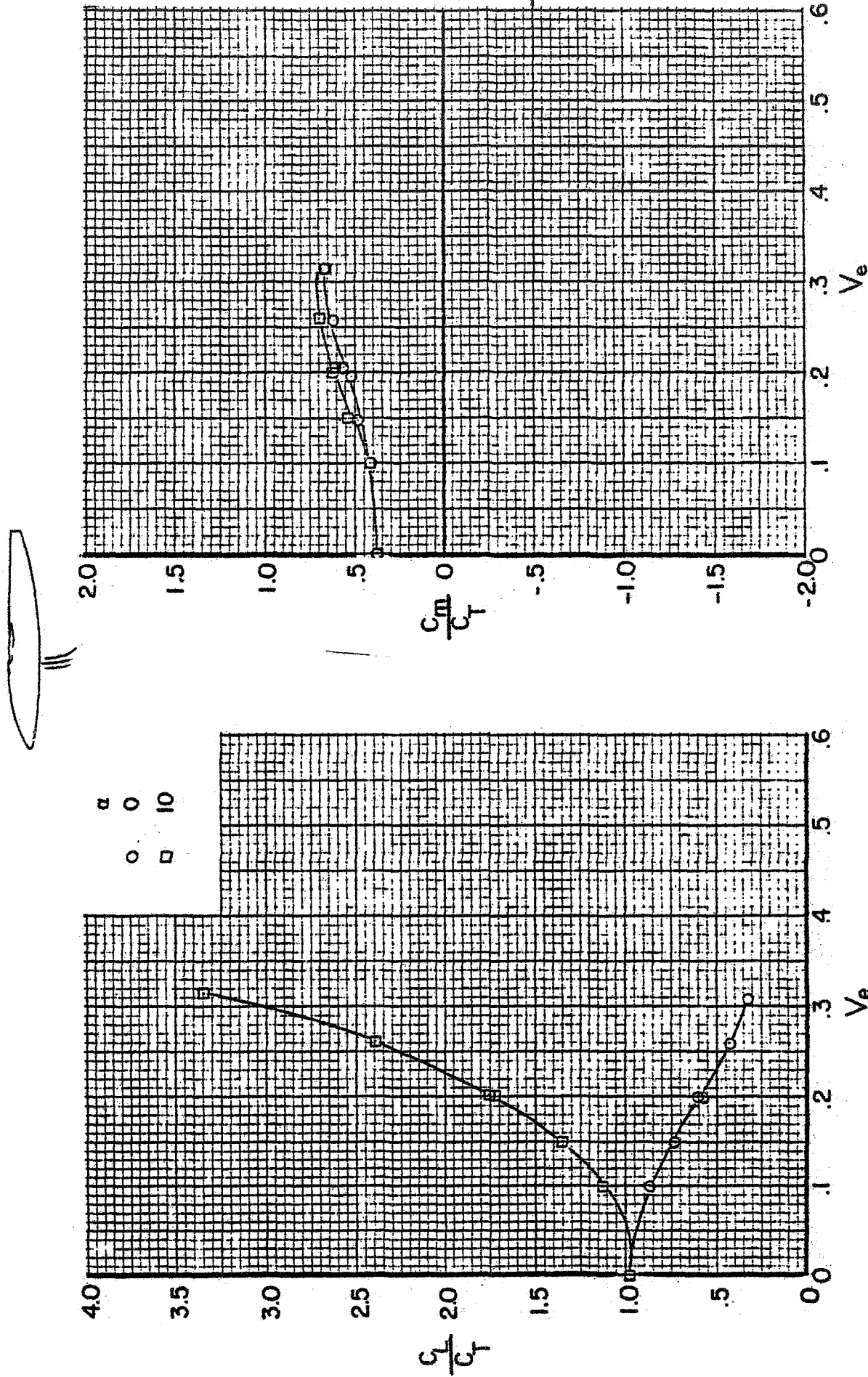


Figure 3 - Variation of the force thrust ratios with effective velocity ratio for the lift jet configuration.

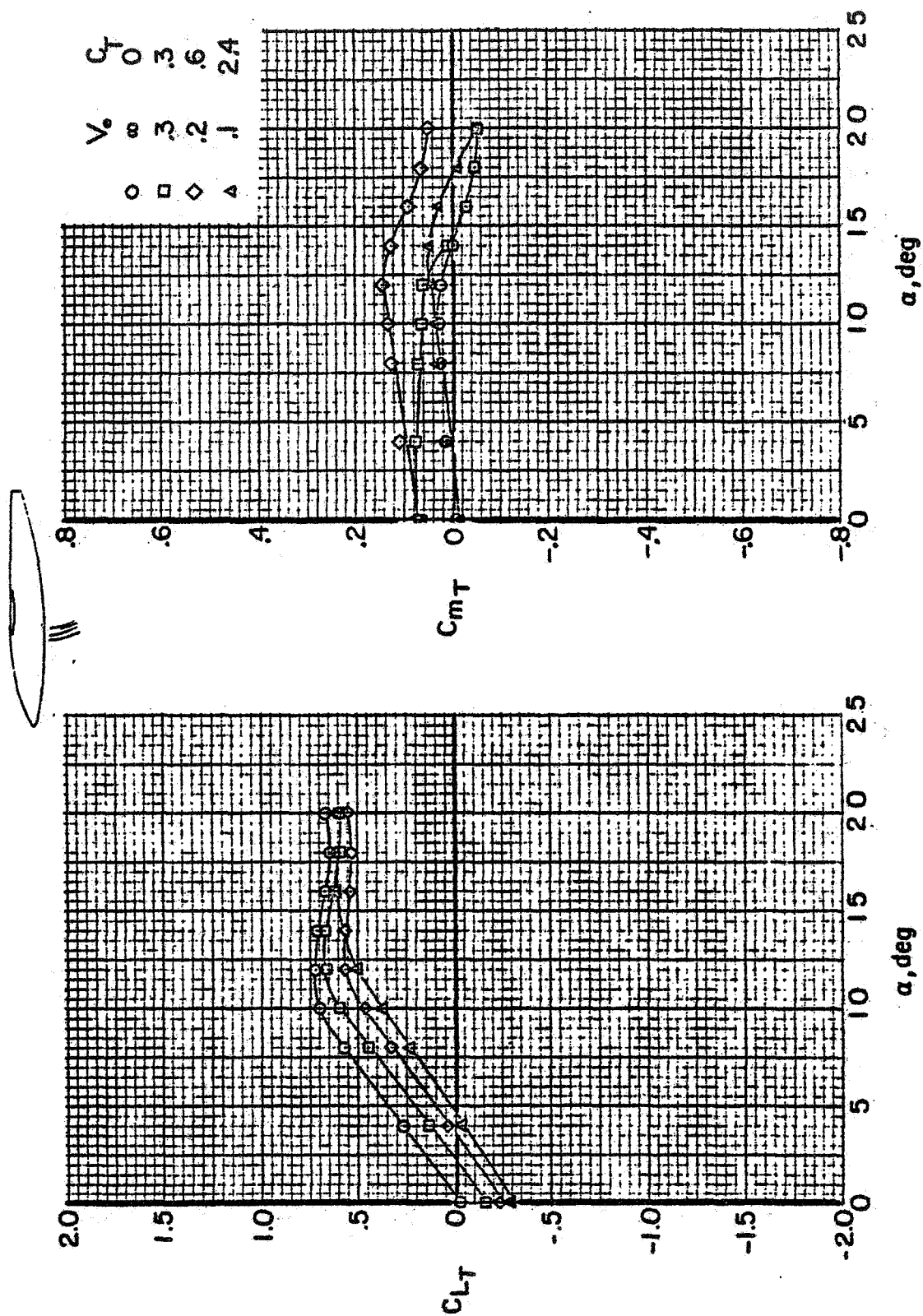
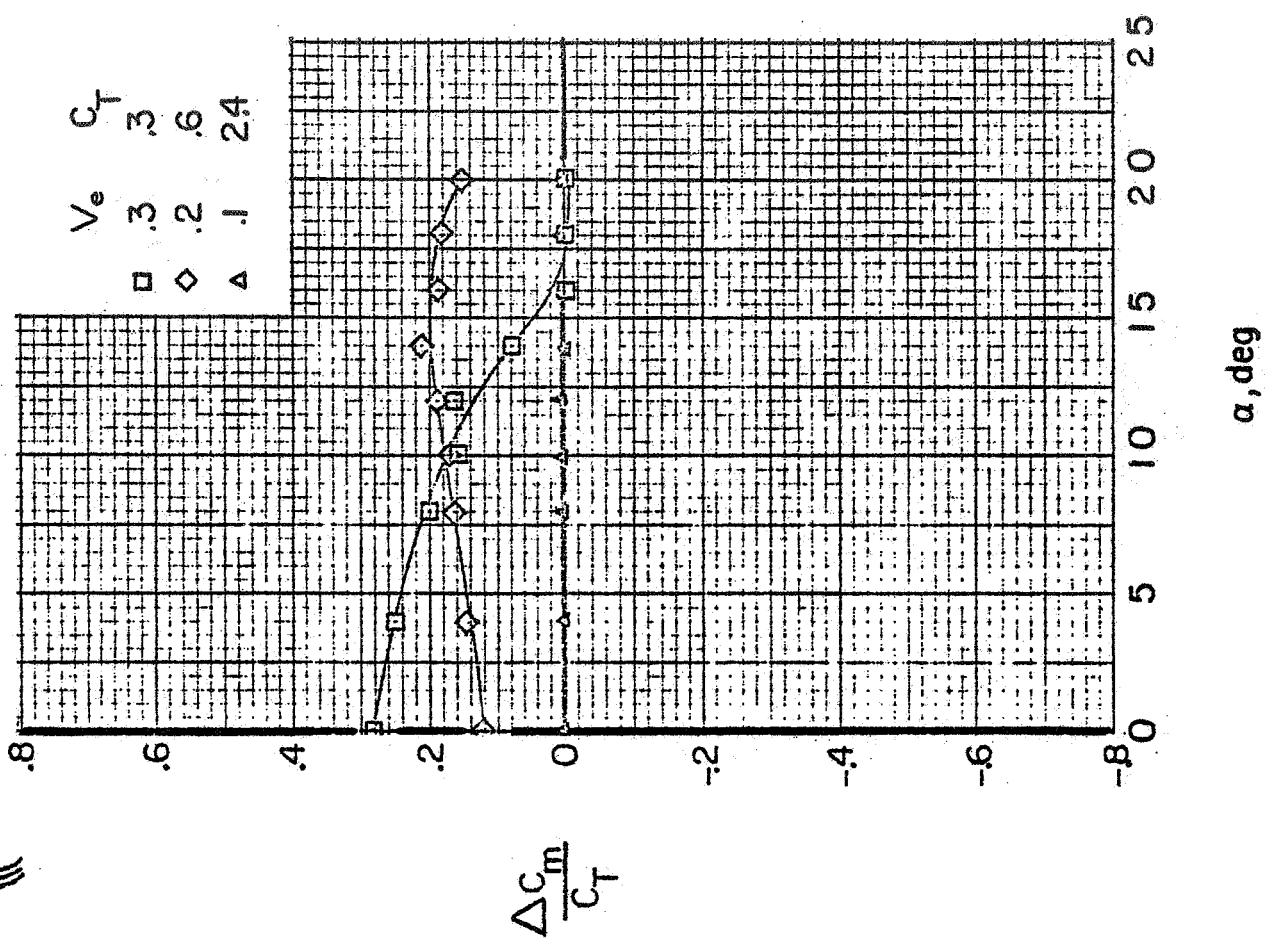
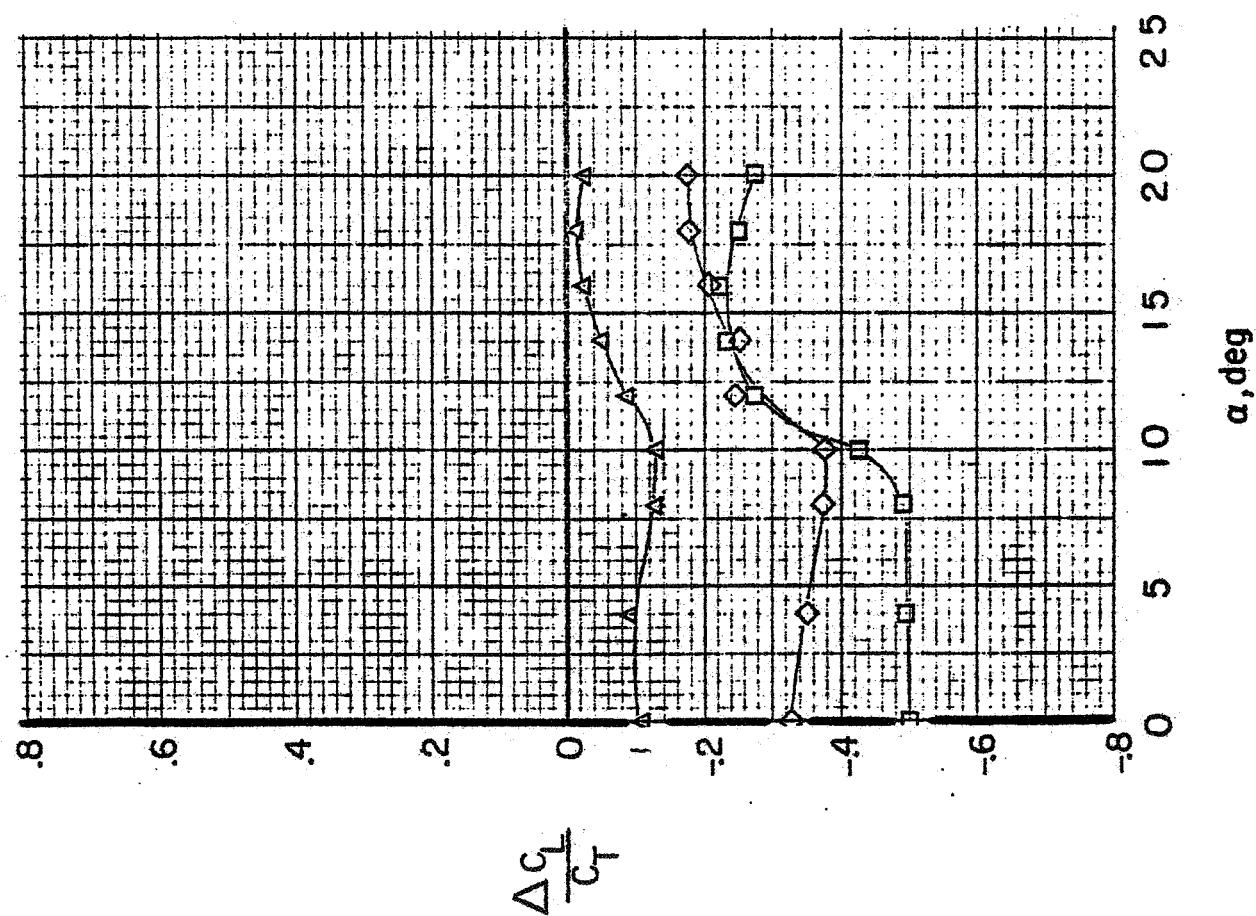


Figure 9. - Variation of the thrust removed aerodynamic characteristics with angle of attack for the lift jet configuration.



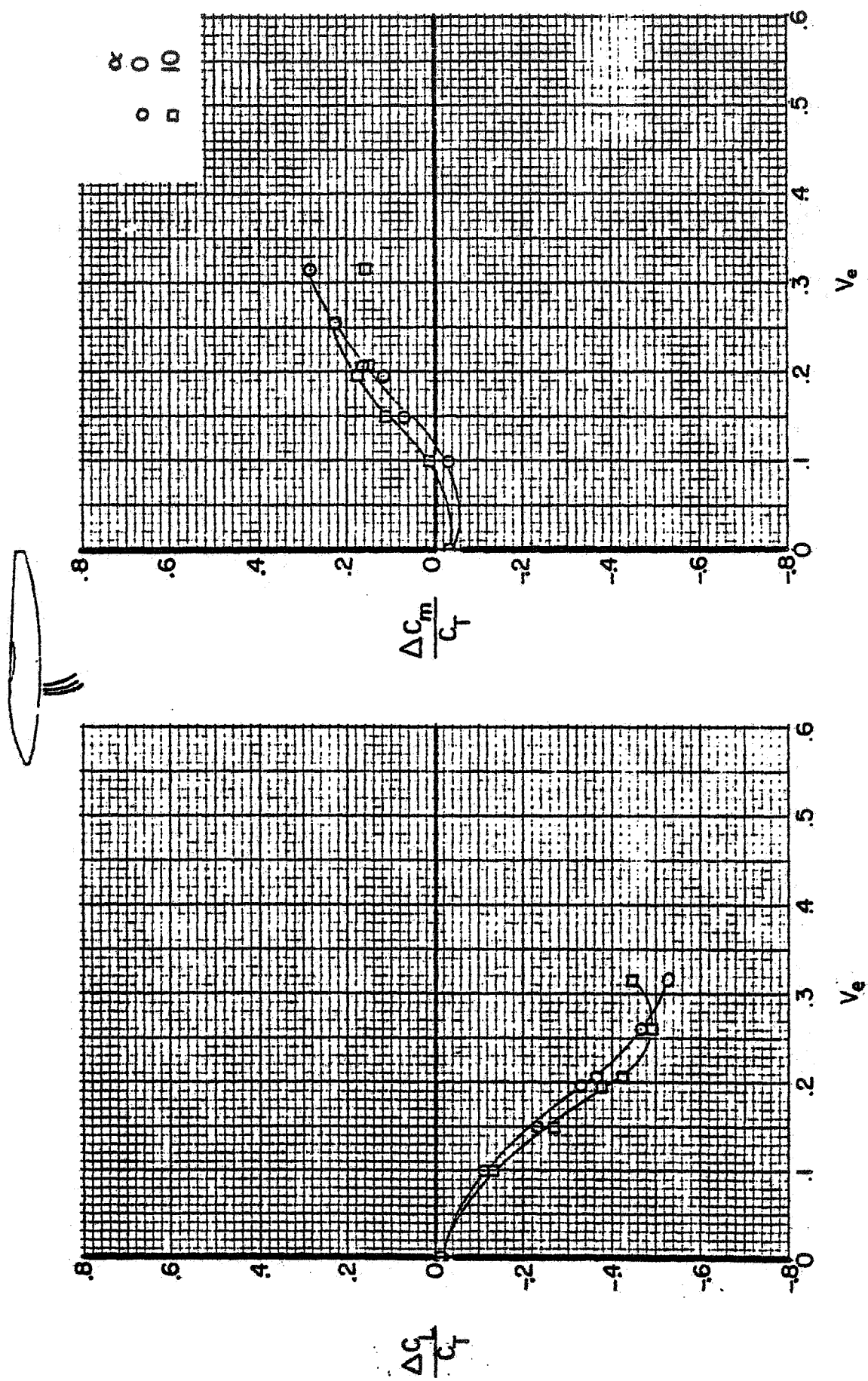


Figure II. - Variation of the Interference effects with effective velocity ratio for the lift jet configuration.

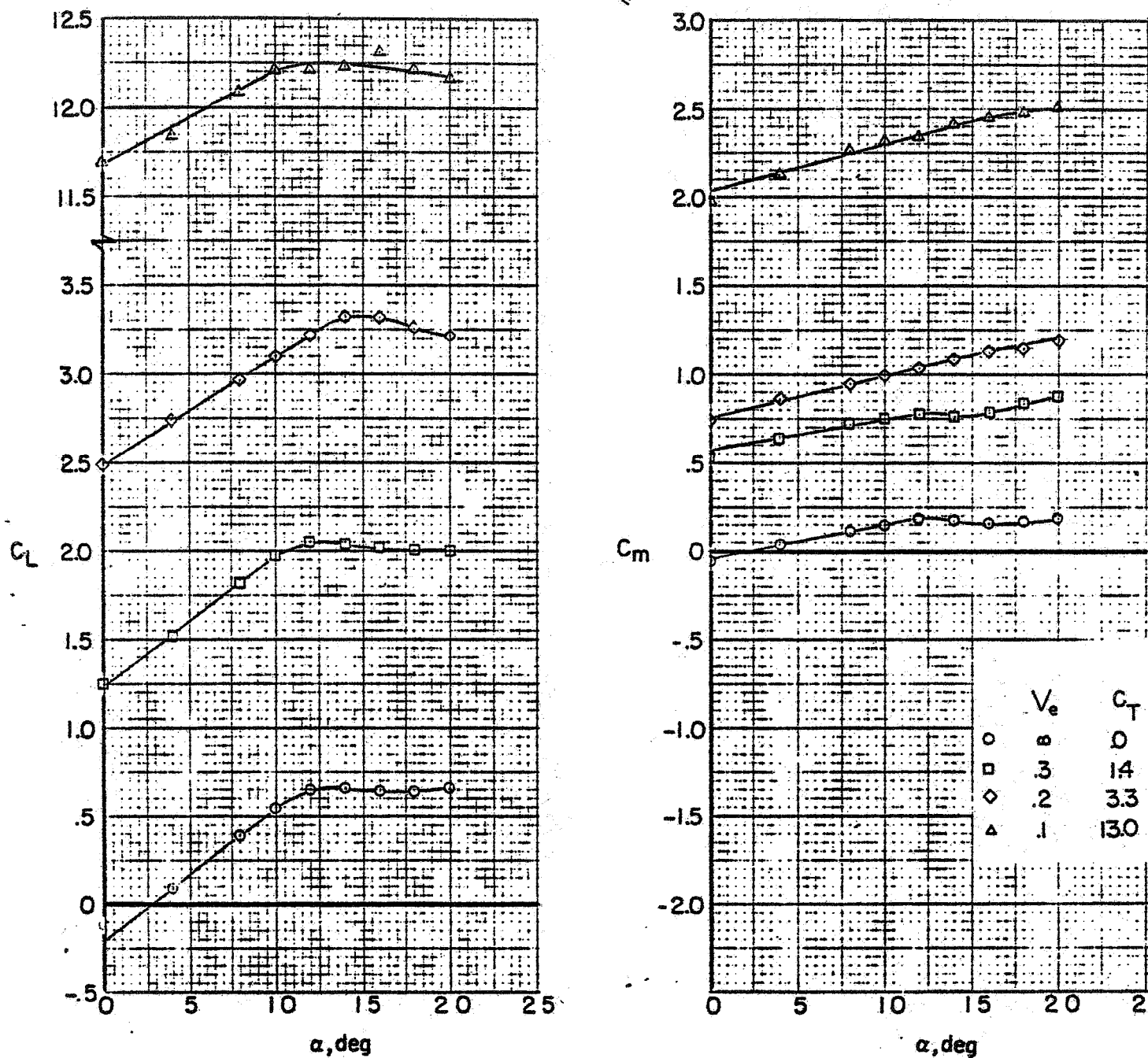
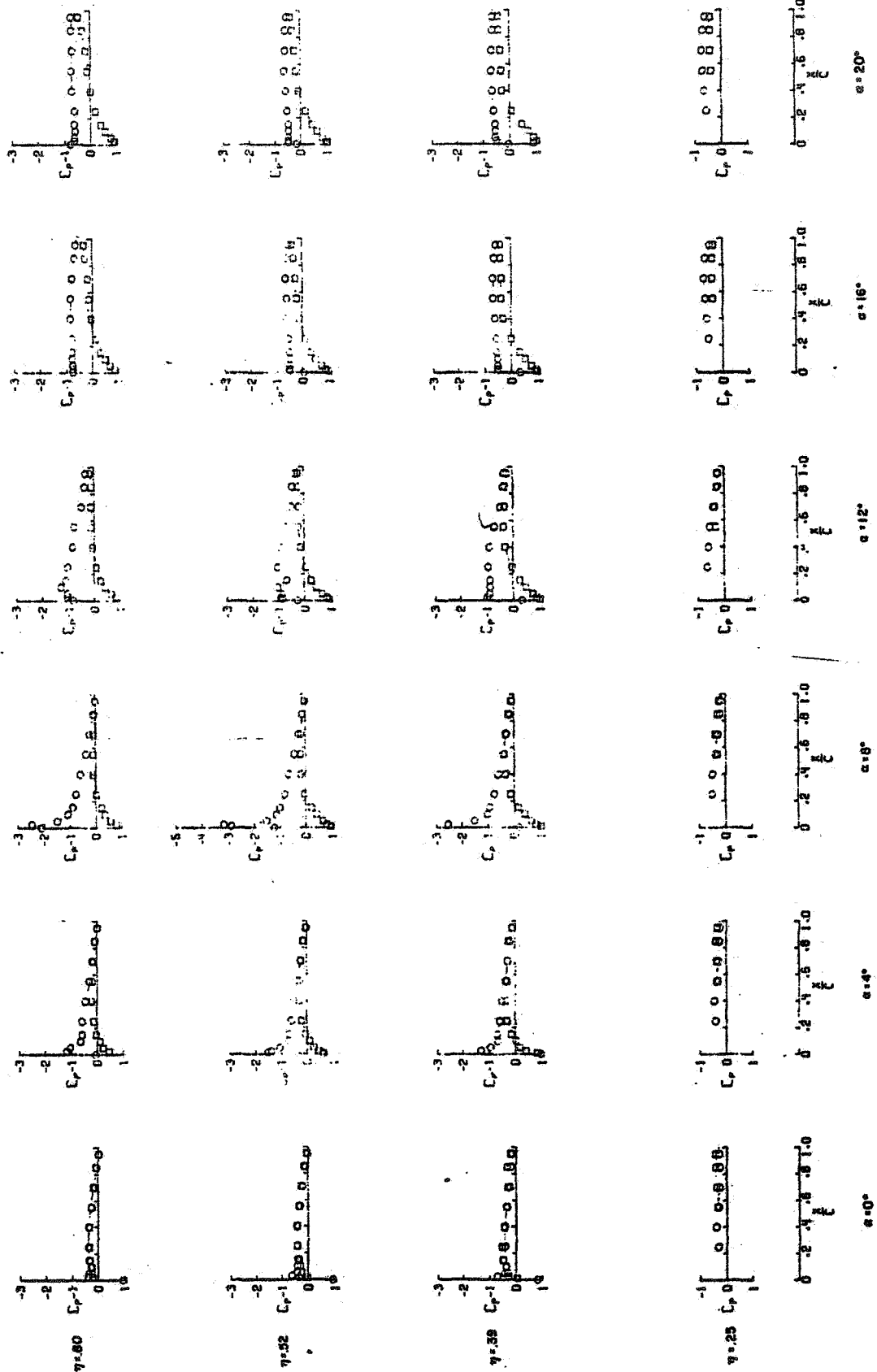
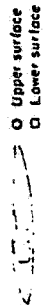


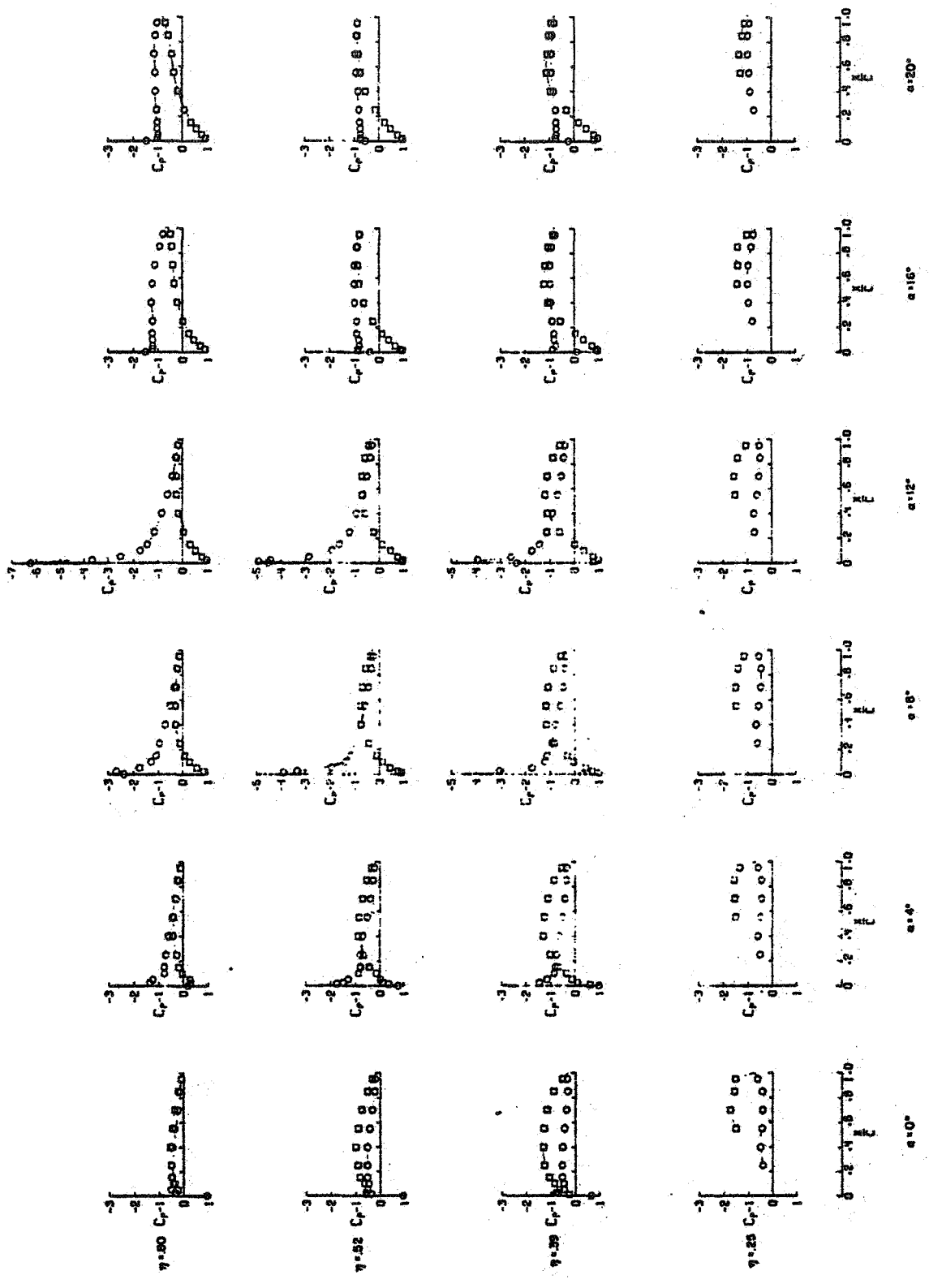
Figure 12 - Basic aerodynamic characteristics of the front vectored thrust configuration.



(a) $V_e \approx \infty$

Figure 13 - Pressure distribution on the wing for the front vectored thrust configuration.

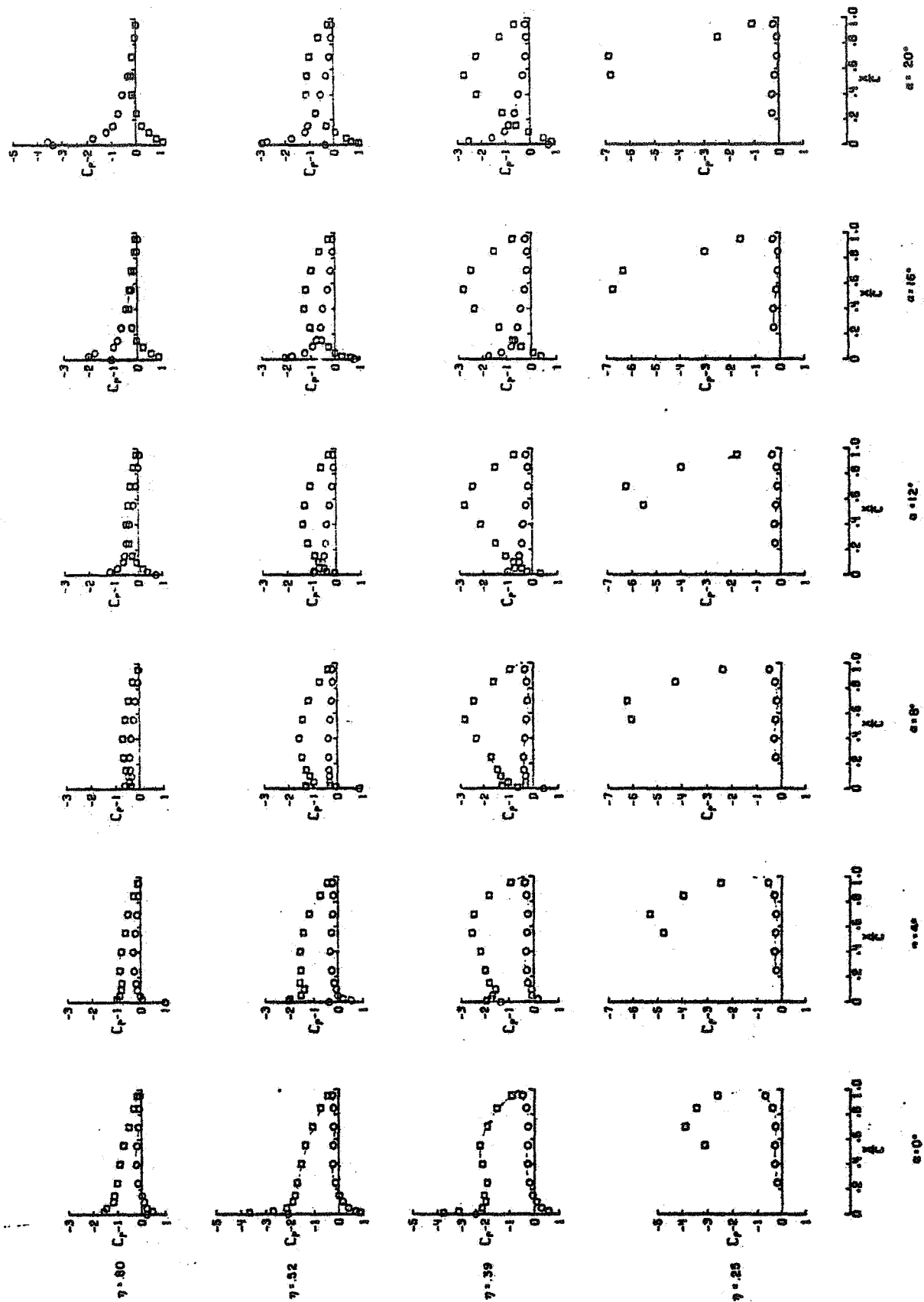
○ Upper surface
□ Lower surface



(b) $V_e \approx 0.3$.

Figure 13 - Continued

c. Upper surface
 (. Lower surface



(c) $V_e \approx 0.1$.

Figure 13.- Concluded.

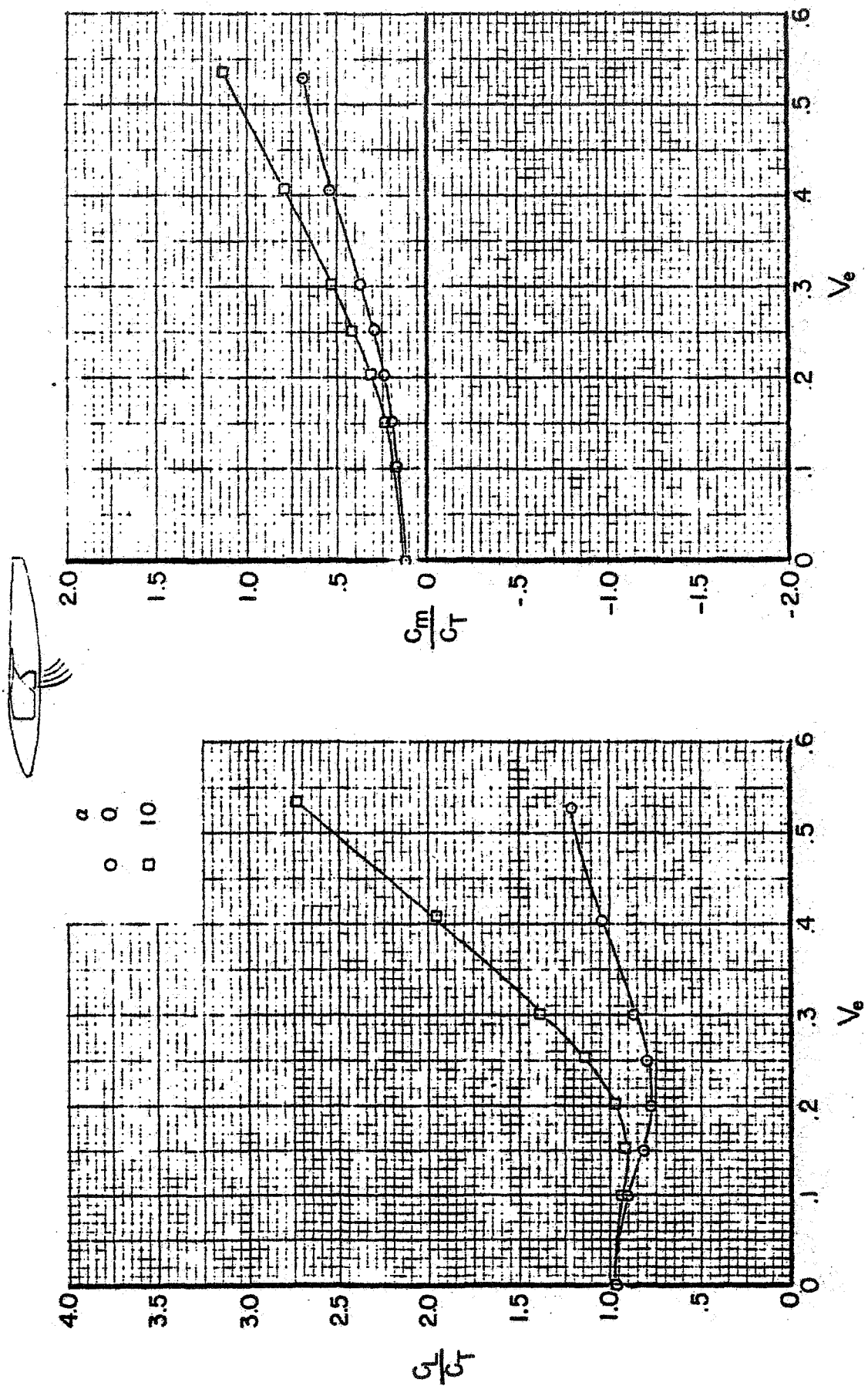


Figure 14 - Variation of the force thrust ratios with effective velocity ratio for the front vectored thrust configuration.

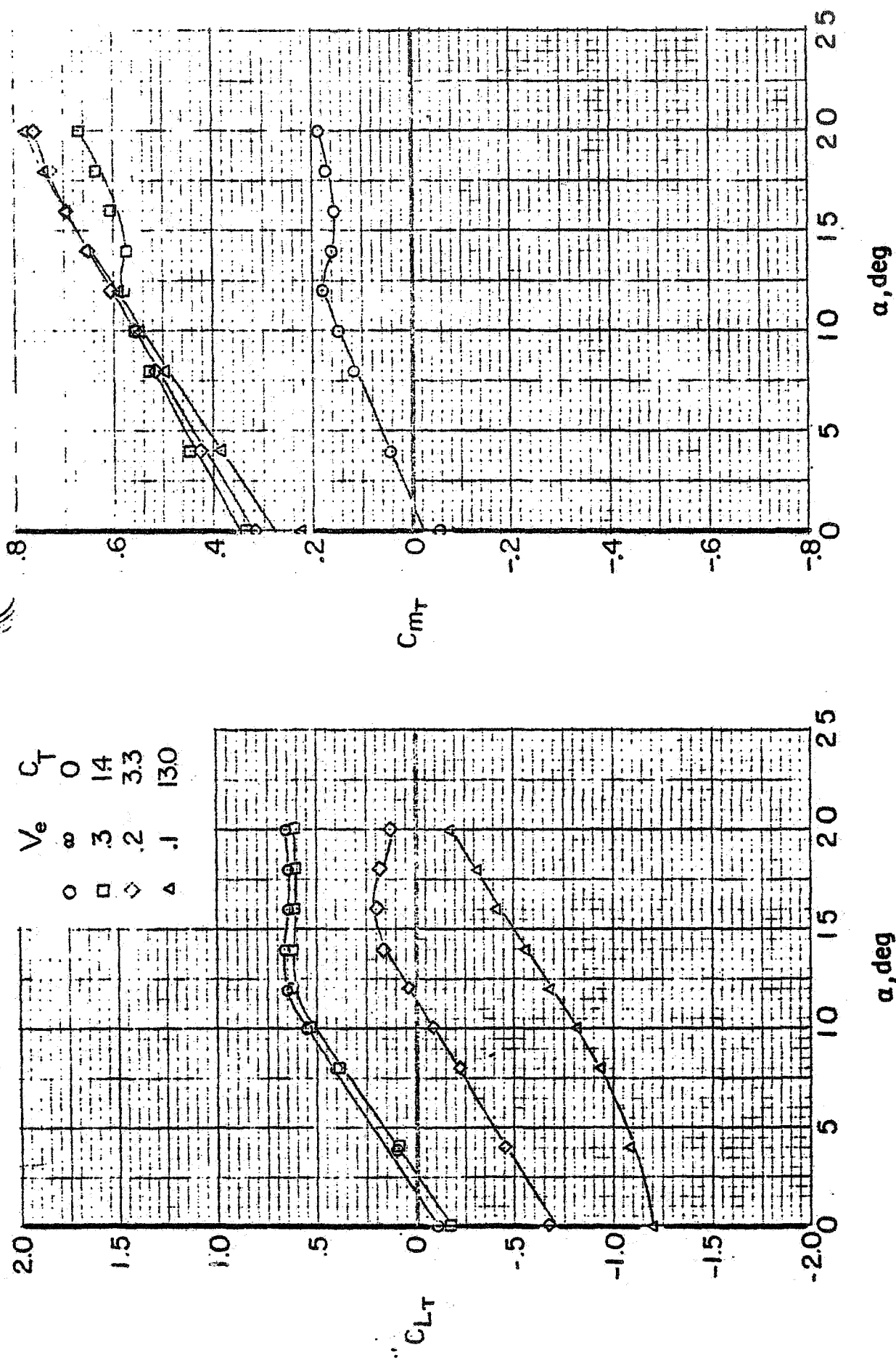


Figure 15. - Variation of the thrust removed characteristics with angle of attack for the front vectored thrust configuration.

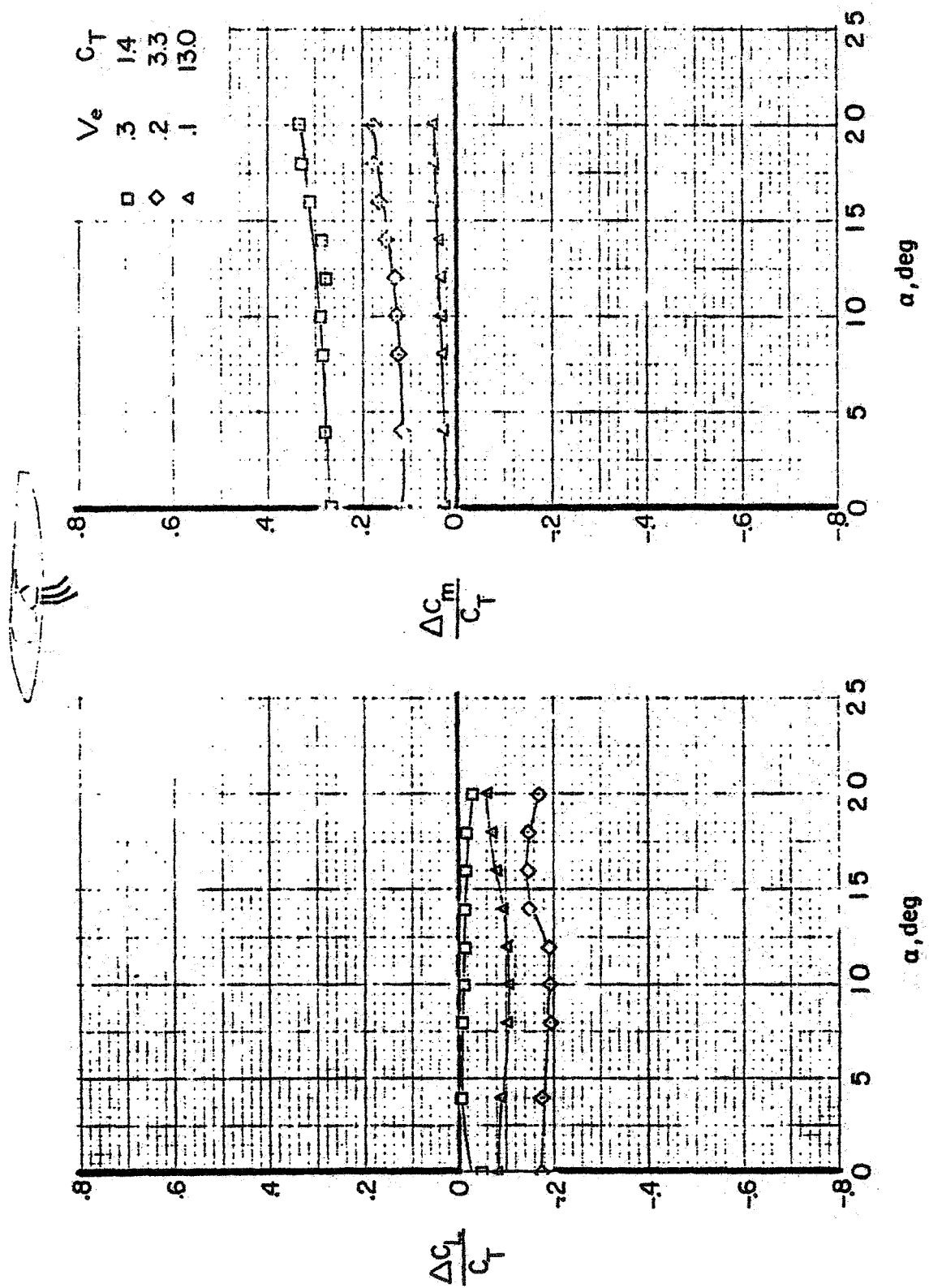


Figure 16. - Variation of the Interference effects with angle of attack for the front vectored thrust configuration.

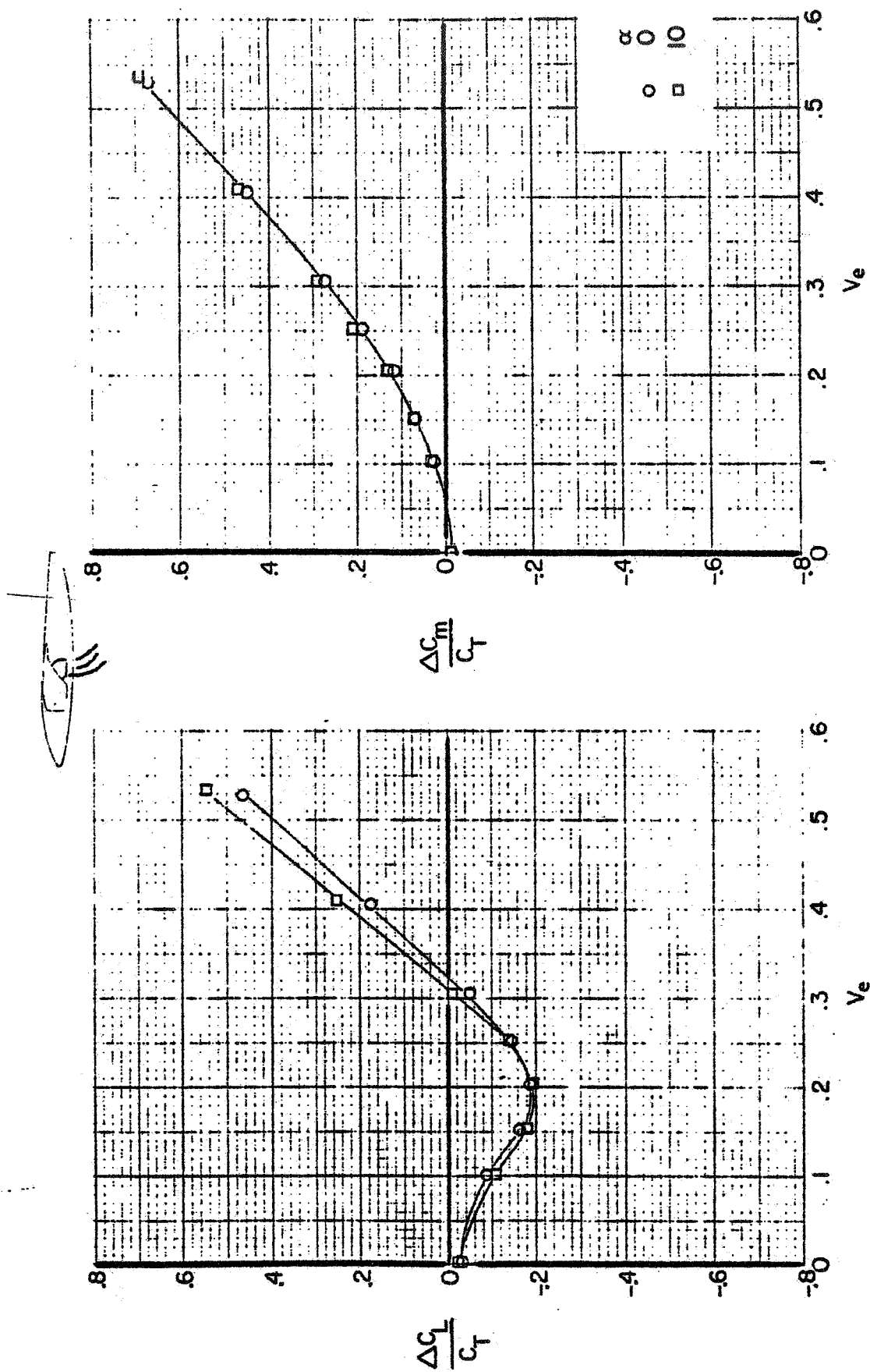


Figure 17. - Variation of the interference effects with effective velocity ratio for the front vectored thrust configuration.

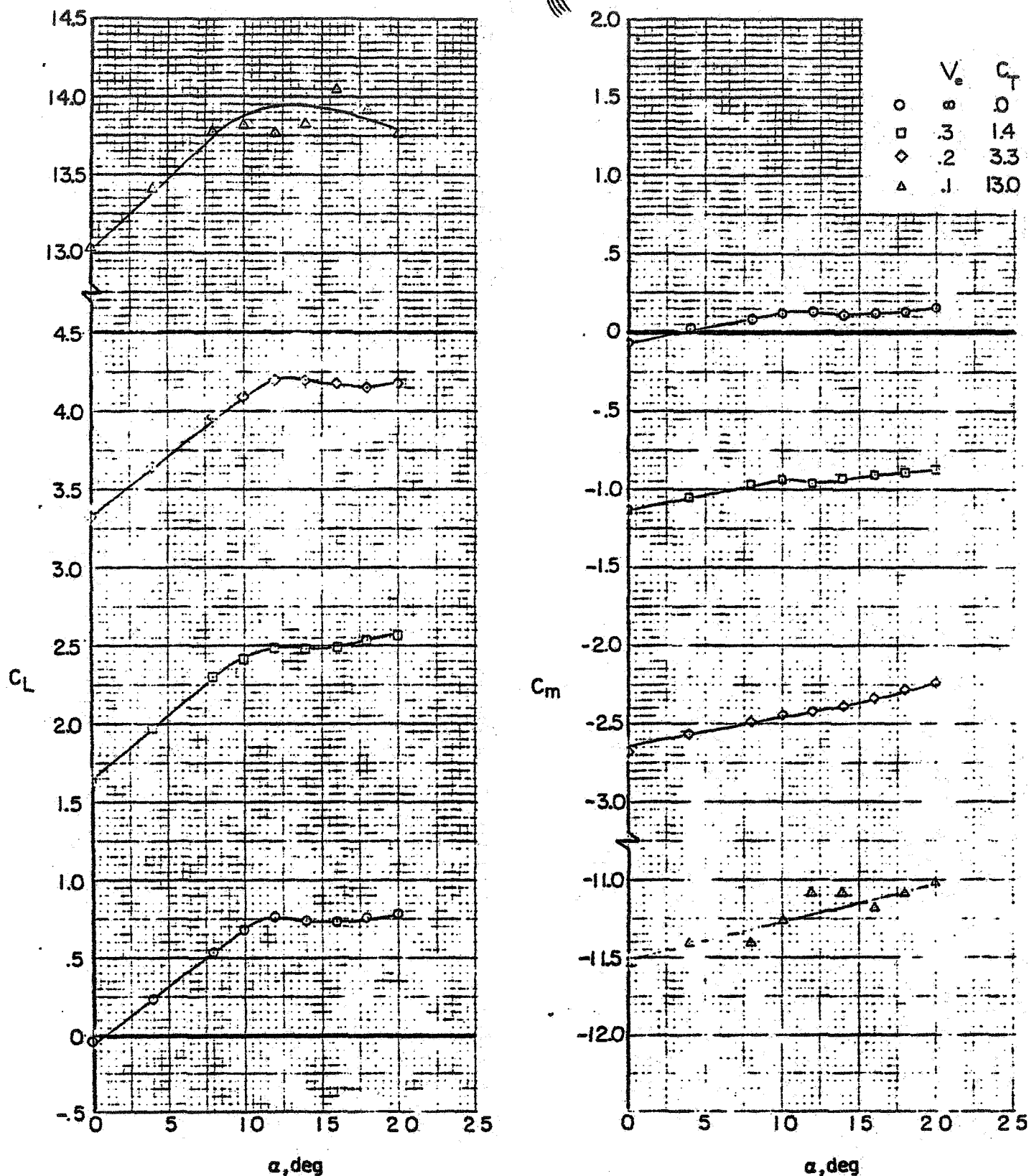
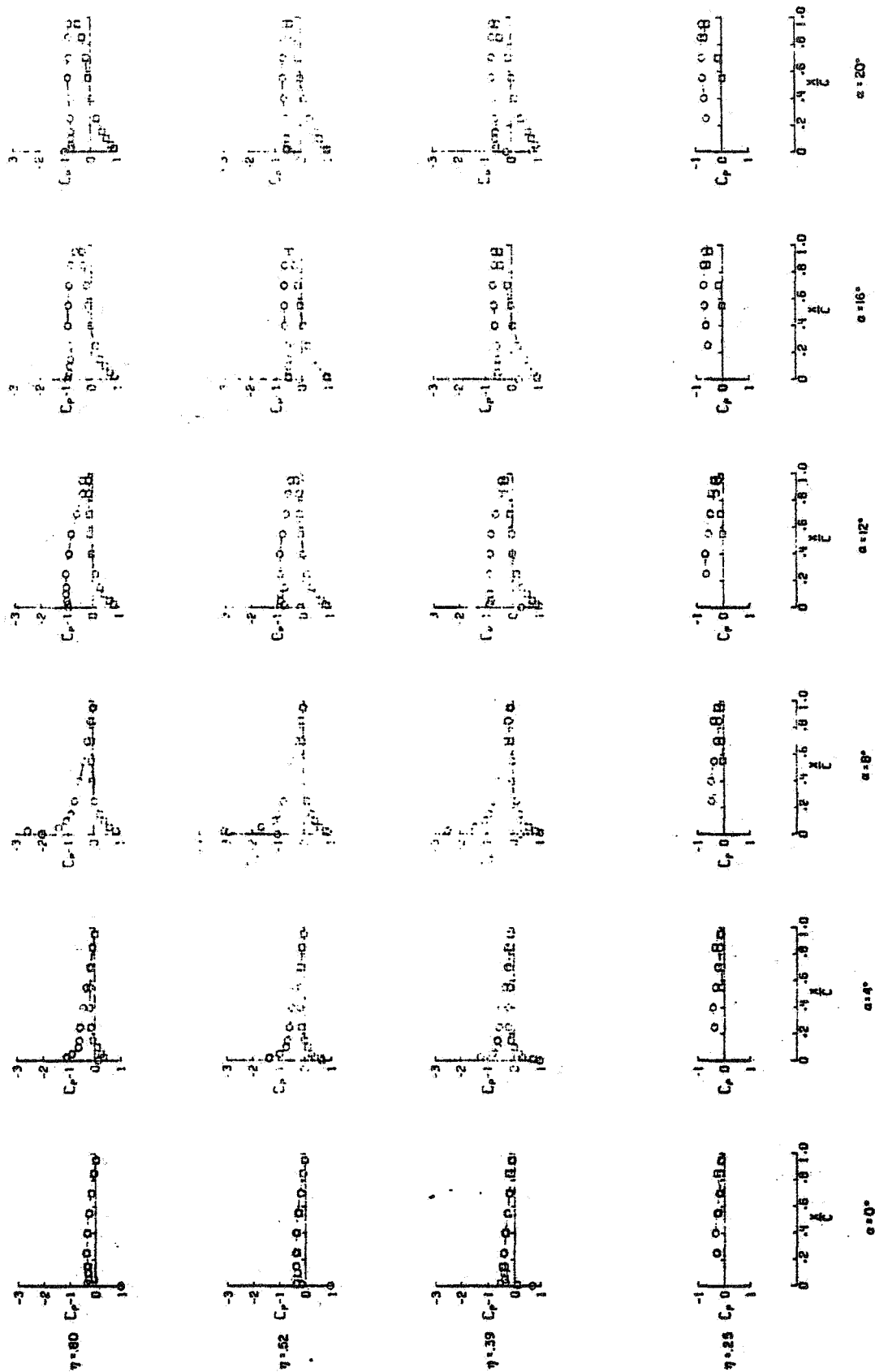


Figure 18 - Basic aerodynamic characteristics of the rear vectored thrust configuration.

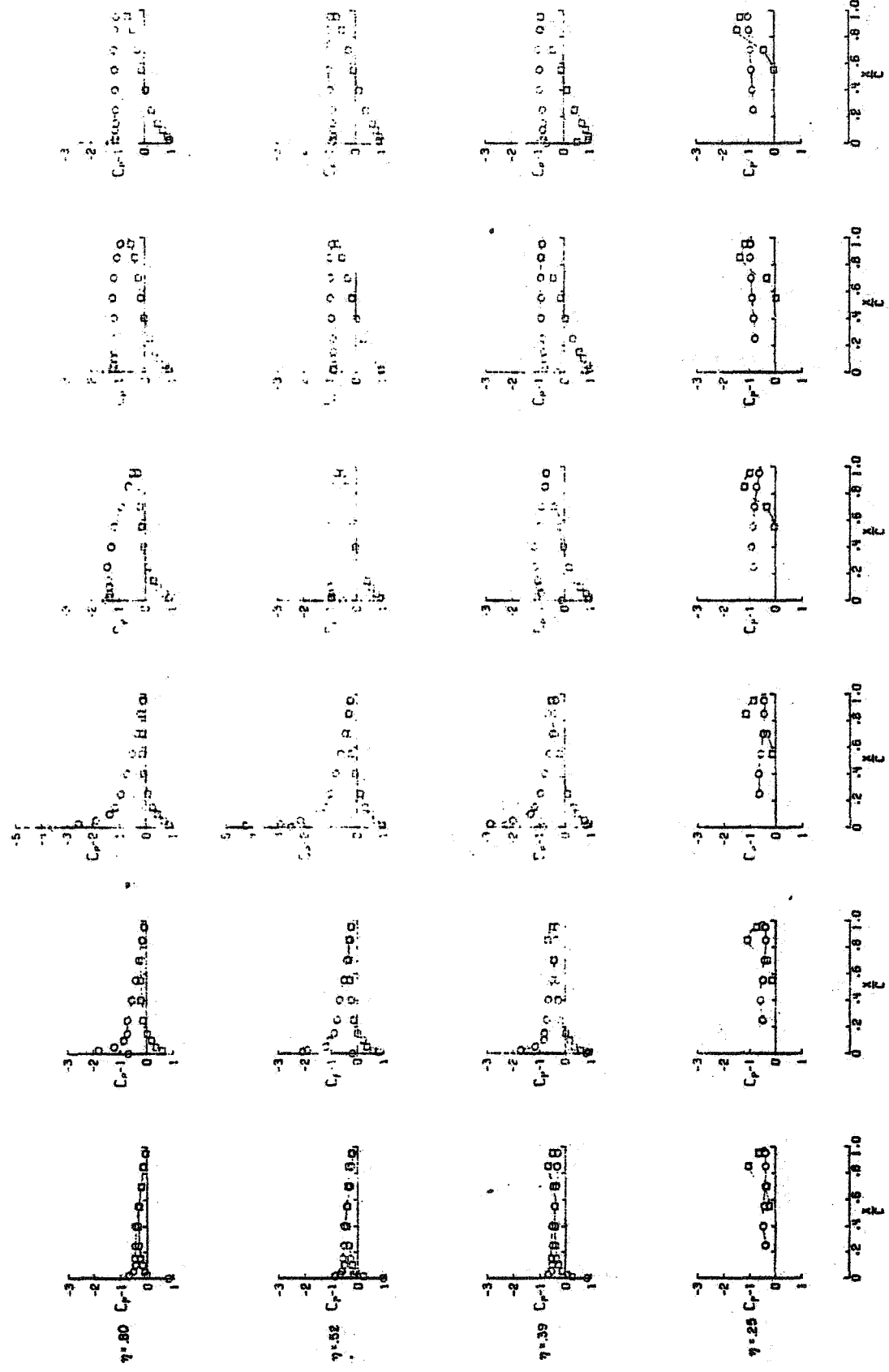
○ Upper surface
□ Lower surface



(a) $V_{\infty} \approx \infty$

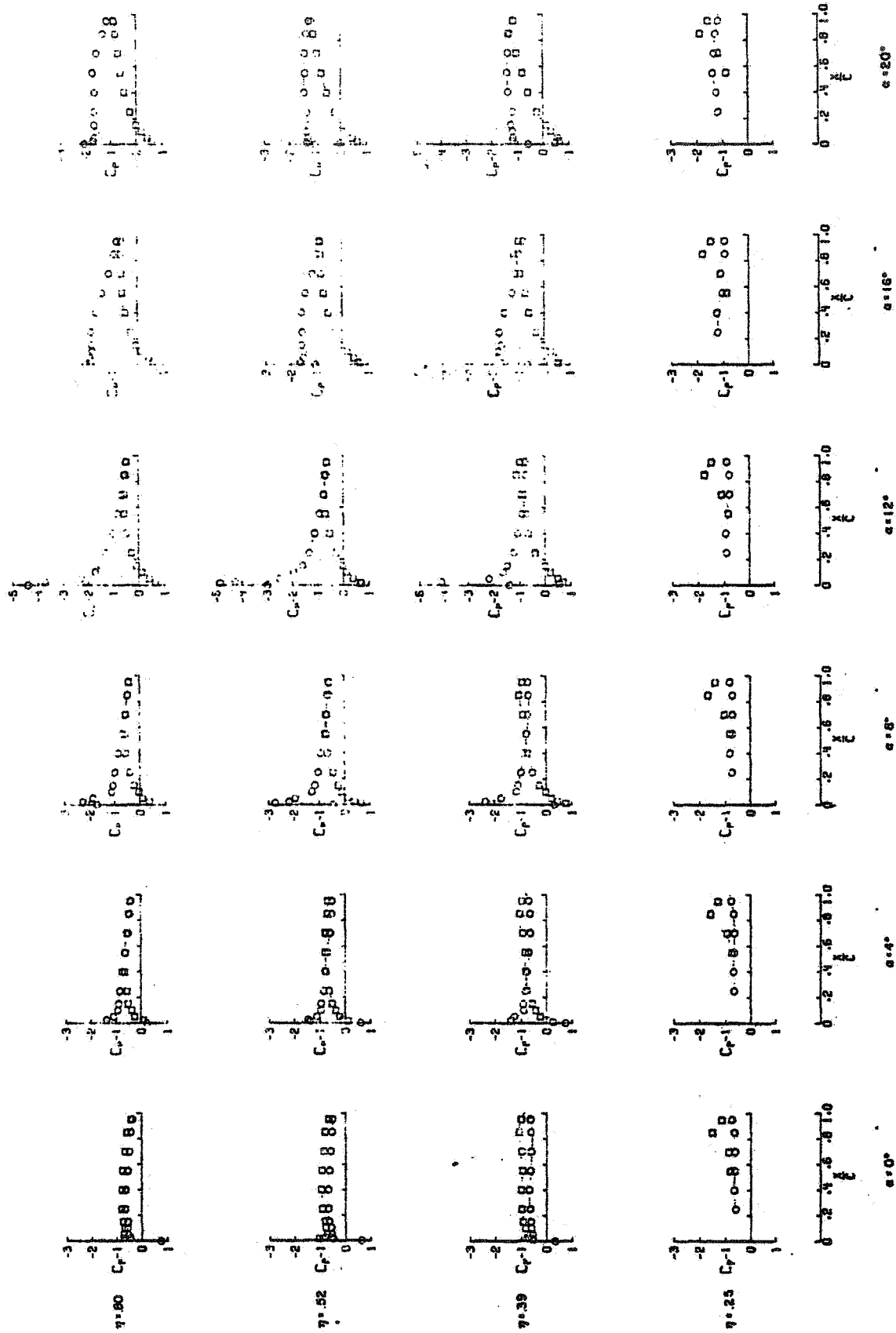
Figure 19 - Pressure distribution on the wing for the rear vectored thrust configuration.

○ Upper surface
□ Lower surface



(b) $V_e \approx 0.3$.

○ Upper surface
□ Lower surface



(c) $V_e \approx 0.1$.

Figure 19.- Concluded.

25

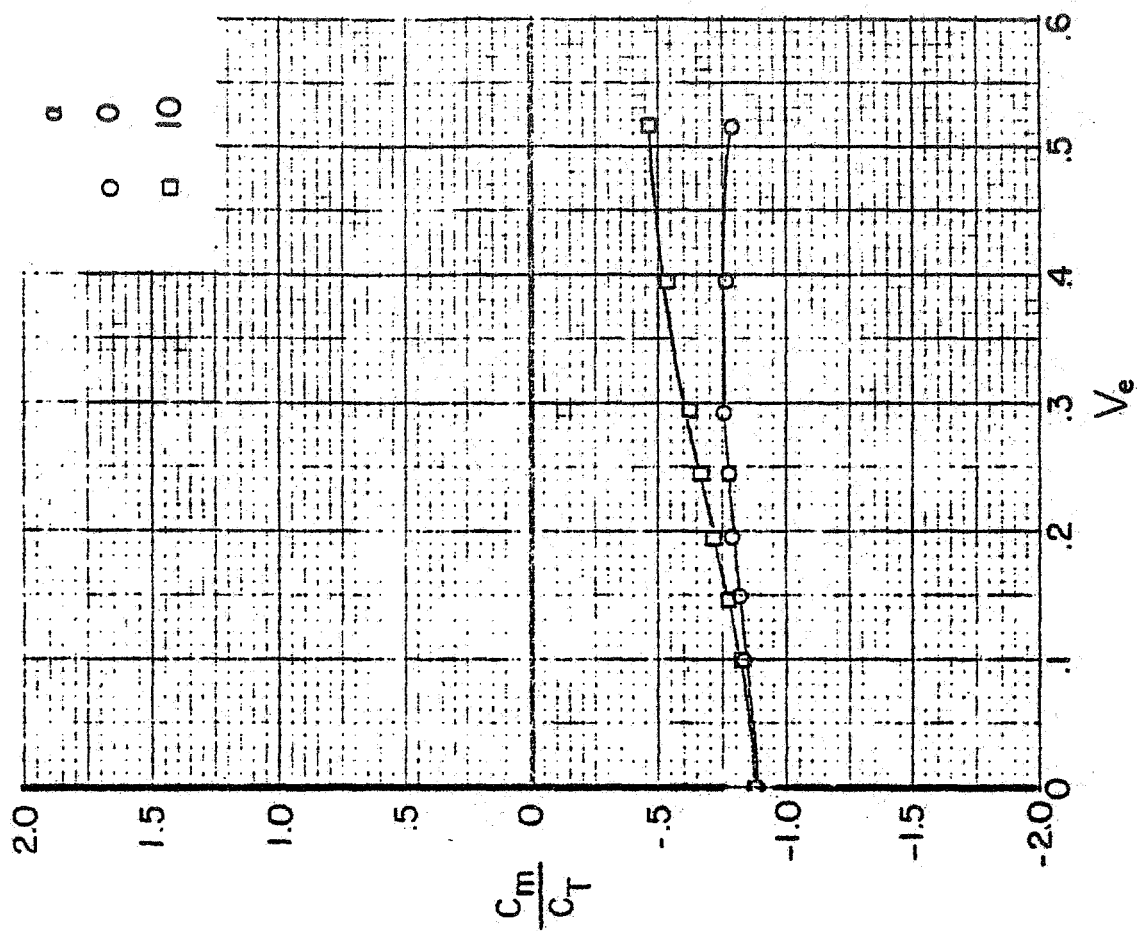
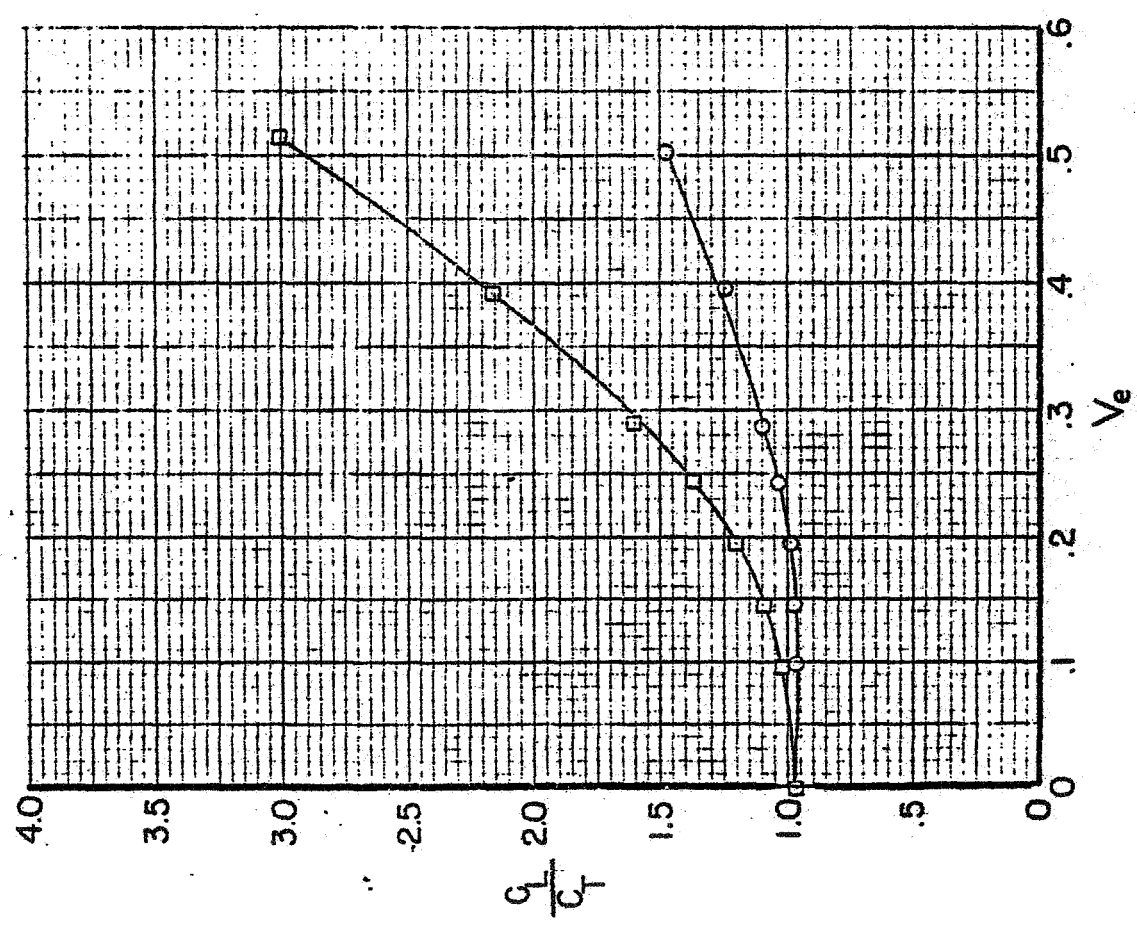


Figure 20 - Variation of the force thrust ratios with effective velocity ratio for the read vectored

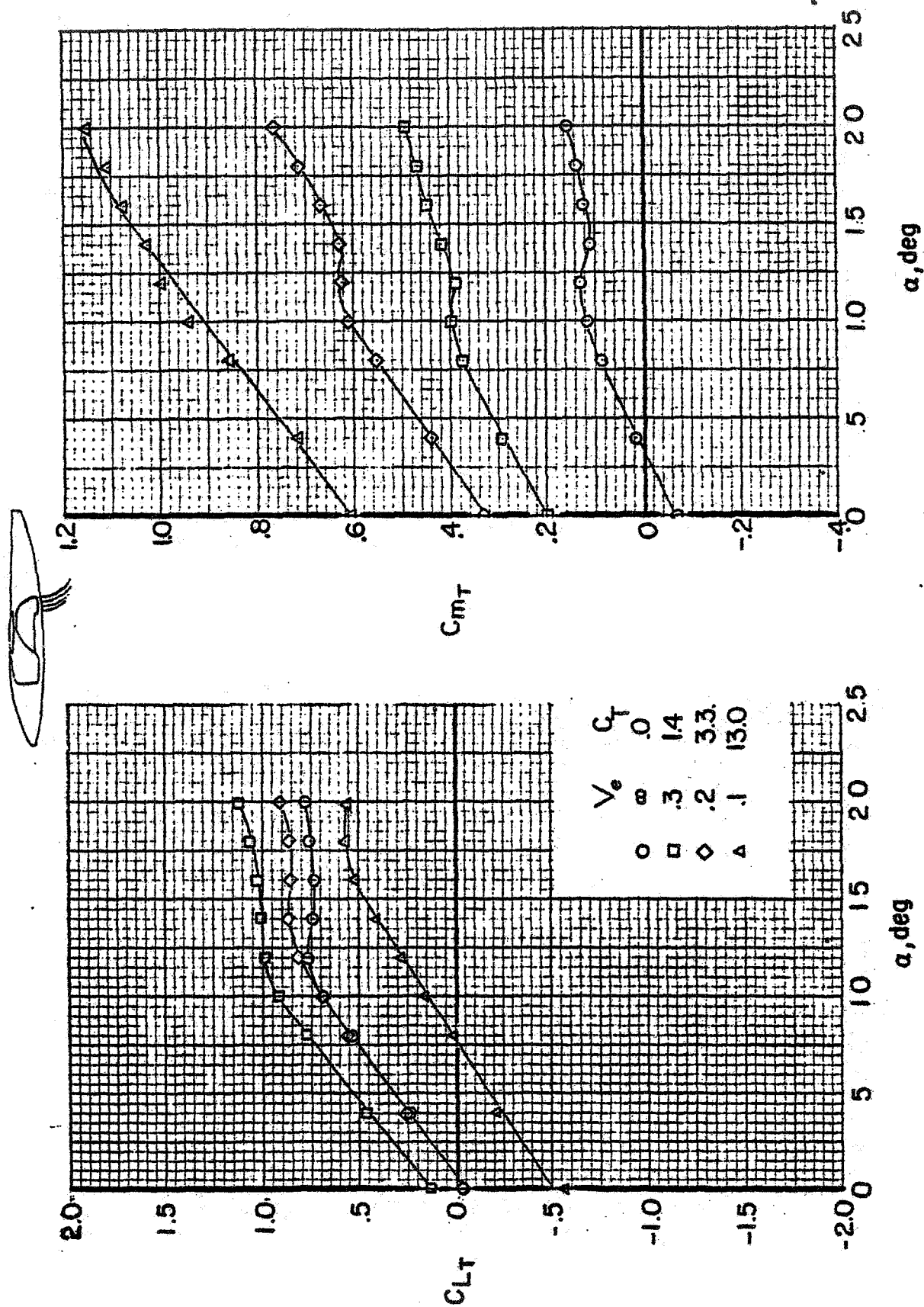


Figure 21. - Variation of the thrust removed characteristics with angle of attack for the rear vectored thrust configuration.

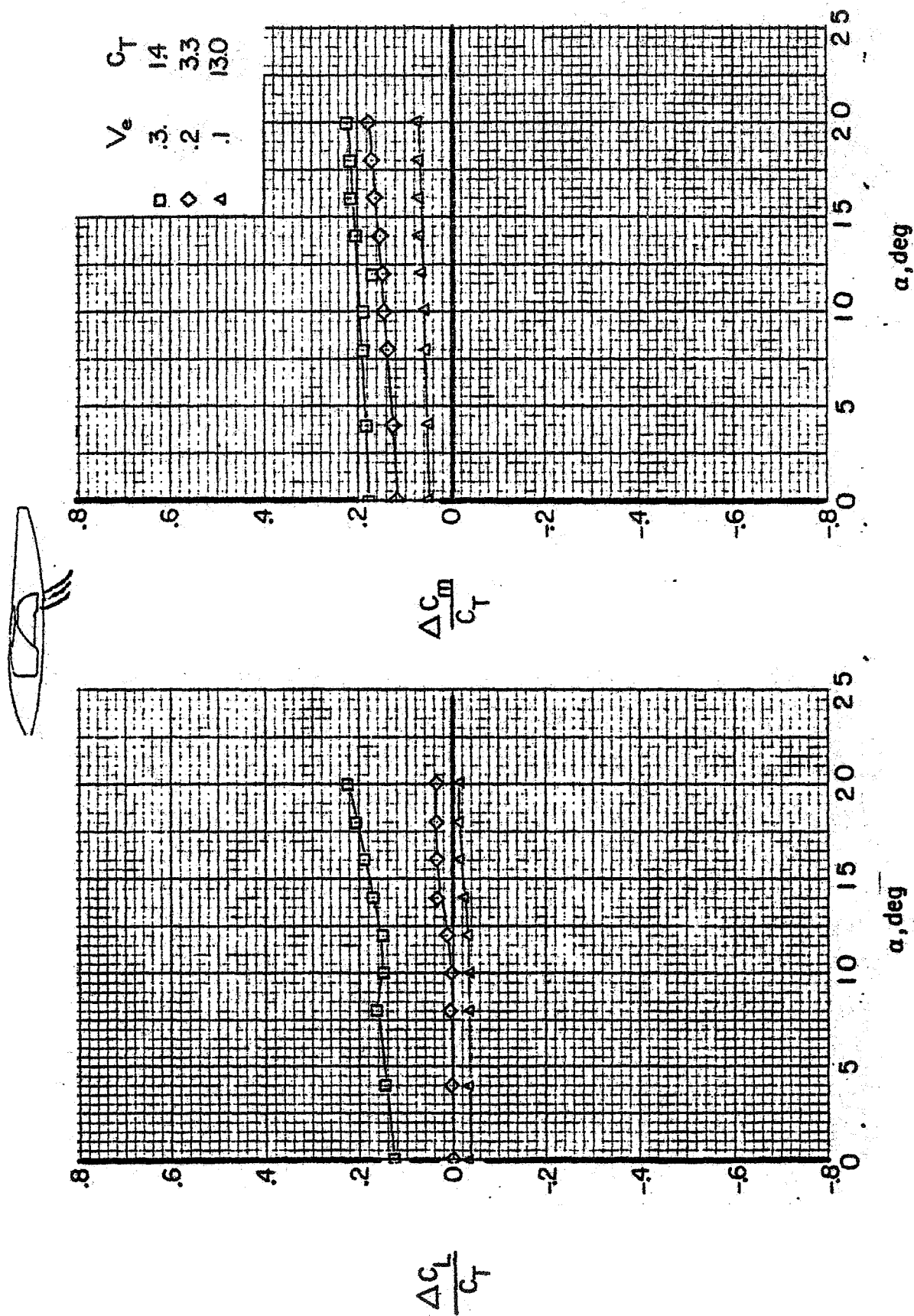


Figure 22. - Variation of the interference effects with angle of attack for the rear vectored thrust configuration.

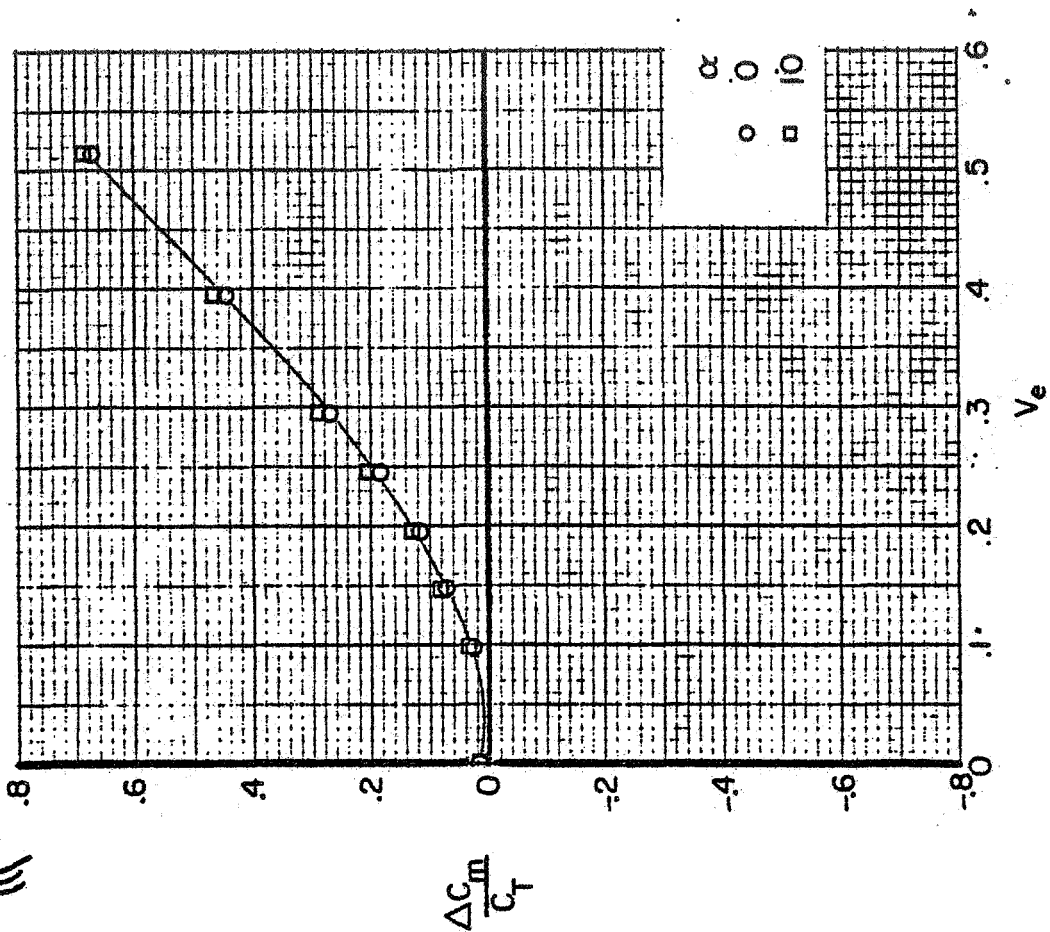
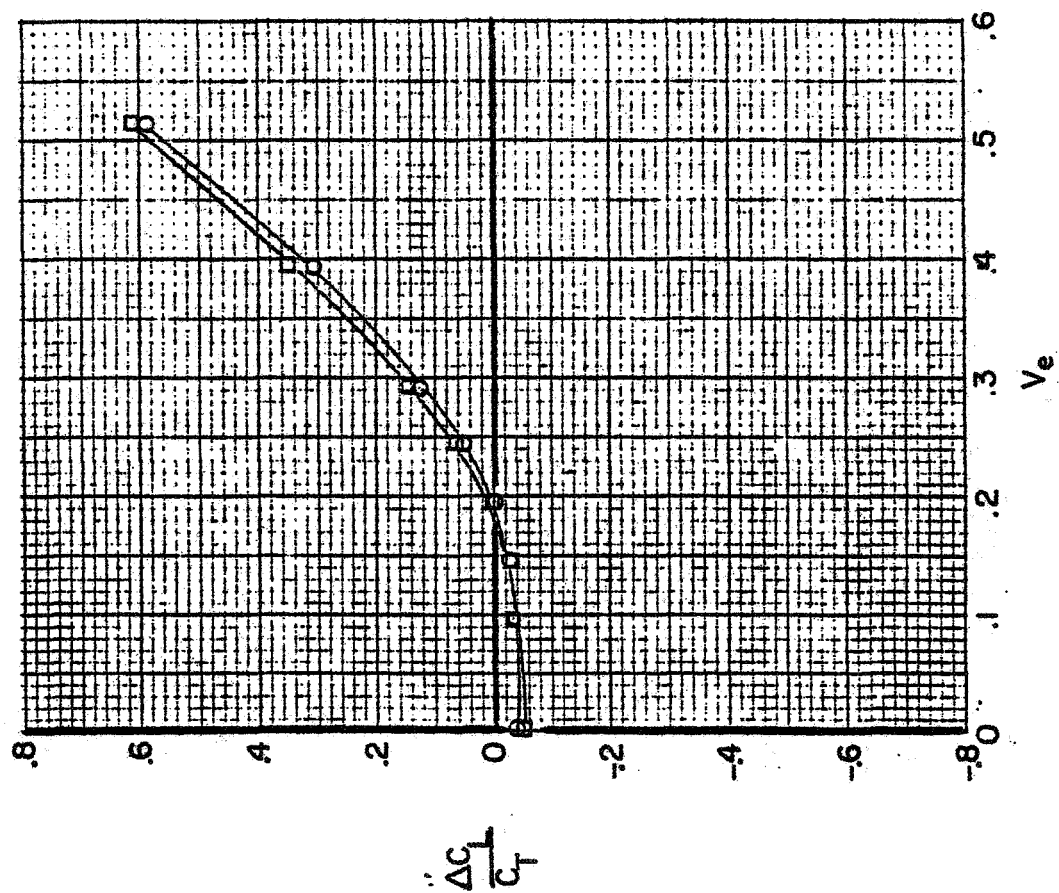


Figure 23. - Variation of the Interference effects with effective velocity ratio for the rear vectored thrust configuration.

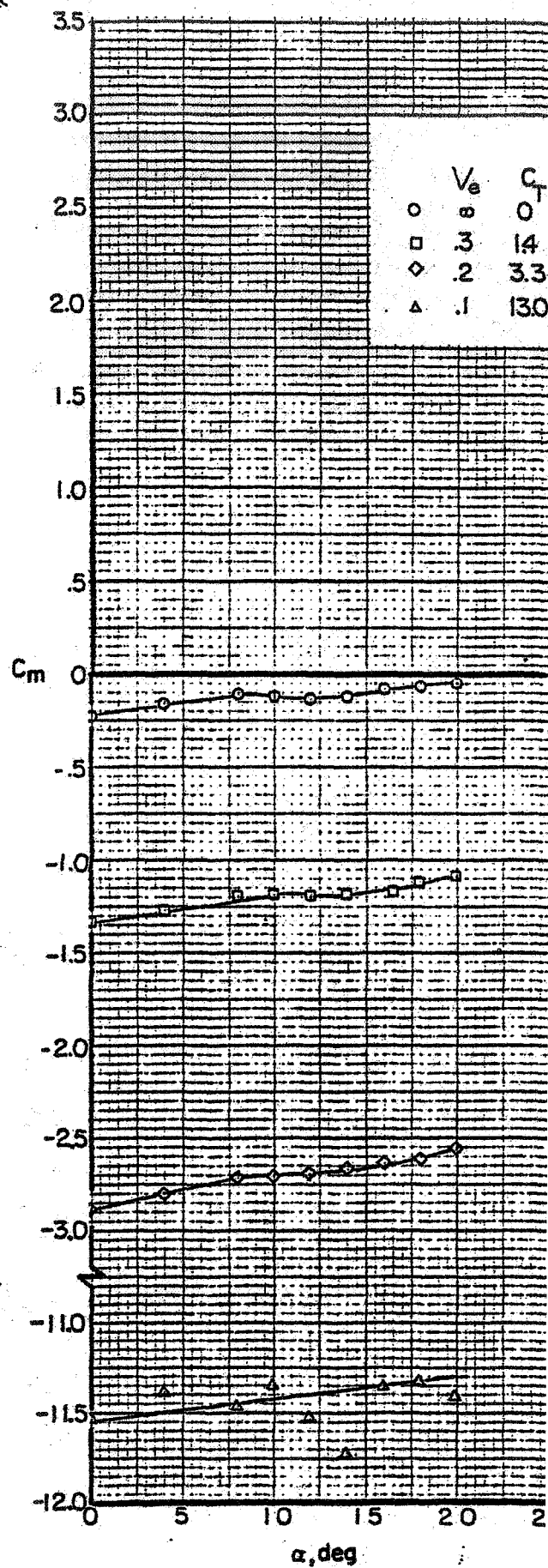
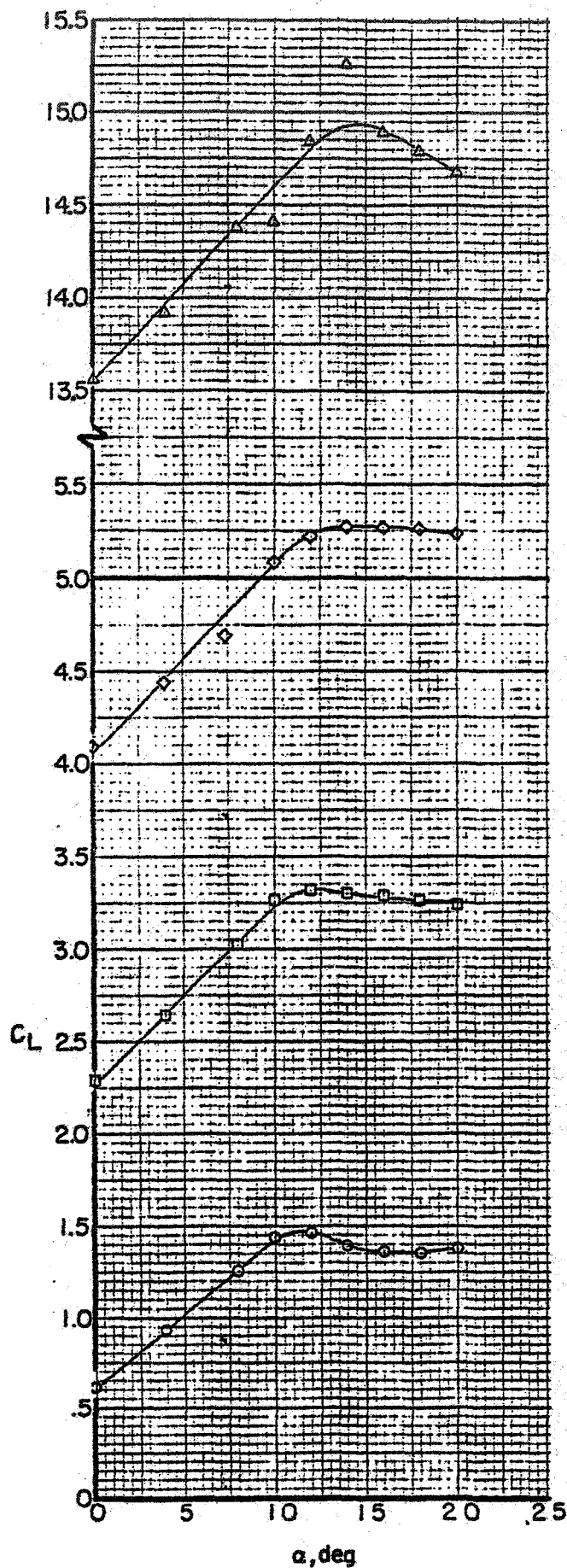


Figure 24 - Basic aerodynamic characteristics of the rear vectored thrust configuration with flaps.

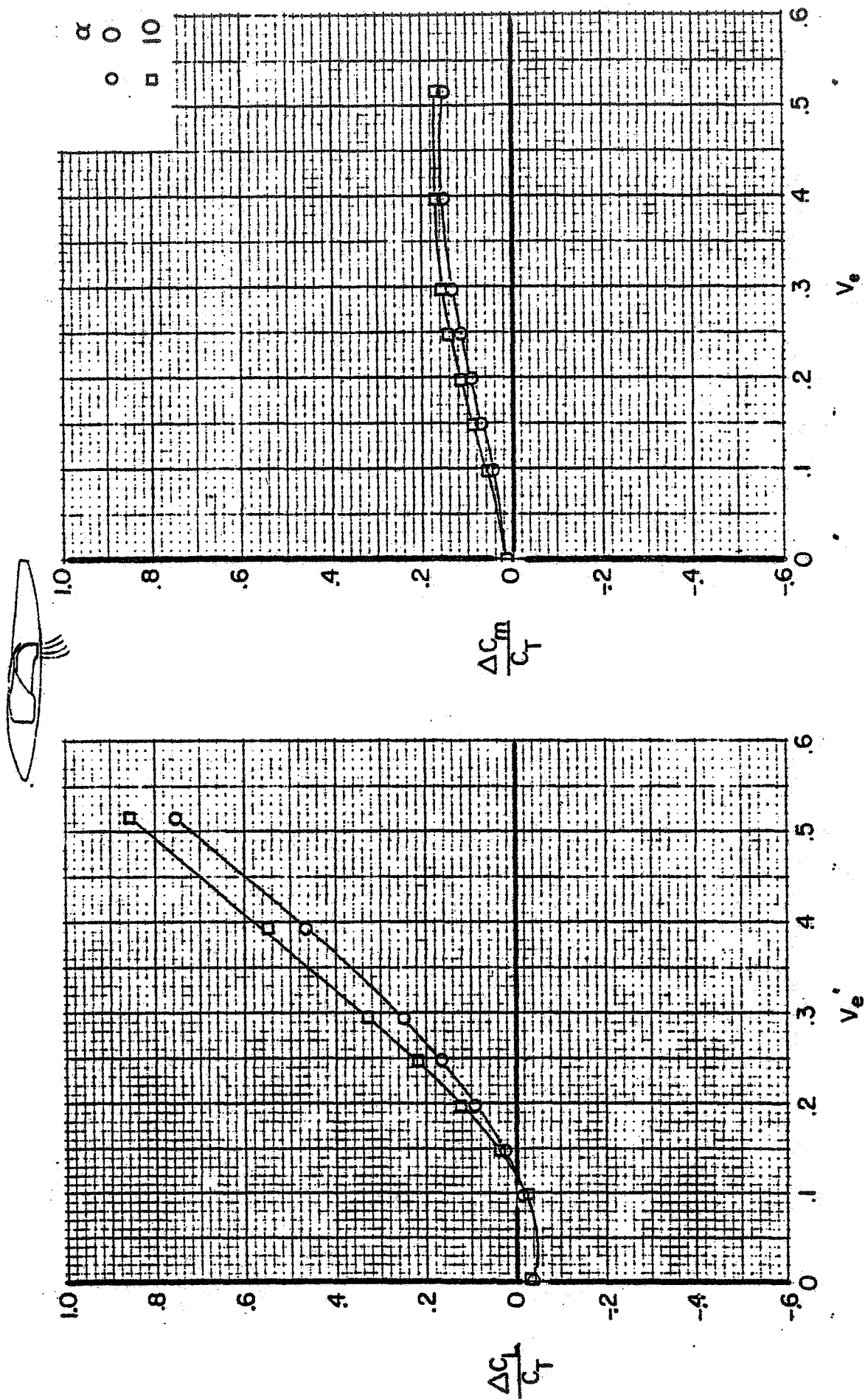
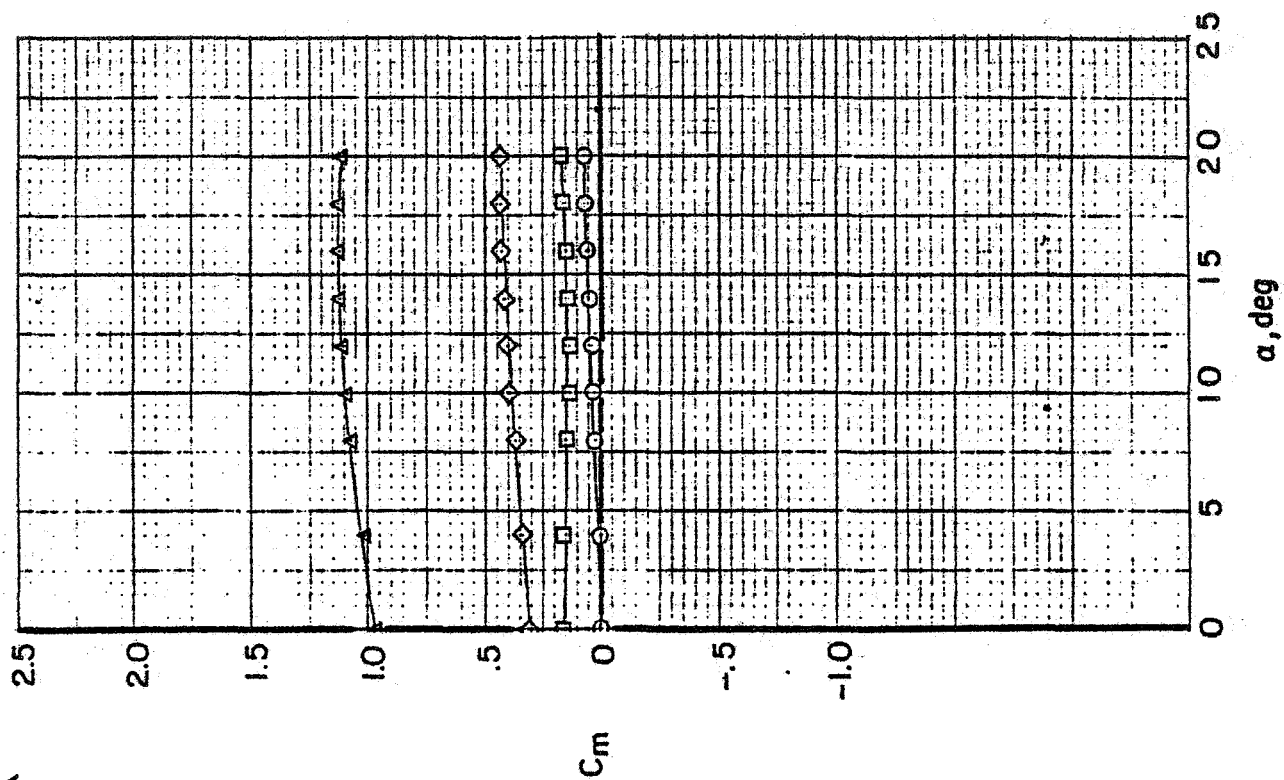
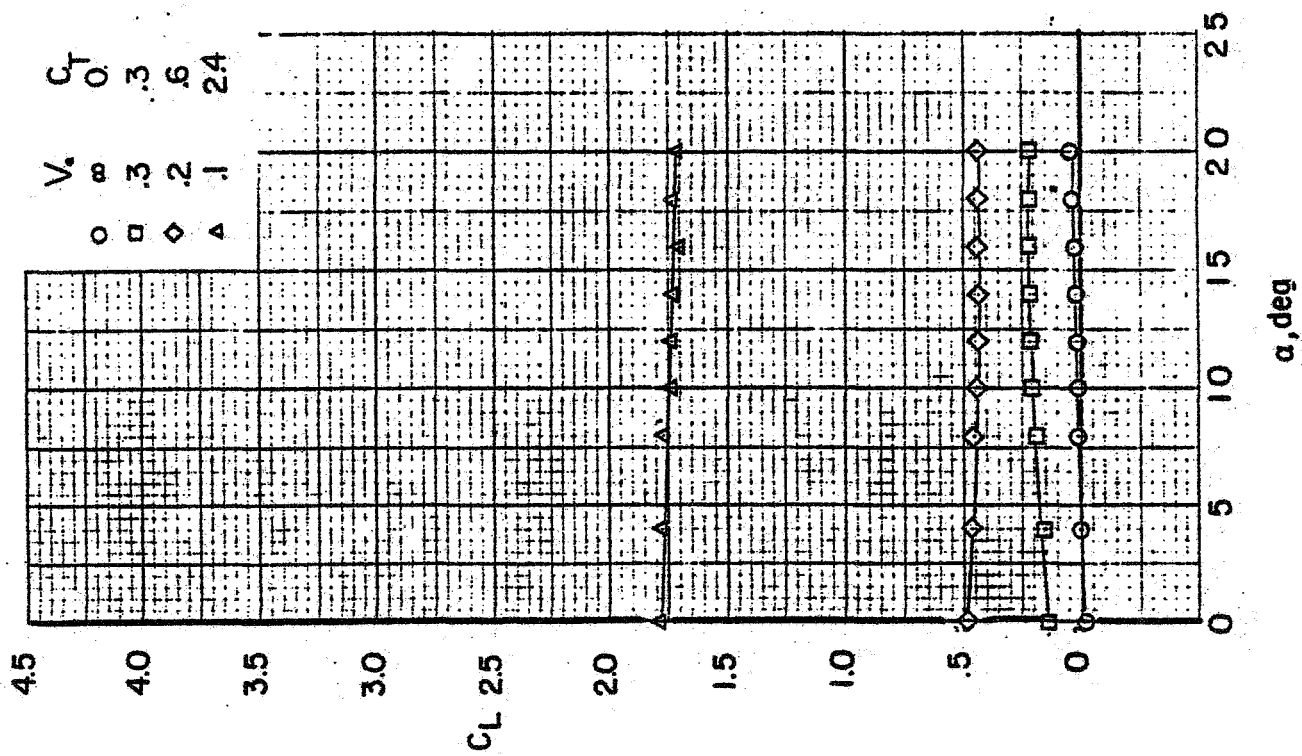


Figure 25. - Variation of the jet induced interference with effective velocity ratio for the rear vectored thrust jets with flaps.



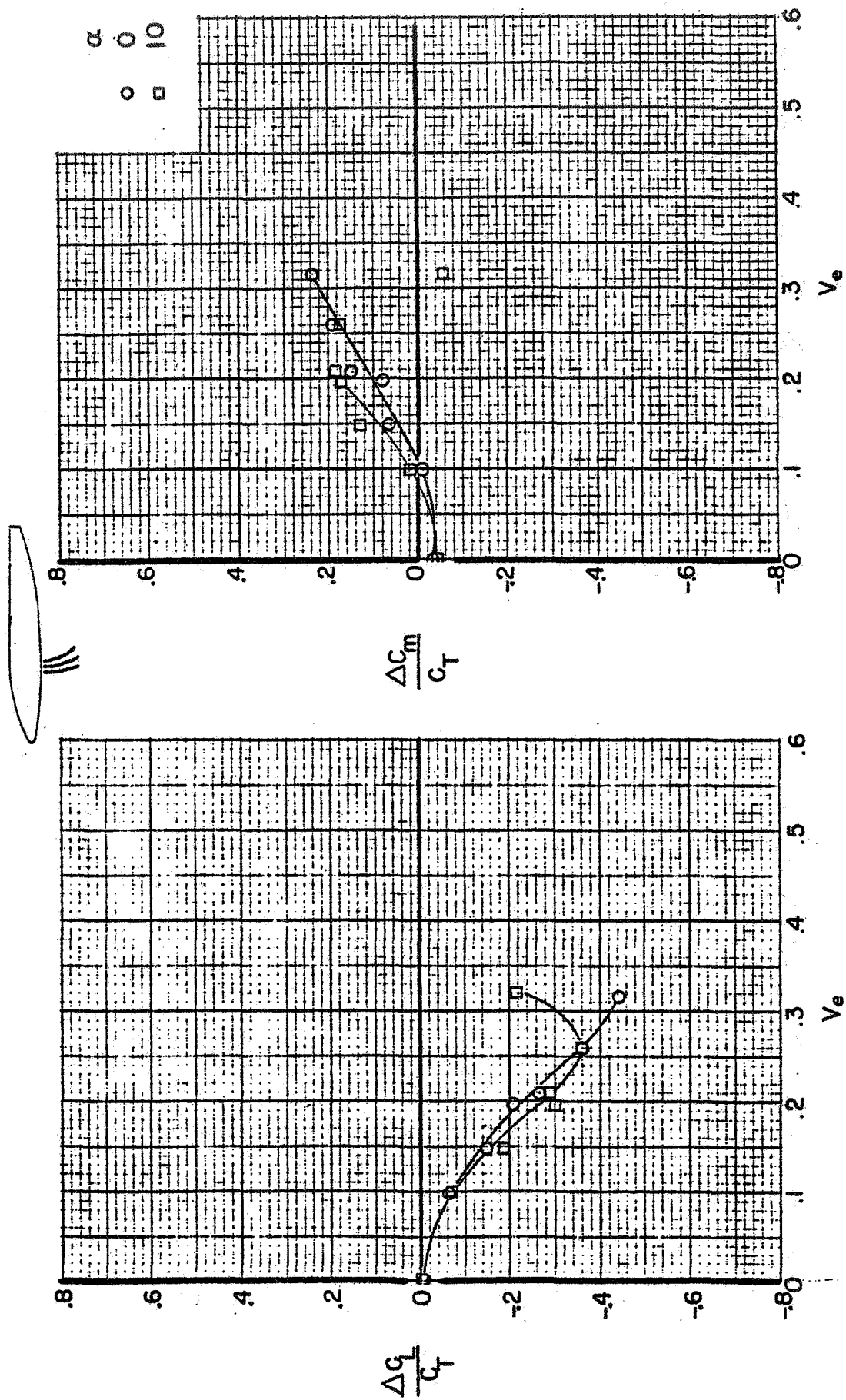
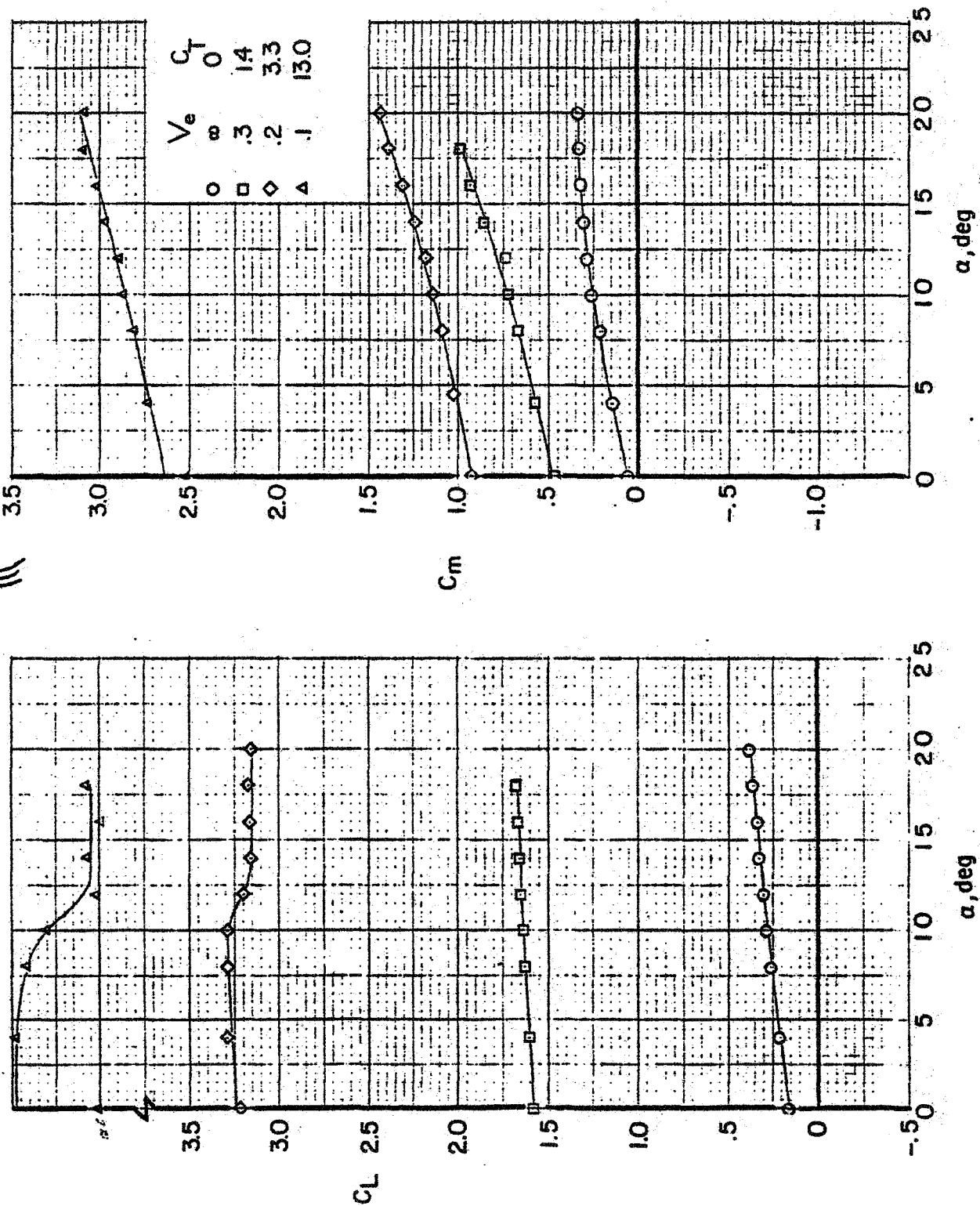


Figure 27. - Variation of the jet induced interference effects with effective velocity ratio for the fuselage alone with the lift jet.



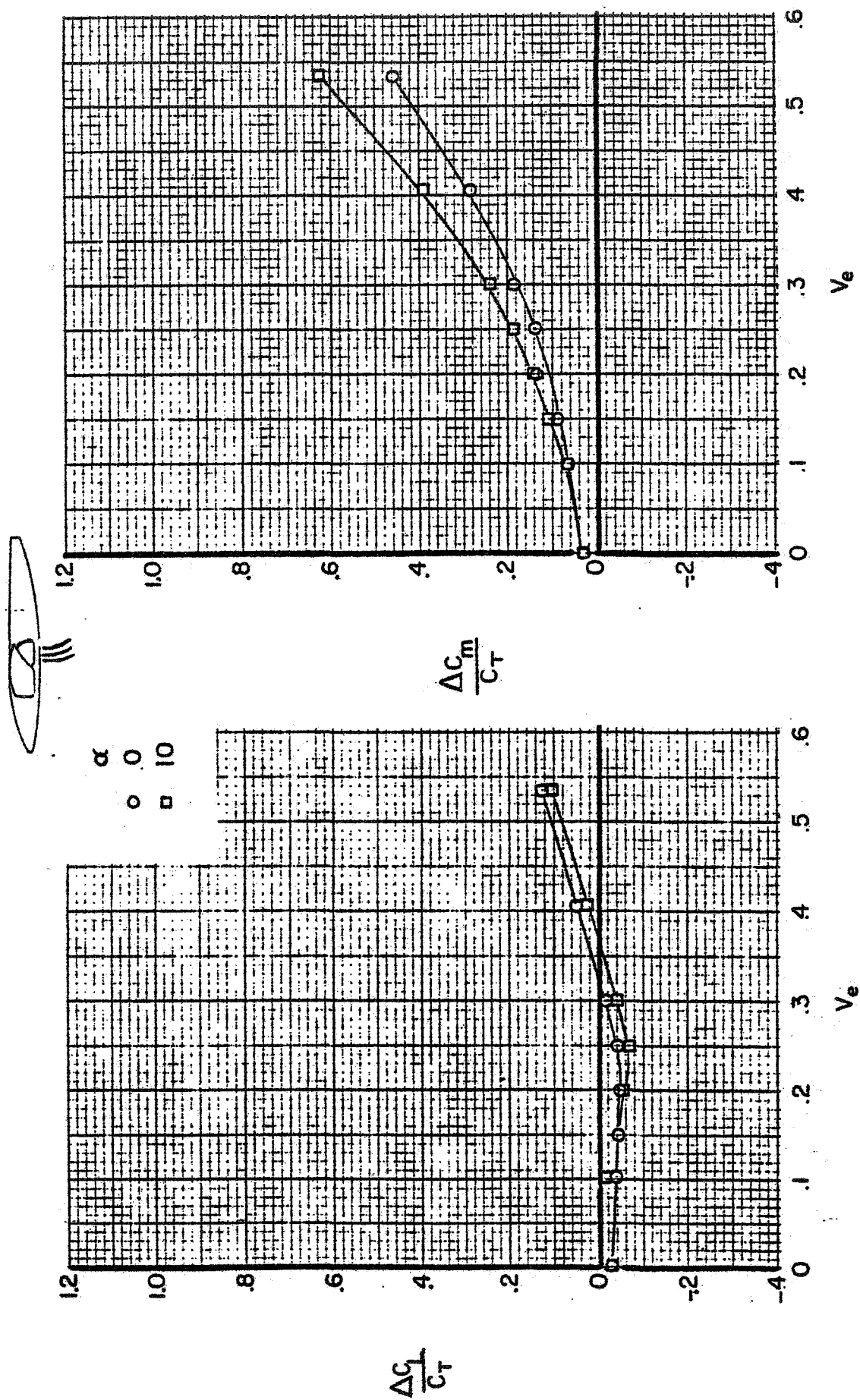


Figure 29. - Variation of the jet induced interference effects with effective velocity ratio for the fuselage alone with the front vectored thrust jets.

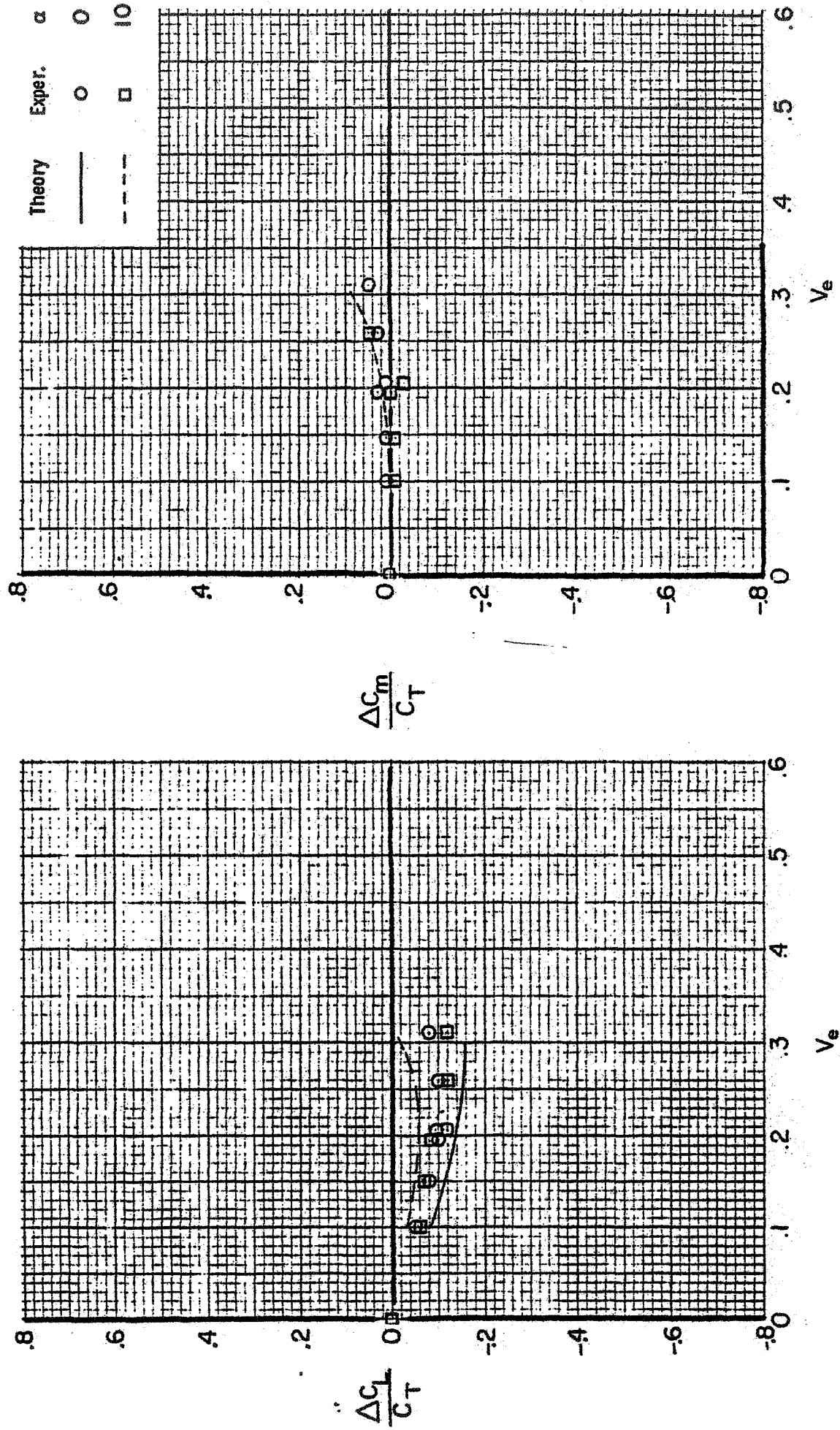


Figure 30. - Variation of the Interference effects on the wing with effective velocity ratio for the lift jet.

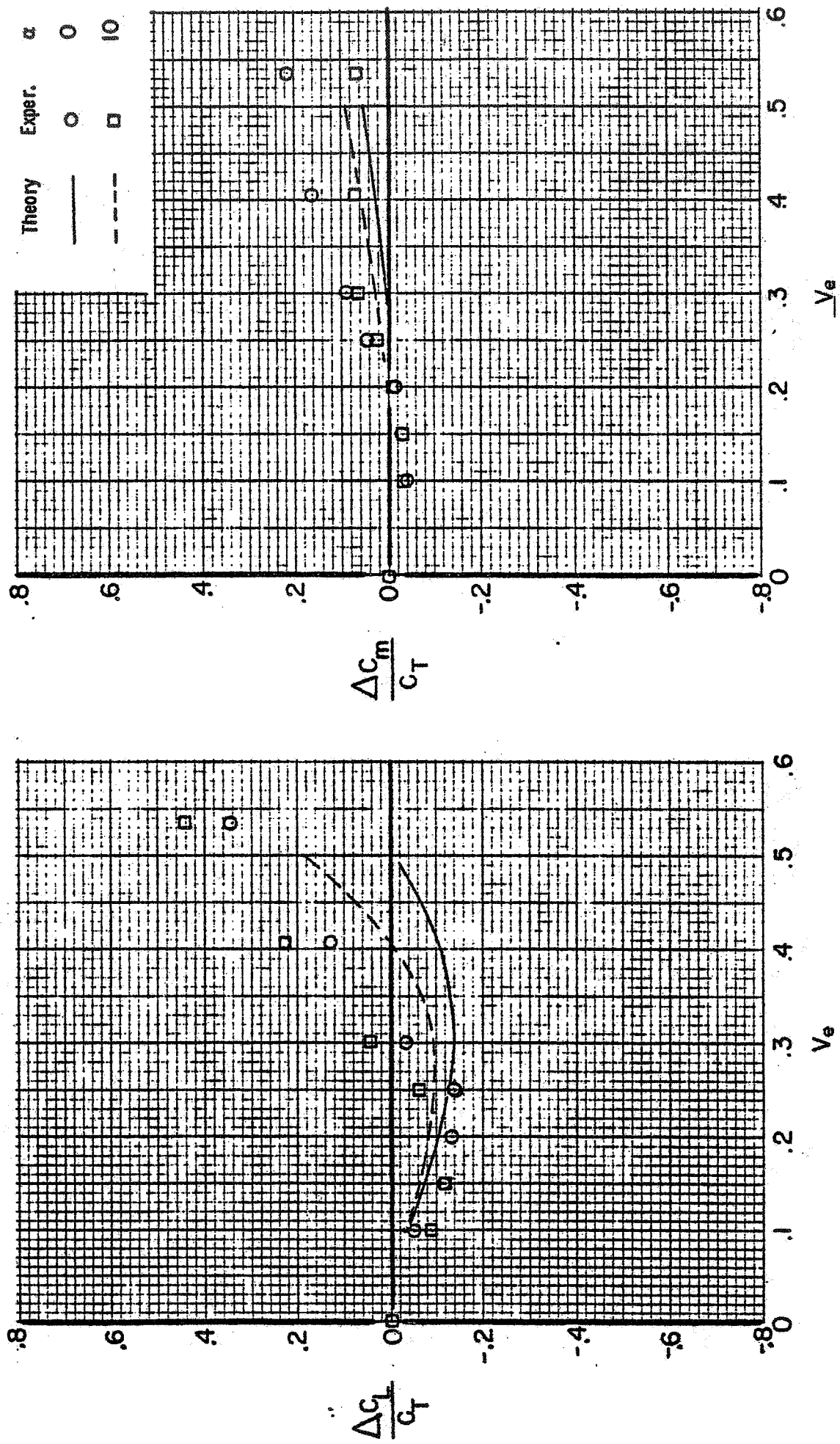


Figure 31. - Variation of the Interference effects on the wing with effective velocity ratio for the front vectored thrust jets.

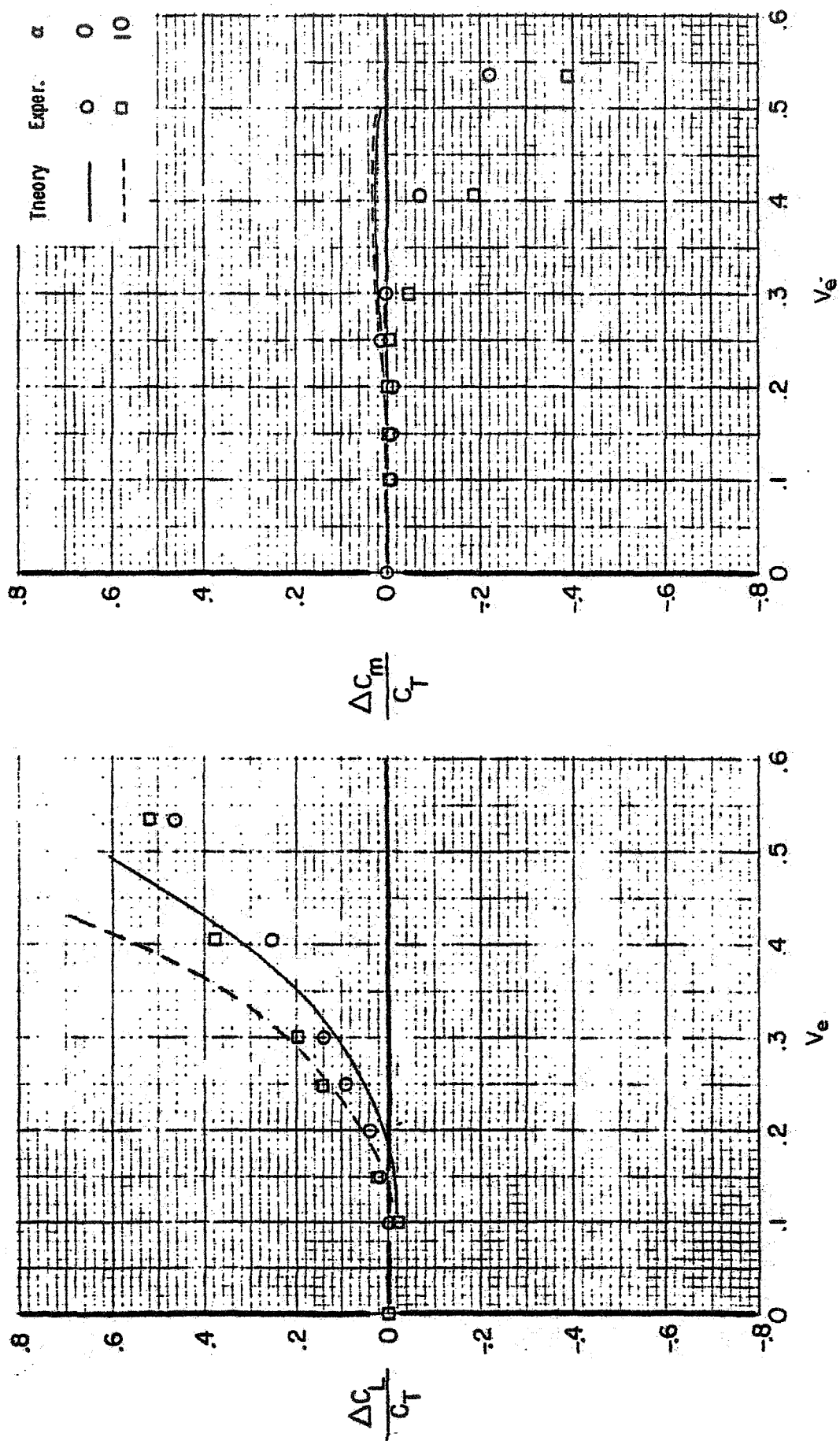


Figure 32. - Variation of the Interference effects on the wing with effective velocity ratio for the rear vectored thrust jets.

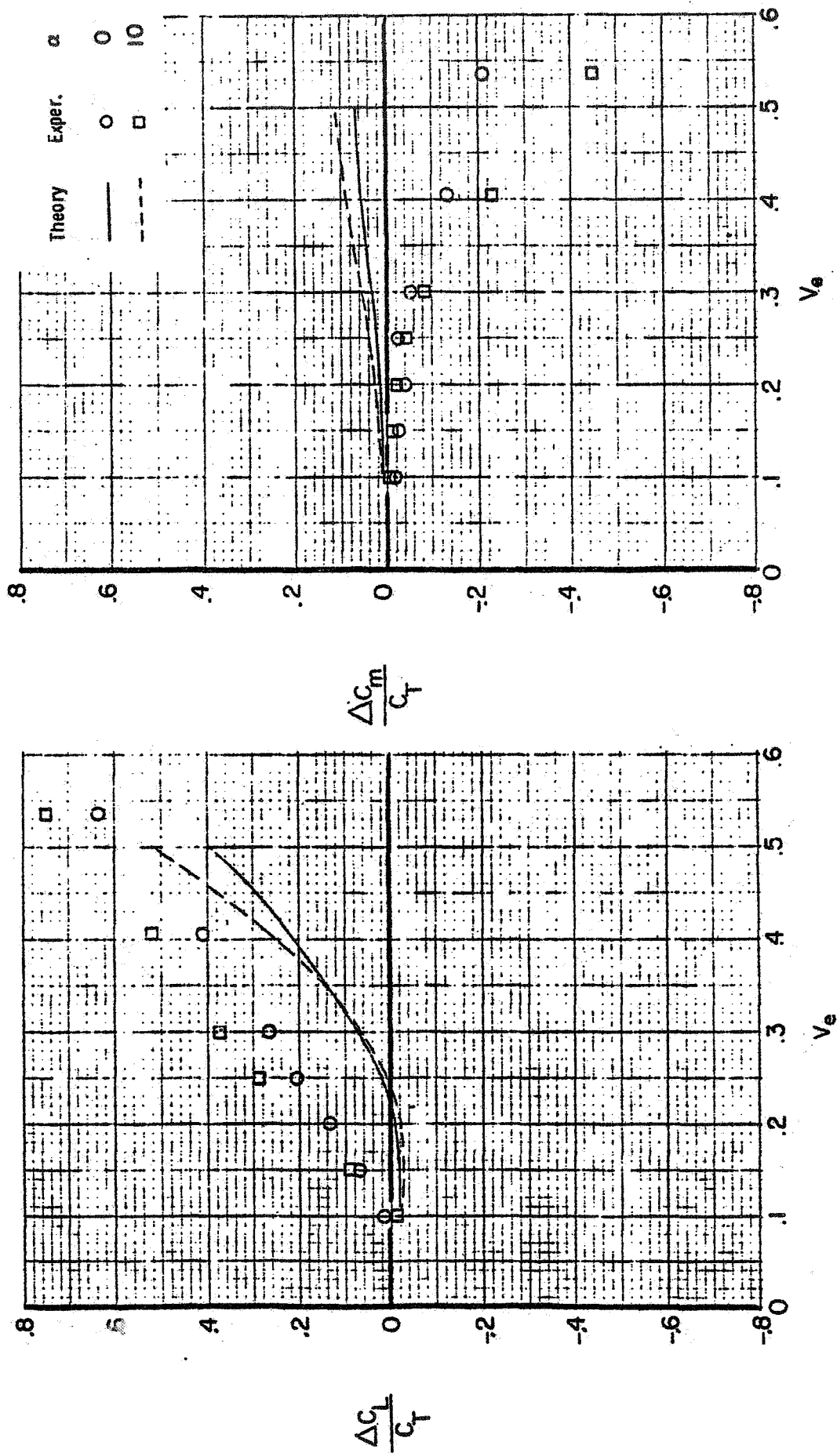


Figure 33. - Variation of the Interference effects on the wing with flaps with effective velocity ratio for the rear vectored thrust jets.